Abstract

In three research articles we have studied the critical properties of effective lattice models for strongly correlated electron systems by Monte Carlo simulations. A similar model is used in a fourth article for investigating thermal fluctuations of vortices in a rotating Bose–Einstein condensate. In the first part of this thesis we review the necessary background and introduce the models one by one. The last part is a collection of the papers.

Paper I [1]: We consider the scaling of the mean square dipole moment in a plasma with logarithmic interactions in a two- and three-dimensional system. In both cases, we establish the existence of a low-temperature regime where the mean square dipole moment does not scale with system size and a high-temperature regime does scale with system size. Thus, there is a nonanalytic change in the polarizability of the system as a function of temperature, and hence a metal-insulator transition in both cases. The relevance of this transition in three dimensions to quantum phase transitions in $2 + 1$-dimensional systems is briefly discussed.

Paper II [2]: The existence of a discontinuity in the inverse dielectric constant of the two-dimensional Coulomb gas is demonstrated on purely numerical grounds. This is done by expanding the free energy in an applied twist and performing a finite-size scaling analysis of the coefficients of higher-order terms. The phase transition, driven by unbinding of dipoles, corresponds to the Kosterlitz-Thouless transition in the 2D XY model. The method developed is also used for investigating the possibility of a Kosterlitz-Thouless phase transition in a three-dimensional system of point charges interacting with a logarithmic pair-potential, a system related to effective theories of low-dimensional strongly correlated systems. We also contrast the finite-size scaling of the fluctuations of the dipole moments of the two-dimensional Coulomb gas and the three-dimensional logarithmic system to those of the three-dimensional Coulomb gas.

Paper III [3]: We perform large-scale Monte Carlo simulations on an effective gauge theory for an easy plane quantum anti-ferromagnet, including a Berry phase term that projects out the $S = 1/2$ sector. Without a Berry phase term, the model exhibits a phase transition in the 3DXY universality class associated with proliferation of gauge-charge neutral U(1) vortices. The instantons that

eliminate the phase transition in the gauge-charged sector are cancelled by the Berry phases. The result is a first order phase transition. This gauge theory therefore does not exhibit deconfined criticality.

Paper IV [4]: We perform Monte Carlo studies of vortices in three dimensions in a cylindrical confinement, with uniform and nonuniform density. The former is relevant to rotating ^{4}He, the latter is relevant to a rotating trapped Bose condensate. In the former case we find dominant angular thermal vortex fluctuations close to the cylinder wall. For the latter case, a novel effect is that at low temperatures the vortex solid close to the center of the trap crosses directly over to a tension-less vortex tangle near the edge of the trap. At higher temperatures an intermediate tensionful vortex liquid located between the vortex solid and the vortex tangle, may exist.

Acknowledgements

Asle Sudbø has been the supervisor for my graduate studies over the last four years. I am very grateful for that and for him giving me the opportunity to start this work in the first place. He was also teaching a couple of courses in my undergraduate studies, providing the right inspiration for me to enter the field of statistical mechanics.

About the time I was beginning my graduate studies Joakim Hove was in the process of ending his. He gave me thorough and essential help both on software issues and on physics in general, and during the last year I have enjoyed working with him again as he returned to a postdoctoral stay in Trondheim. Joakim is also acknowledged for proofreading this thesis.

Former graduate students Jo Smiseth and Eivind Smørgrav who both finished last year have been valuable discussion partners. Their numerous papers are important references and fundaments for my study, as is the portfolio of Egor Babaev. Egor initiated the work of paper IV [4] and I highly appreciate his insight and crucial contributions to this. I thank Flavio S. Nogueira for coauthoring paper I and III [1, 3].

Fellow graduate students and postdocs continue to make our department a nice place to work. Kjetil Børkje is a coauthor of paper II [2] and he has helped me proofreading the chapter concerning that study. Eskil K. Dahl, Martin S. Grønsleth, Daniel Huertas-Hernando, Jacob Linder, Jan Petter Morten, Anh Kiet Nguyen, Lars Erik Walle: Thank you all for providing such a stimulating environment for discussions, work and pleasant coffee breaks.

Finally, I want to mention my friends and former class mates: Håvard Berland, Hugo Hammer, Kjetil Midthun and Geir Solgaard. Since you chose to stay in Trondheim after graduation, it was easy for me too to decide to continue here these four additional years.

The Norwegian University of Science and Technology has kindly provided the financial support for this work.

Steinar Kragset

Trondheim, September 2006

List of papers

Paper I: S. Kragset, A. Sudbø, and F. S. Nogueira,
Metal-insulator transition in two- and three-dimensional logarithmic plasmas,
Physical Review Letters **92**, 186403 (2004).

Paper II: K. Børkje, S. Kragset, and A. Sudbø,
Instanton correlators and phase transitions in two- and three-dimensional logarithmic plasmas,
Physical Review B **71**, 085112 (2005).

Paper III: S. Kragset, E. Smørgrav, J. Hove, F. S. Nogueira and A. Sudbø,
First order phase transition in a gauge theory of $S = 1/2$ quantum antiferromagnets,
cond-mat/0609336, (submitted to Physical Review Letters).

Paper IV: S. Kragset, E. Babaev, and A. Sudbø,
Thermal fluctuations of vortex Matter in trapped Bose condensates,
cond-mat/0604416, (accepted for publication in Physical Review Letters).

Contents

Preface

Strong local repulsion among electrons in many-particle systems is believed to be responsible for strange physical properties like the breakdown of Landau Fermi liquid theory in certain cuprate compounds. Since the discovery of high temperature superconductivity in such materials by Bednorz and Müller in 1986, the focus has increased on strongly correlated electron systems. In order to understand the physics of these compounds, great theoretical effort has been laid down in the study of lightly doped Mott–Hubbard insulators in two spatial dimensions (2D) at zero temperature. Effective lattice field theories in $2+1$ space-time dimensions can be formulated and used in classical Monte Carlo simulations to search for characteristics of transitions between various ground states in the 2D quantum mechanical model. Such phase transitions are driven by parameters like pressure or doping.

In this thesis we present Monte Carlo results for three distinct models in $2+1$ space-time dimensions. In Chapter 3 and 4 we introduce the investigations of two models for various zero temperature properties of a strongly correlated electron system in two spatial dimensions. The first is a lattice gas of charge-like particles which interact through a logarithmic potential, and predicted to exhibit a phase transition of the so-called Berezinskii–Kosterlitz–Thouless type. Due to the many similarities with the classical two dimensional Coulomb gas, we perform simulations on both two and three dimensional systems. Here, a novel characterization technique is developed and tested. In the second model, we find evidence for a phase transition of first order.

The nonuniform 3DXY model that we introduce in Chapter 5 can be applied to a trapped, three dimensional Bose–Einstein condensate. In rotating such systems, remarkably large and beautiful arrays of vortices have been experimentally attainable since the last few years. We investigate their thermal fluctuations.

Chapter 1 and 2 is devoted to review the necessary background to appreciate the work we introduce in the last three chapters, and present in the four research articles [1, 2, 3, 4]. This is done by an evolution from the simple Ising model to the phenomenological Ginzburg–Landau theory for superconductivity, which can be thought of as a generic theory for the models in the included collection of papers at the end of the thesis.

The work of this thesis is a natural continuation of the previous studies in our research group, References [5, 6, 7, 8, 9], which all have benefited from the high performance supercomputing facilites at NTNU. As effective lattice theories in condensed matter physics require large amounts of computation time, access to a powerful supercomputer has been essential.

Chapter 1

Statistical mechanics

Resolution is an important concept in today's digital cameras. It is now common knowledge how digital pictures are put together by millions of tiny pixels, and in a given picture we want sufficiently many so that we cannot tell them apart. Zooming in will however eventually reveal the microscopic structure of pixels. A similar effect is appearant in a newspaper picture. Even though the only colors used in the printing process are black and white, the picture contains almost every shades of gray. If you look carefully, you can see tiny dots of black onto the white paper, and the density or size of these dots decide the amount of gray. Reading the news, you don't notice the dots, your eyes average over them and the white space in between, and you only see the smooth grayscale picture.

In statistical mechanics we attempt to average over microscopic details in a system with macroscopically many particles in order to obtain thermodynamic quantities such as magnetization, total energy, and heat capacity, as well as derive the relations between them. The exact origin of these quantities disappears in the averaging process, as details in a picture are smoothened out when viewed from a distance.

There are however examples where some microscopic details are not averaged out. In a system with a *critical* behaviour, the range of correlations can grow when certain values of control parameters are approached. The range can in fact diverge to infinity, and since infinity is the same on any length scale they will in principle look the same irrespective of our zoom level. Of course, a physical system has a finite size and structures within it have to be restricted to fit into those dimensions. Still, we can often consider these systems infinitely large because they are so many orders of magnitude larger than the phenomena and the scales we think of when zooming in and out. On the other hand, in computer simulations, size does indeed play an important role, and this will be discussed in the context of finite size scaling in Chapter 2.

In the following sections, we will first establish some basic relations of statistical mechanics before we proceed to the concepts of phase transitions and critical phenomena. Along the way we will encounter a few simple but important models capturing many of the features essential for the main works in this thesis.

1.1 Statistical mechanics and thermodynamics

The goal of statistical mechanics is basically to compute the partition function Z for a given system [10, 11, 12]. This is a weighted sum over all configurations ψ the system can be in. All the information needed to calculate the thermodynamic properties are contained in Z. The partition function can be written

$$Z = \sum_{\{\psi\}} \mathrm{e}^{-\beta H_\psi}, \tag{1.1}$$

where H is the system's Hamiltonian and $\beta \equiv 1/(k_B T)$, with T the temperature and k_B the Boltzmann's constant. Knowing this sum we can derive the expectation values of essentially all thermodynamic observables O,

$$\langle O \rangle = \frac{1}{Z} \sum_{\{\psi\}} O_\psi \mathrm{e}^{-\beta H_\psi}, \tag{1.2}$$

by differentiations of Z with respect to various parameters in the exponent. If the system is in thermal contact with a heat reservoir which keeps the temperature fixed, the internal energy U can be calculated from the canonical partition function by

$$U \equiv \langle H \rangle = \frac{1}{Z} \sum_{\{\psi\}} H_\psi \mathrm{e}^{-\beta H_\psi} = -\frac{\partial}{\partial \beta} \ln Z. \tag{1.3}$$

Additionally, if we hold volume V and particle number N constant, the following fundamental thermodynamic relations involving the Helmholtz free energy $F = U - TS$,

$$dF = dU - TdS - SdT \underset{V,\, N \text{ constant}}{=} -SdT, \tag{1.4}$$

and

$$U = F + TS = F - T\left(\frac{\partial F}{\partial T}\right) = -T^2 \left[\frac{\partial}{\partial T}\left(\frac{F}{T}\right)\right] = \left[\frac{\partial (F/T)}{\partial (1/T)}\right], \tag{1.5}$$

can be used to express F in terms of Z. By comparison with Equation (1.3) we find

$$F = -\frac{1}{\beta} \ln Z, \tag{1.6}$$

which acts as the connection between statistical mechanics and thermodynamics.

But the partition function can also give insight into fluctuations, something classical thermodynamics can not. Energy fluctuations around a system's equilibrium value,

$$(\delta U)^2 \equiv \langle (H - \langle H \rangle)^2 \rangle = \langle H^2 \rangle - \langle H \rangle^2, \tag{1.7}$$

can be calculated from Z by subsequent differentiations as in Equation (1.3),

$$(\delta U)^2 = \frac{1}{Z}\left(\frac{\partial^2 Z}{\partial \beta^2}\right) - \left(\frac{1}{Z}\left(\frac{\partial Z}{\partial \beta}\right)\right)^2 = \left(\frac{\partial^2 \ln Z}{\partial \beta^2}\right). \tag{1.8}$$

From the definition of the heat capacity $C_V \equiv (\partial U/\partial T)$, we see that the fluctuations in the energy of a system can be measured through

$$C_V = \frac{1}{k_B T^2}(\delta U)^2 \equiv \langle (H - \langle H \rangle)^2 \rangle = k_B \beta^2 \left(\frac{\partial^2 \ln Z}{\partial \beta^2}\right), \tag{1.9}$$

and from now on we set k_B equal to unity for simplicity.

Generalizing slightly to having more than one temperature-like parameter, or equivalently coupling γ, in the partition function, we let $\beta H \to S = \sum_\gamma \gamma H_\gamma$. The *moments* of the energy can then be found by differentiation of the correspondingly generalized free energy F,

$$\frac{\partial F}{\partial \mu} = -\langle H_\mu \rangle, \tag{1.10}$$

$$\frac{\partial^2 F}{\partial \mu \partial \lambda} = \langle (H_\mu - \langle H_\mu \rangle)(H_\lambda - \langle H_\lambda \rangle) \rangle, \tag{1.11}$$

$$\frac{\partial^3 F}{\partial \mu \partial \lambda \partial \eta} = -\langle (H_\mu - \langle H_\mu \rangle)(H_\lambda - \langle H_\lambda \rangle)(H_\eta - \langle H_\eta \rangle) \rangle. \tag{1.12}$$

The second moment Equation (1.11) with $\mu = \lambda = \beta$ corresponds to the heat capacity. Of these moments, the third moment Equation (1.12) will in particular prove to be a valuable tool for extracting critical exponents from Monte Carlo simulations [13, 14].

1.2 Phase transitions

To most people, the familiar examples of phase transitions are the boiling of water and melting of ice, but the magnetic to non-magnetic transition is a standard introductory example because of its simplicity [15]. We will concentrate on this transition which is *continuous* and can take place in uniaxial ferromagnets for which a typical situation is shown in Figure 1.1 (a). The magnetization M goes continuously to zero at a *critical temperature* T_C when the temperature is increased.

If exposed to an external magnetic field h, these systems can also demonstrate the other common type of phase transitions, namely a *first order* transition as h changes sign. In Figure 1.1 (b) the solid line at $T < T_C$ indicates a first order transition where M jumps discountinuously from a negative to a positive value

as h is increased. Also melting transitions are typically first order. Later, we will encounter yet another type, the *Berezinskii–Kosterlitz–Thouless* transition [16, 17].

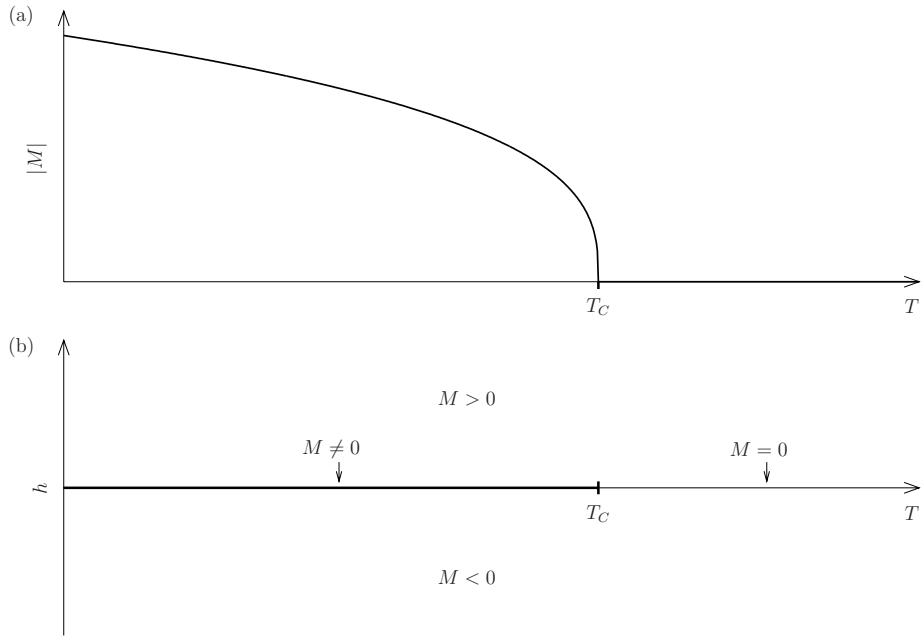

Figure 1.1: The magnetization $M(T)$ goes continuously to zero at T_C (a). If an external magnetic field h is applied, the sign of M is determined by h and jumps discontinuously between a positive and a negative value across the solid line (b).

1.2.1 The Ising model

A uniaxial ferromagnet can be modelled on a lattice in d dimensions by the Ising model [18] given by the hamiltonian

$$H = -J \sum_{\langle ij \rangle} s_i s_j - h \sum_i s_i, \tag{1.13}$$

where J is a coupling constant determining the interaction between nearest neighbour spins s_i and s_j, and h is an external magnetic field. Each spin can point either up ($s_i = 1$) or down ($s_i = -1$). The lattice will in this work always be

square meaning that each spin site i has $2d$ nearest neighbour sites. In statistical mechanics we take the temperature $T = 1/\beta$ into account through the partition function Z Equation (1.1), and for simplicity we set the coupling J to unity, since its only effect is to define the units of β. If the system has the same linear extension L in units of the lattice spacing in all d directions, the number of terms in Z is 2^{L^d}. Hence, the partition function is difficult and often impossible to evaluate analytically. We will get back to a way to work around this problem in Chapter 2.

In $d = 1$ dimensions and $h = 0$ the Ising model does not exhibit any phase transition for $T > 0$, but in higher dimensions it does: Consider the model in $d > 1$ with infinitely many spins $N \equiv L^d \to \infty$. At high temperatures and $h = 0$ there is no net magnetization,

$$M = \frac{1}{N} \sum_i s_i = 0, \tag{1.14}$$

because the spins are not likely to point in any particular direction. Thermal fluctuations ensure complete *disorder* among the spins. However, as the temperature is lowered the system spontaneously starts to organize a continuously growing majority of its spins either up or down when the critical temperature T_C is passed as shown in Figure 1.1 (a). Consequently, the system is said to have a *disordered* and an *ordered* phase. The two phases can be predicted from arguments regarding the free energy $F = U - TS$. At high temperatures $T \to \infty$, maximization of the entropy S will always dominate over internal energy $U = \langle H \rangle$ in the system's quest for minimum free energy. The highest entropy is obtained by disordering the system and thus $M(T \to \infty) = 0$. At $T = 0$ on the other hand, when there are no thermal fluctuations, minimizing the Hamiltonian Equation (1.13) by ordering the system so that all spins point in the same direction will minimize F. In $d > 1$ dimensions this ordering takes place at a nonzero temperature.

In the Ising model, M is the *order parameter* describing which of the two possible phases the system is in: The disordered with $M = 0$ or the ordered with finite magnetization. Continuous phase transitions are characterized close to T_C by a power law dependence of the order parameter on the reduced temperature $\tau \equiv (T - T_C)/T_C$,

$$M \sim \tau^\beta \tag{1.15}$$

where β is a *critical exponent*. The order parameter is not always known in a given system, but β can still be found from relations to other critical exponents, see section 2.5.

1.2.2 Landau theory

Given that a system indeed undergoes a transition from an ordered to an unordered phase, Landau developed a theory describing the transition qualitatively [19]. He expanded the difference in free energy F between the two phases of the system in powers of the order parameter, keeping only the lowest order terms consistent with the symmetries of the Hamiltonian,

$$\Delta F = \frac{a\tau}{2}M^2 + \frac{u}{4!}M^4 + \dots \tag{1.16}$$

If $h \neq 0$ in Equation (1.13), a linear term $-hM$ has to be included, but since the theory otherwise is written down as a phenomenological effective theory, the rest of the parameters are considered free. We use the convention $a, u > 0$. Systems with additional intrinsic symmetries could include more terms in the expansion Eq. (1.16), such as the cubic M^3. Now, by minimizing ΔF with respect to M the equilibrium values of the order parameter are found. From Figure 1.2 (a) we see that there is only one minimum when τ is positive, corresponding to the high temperature phase with zero magnetization. As the temperature is decreased and τ becomes negative, the $M = 0$ minimum developes into two minima, and the system spontaneously chooses one of them. The up-down symmetry of the system is broken accordingly.

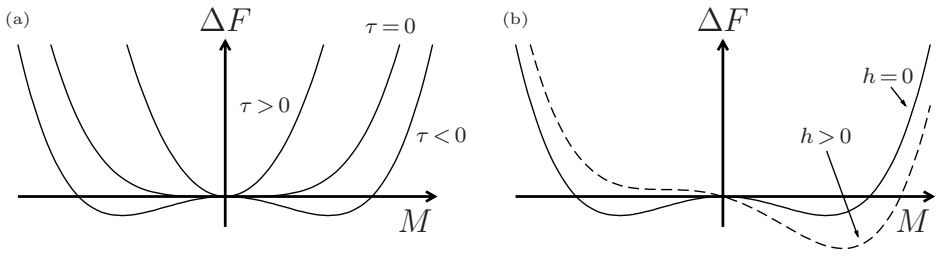

Figure 1.2: Difference in free energy ΔF between to phases according to Landau theory Equation (1.16) in zero (a) and finite (b) external field h. The minima correspond to thermodynamically stable states. In (b) the reduced temperature τ is negative.

In Figure 1.2 (b) τ is negative, and the system can be in either of two equally probable states (solid line), but by turning on a finite $h > 0$ there will only be one true minimum in ΔF (dashed line). In this way the system is forced to be in a state with positive magnetization. If the system originally was in the negatively magnetized state, it will make a discontinuous jump in M corresponding to a first order phase transitition.

The Landau theory does not depend on the microscopic properties of the system. The symmetries of the set of possible ordered phases is reflected in the free energy expansion Equation (1.16), but the symmetries of the true Hamiltonian is in general unknown. Additionally does the theory not depend on the lattice on which we defined the Ising model Equation (1.13). One of the strengths of the theory is that it treats correctly the importance of symmetry in the qualitative aspects of critical phenomena. In the above introduction, we had a uniaxial ferromagnet in mind, but any system with the same set of symmetries could in principles be described by the same theory. This hints to the concept of universality.

1.3 Ginzburg–Landau theory

The Landau theory provides a qualitative description of phase transitions, but its quantitative predictions for T_C or the critical exponents are generally wrong because the theory neglects the effect of fluctuations. A natural generalization would be to allow the magnetization to depend on position,

$$M = \frac{1}{V}\int \mathrm{d}V m(\mathbf{r}). \tag{1.17}$$

Here, we have also allowed the space to be continuous and replaced the number of lattice sites N with the volume V of the system. The simplest extension of Landau theory to incorporate this position dependent order paramater $m(\mathbf{r})$ and fluctuations of it, is called the *Ginzburg–Landau theory* [20],

$$\Delta F = \int \mathrm{d}V \left[\frac{g}{2}(\nabla m)^2 + \frac{a\tau}{2}m^2(\mathbf{r}) + \frac{u}{4!}m^4(\mathbf{r}) + \dots\right]. \tag{1.18}$$

This theory has actually proved successfull, with small variations, as an *effective Hamiltonian* for many different systems. So far, we have only considered a scalar order parameter, but it could as well take a vector or a tensor to characterize the order of the given system. In a superconductor, the order parameter is the superconducting wavefunction

$$\Psi(\mathbf{r}) = |\Psi(\mathbf{r})|\mathrm{e}^{i\theta(\mathbf{r})} = \sqrt{n}\mathrm{e}^{i\theta(\mathbf{r})}, \tag{1.19}$$

where n is the density of Cooper pairs. Since this is a charged and quantum mechanical phenomenon, we include the electromagnetic vector potential $\mathbf{A}$ into the gradient term in the standard way

$$\nabla \to (-i\hbar\nabla - 2e\mathbf{A}), \tag{1.20}$$

and also add a term proportional to $|\nabla \times \mathbf{A}|^2$ in the effective hamiltonian. The full Ginzburg-Landau theory for a superconductor reads

$$H_{SC} = \int \mathrm{d}V \Big[\frac{g}{2} |(\nabla - i\mathbf{A})\Psi(\mathbf{r})|^2 + \frac{a\tau}{2} |\Psi(\mathbf{r})|^2 + \frac{u}{4!} |\Psi(\mathbf{r})|^4 + \frac{\kappa}{2} |\nabla \times \mathbf{A}|^2 \dots \Big]. \tag{1.21}$$

For simplicity, we have here rescaled $\mathbf{A}$ and the free parameters so as to absorb Planck's constant $\hbar$ and the charge $2e$ of the Cooper pairs.

There is actually a close connection between the statistical mechanics of Ginzburg–Landau like theories and quantum field theories in one time and d spatial dimensions at zero temperature. This can be realized by writing down the Feynman path integral of a quantum mechanical problem and interpret it as the partition function of a classical system in $d+1$ Euclidian dimensions [21].

1.3.1 Lattice regularization

The Ginzburg–Landau hamiltonian of Equation (1.21) is a contiumuum theory, but for the following, and especially later for the computer simulations, it is more convenient to reintroduce a lattice. That is, we let the order parameter $\Psi(\mathbf{r}) \to \Psi_i$, so that it is only defined on lattice sites $i = 1, ..., N$ separated by a lattice constant a. Now, we have to replace the gradient term with a gauge invariant lattice difference,

$$|(\nabla - i\mathbf{A})\Psi(\mathbf{r})|^2 \to \sum_{\mu} |\Psi_{i+a\mu} \mathrm{e}^{-iA_{i\mu}} - \Psi_i|^2, \tag{1.22}$$

where $i + a\mu$ is the lattice site situated next to site i in direction μ. The gauge field here lives on the links of the lattice and is given by the line integral

$$A_{i\mu} = \int_i^{i+a\mu} \mathrm{d}l A_\mu. \tag{1.23}$$

The continuum is recovered if we let $a \to 0$. For high T_C superconductors it is a well established approximation only to consider fluctuations in the phase of the order parameter [22]. In this approximation, known as the London model, we assume a condensate of Cooper pairs to exist by having a finite and constant $|\Psi_i| = |\Psi|$, since in the end, it is not the depletion of Cooper pairs that is responsible for destroying superconductivity. Increasing the temperature, large fluctuations in the phase θ makes the condensate incoherent and non-superconducting before $|\Psi|$ vanishes. The right hand side of Equation (1.22) can thus be rewritten

$$|\Psi_{i+a\mu} \mathrm{e}^{-iA_{i\mu}} - \Psi_i|^2 = |\Psi|^2 \left[2 - 2\cos(\Delta_\mu \theta_i - A_{i\mu}) \right], \tag{1.24}$$

where $\Delta_\mu \theta_i = \theta_{i+a\mu} - \theta_i$. To further simplify the model without changing any qualitative properties, we drop constant terms in Equation (1.21) and set the amplitude $|\Psi|$ and lattice constant a to unity. The resulting effective lattice Hamiltonian for superconductivity is

$$H_{\text{London}} = \sum_{i,\mu} \Big[-g \cos(\Delta_\mu \theta_i - A_{i\mu}) + \frac{\kappa}{2} (\varepsilon_{\mu\nu\lambda} \Delta_\nu A_{i\lambda})^2 \Big]. \tag{1.25}$$

We have here rewritten the curl in terms of the totally Levi–Civita tensor $\varepsilon_{\mu\nu\lambda}$. By neglecting the gauge field, Equation (1.25) is nothing but the XY model, a generalization of the Ising model Equation (1.13).

1.3.2 The two dimensional XY model

The Hamiltonian of the XY model,

$$H_{XY} = -\sum_{\langle ij \rangle} \mathbf{s}_i \cdot \mathbf{s}_j \tag{1.26}$$

is similar to the Ising model Equation (1.13), but the spins $\mathbf{s}_i$ are now vectors of unit length, living in a continuous two dimensional spin space. Thus, the Hamiltonian can be written

$$H_{XY} = -\sum_{\langle ij \rangle} \cos(\theta_j - \theta_j) = -\sum_{i,\mu} \cos(\Delta_\mu \theta_i). \tag{1.27}$$

The model can be generalized to have a position dependent bare *phase stiffness*, which would appear as a coefficient P_{ij} in front of the cosine terms (see Chapter 5, but at this point we only consider $P_{ij} = 1$. If the lattice on which the spins are situated is two dimensional ($2D$), the XY model is of special interest from the perspective of phase transitions and critical phenomena because it has a transition which is neither first order nor continuous.

According to Mermin and Wagner [23], there can never be long range order at finite temperatures in two dimensional models with a continuous symmetry. Specifically, for the $2DXY$ model the magnetization $M = 0$ for all nonzero temperatures. At low temperatures there is quasi long range order, but at large distances smooth spin waves eventually destroy the spins' tendency to point in the same direction. The spin–spin correlations decay algebraicly, a feature typical to the situation precicely at the critical temperature of a continuous phase transition. This time however, the feature applies to all temperatures below a certain value, the transition temperature T_{KT}. In the high temperature limit on the other hand, even short range order is absent due to large thermal fluctuations, and the spin–spin correlations decay exponentially with distance.

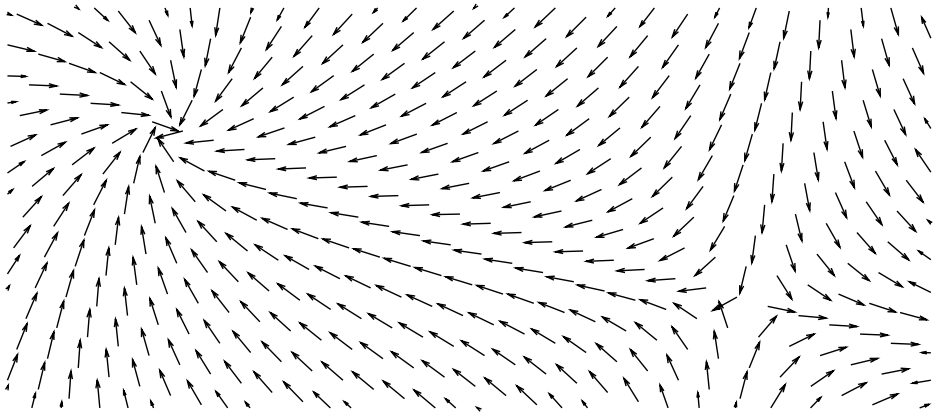

Figure 1.3: A pair of vortices in a two dimensional configuration of spins. The rotation of the phase is opposite around each of the two centers, hence there is no net vorticity. The pair can be viewed as a neutral configuration of charges.

Separating the critical low temperature regime, with algebraic decay of correlations, from the high temperature regime with exponential decay, there is a phase transition where *vortices* start to proliferate. Vortices are topological objects originating from the periodic nature of the phases in the Hamiltonian Equation (1.27). To characterize the vortices, we use the *vorticity* q in a region around which we integrate,

$$\oint d\mathbf{l} \cdot \nabla\theta = 2\pi q. \tag{1.28}$$

The vorticity can be viewed as a positive or negative charge, and this can actually be taken even more literally. In the next section we will demonstrate how the $2DXY$ model with periodic boundary conditions can be mapped onto a neutral two dimensional Coulomb gas where the charges appear in pairs. A corresponding pair of vortices is shown in Figure 1.3. Since the two vortices have opposite rotation, there is no net vorticity, or charge, in this specific configuration of spins.

The phase transition we mentioned is normally referred to as the *Kosterlitz—Thouless* transition [17], and often Berezinskii is also added since he independently contributed to the understanding of the mechanism [16]: The quasi long range order at low temperatures is reflected by a finite stiffness, namely the helicity modulus Υ_μ, associated with twisting the phases. It is given by the second order derivative of the free energy with respect to the total twist δ of the phases

across the system in μ direction,

$$\Upsilon_\mu \equiv \left.\frac{\partial^2 F}{\partial \delta^2}\right|_{\delta=0} = \frac{1}{N}\Big\langle \sum_i \cos(\Delta_\mu \theta_i)\Big\rangle - \frac{1}{NT}\Big\langle \Big[\sum_i \sin(\Delta_\mu \theta_i)\Big]^2\Big\rangle. \tag{1.29}$$

This quantity vanishes discontinuously as vortex pairs proliferate at the phase transition. In a superfluid, Υ_μ is nothing but the superfluid density.

1.3.3 Mapping to the two dimensional Coulomb gas

In this section we will demonstrate a typical mapping for lattice models from a phase representation to a form in which the models are given in terms of their topological objects. Sometimes, this mapping is called a dualization, but following the terminology of Savit [24], a dualization transforms the low temperature region of a model into the high temperature region of its dual counterpart and vice versa. In our particular case of the $2DXY$ model, this is only a part of the mapping, and the temperature in the final model is directly proportional to the temperature in the original. The topological objects are the vortices described above, and in the end we will recognize these as point particles, or charges, interacting through a Coulomb potential.

We begin with the partition function of the XY model

$$Z_{XY} = \int \mathcal{D}\theta \mathrm{e}^{\beta \sum_{i,\mu} \cos(\Delta_\mu \theta_i)}, \tag{1.30}$$

where the phases are restricted to $[0, 2\pi)$. The Villain approximation [25] is applied to obtain

$$Z = \int \mathcal{D}\theta \sum_{\{n\}} \mathrm{e}^{-\frac{\beta}{2} \sum_{i,\mu} (\Delta_\mu \theta_i - 2\pi n_{i,\mu})^2}, \tag{1.31}$$

and this is the only approximation we will make in the transformation. The integer fields $n \in (-\infty, \infty)$ have been introduced to take care of the periodicity of the cosine. The next step is to do a Hubbard–Stratonovich decoupling where every $n_{i,\mu}$ is decoupled from $\Delta_\mu \theta_i$ at the prize of introducing a real valued field $v_{i,\mu} \in (-\infty, \infty)$ in the partition function,

$$Z = \int \mathcal{D}\theta \int \mathcal{D}v \sum_{\{n\}} \mathrm{e}^{-\sum_{i,\mu} [\frac{1}{2\beta} v_{i,\mu}^2 - \mathrm{i}(\Delta_\mu \theta_i - 2\pi n_{i,\mu}) v_{i,\mu}]}. \tag{1.32}$$

Now, we are able to calculate the sum over the integer fields, using the Poisson summation formula,

$$\sum_{n=-\infty}^{\infty} \mathrm{e}^{2\pi \mathrm{i} n v} = \sum_{\hat{v}=-\infty}^{\infty} \delta(v - \hat{v}), \tag{1.33}$$

so that the partition function takes the form

$$Z = \int \mathcal{D}\theta \sum_{\{\hat{v}\}} \mathrm{e}^{-\sum_{i,\mu}[\frac{1}{2\beta}\hat{v}_{i,\mu}^2 - \mathrm{i}\Delta_\mu \theta_i \hat{v}_{i,\mu}]}, \tag{1.34}$$

where the continuous v fields have been promoted to the integer fields $\hat{v}$. A partial summation and subsequent θ integration leaves us with

$$Z = {\sum_{\{\hat{v}\}}}' \mathrm{e}^{-\sum_{i,\mu}\frac{1}{2\beta}\hat{v}_{i,\mu}^2}, \tag{1.35}$$

and the constraint $\Delta_\mu \hat{v}_{i,\mu} = 0$, indicated by the prime in the sum, which we solve by writing $\hat{v}_{i,\mu} = \varepsilon_{\mu\nu}\Delta_\nu \hat{h}_i$. Note here that the new fields $\hat{h}$ are also integer valued and that they are situated on the vertices of a *dual* lattice[1]. The model is now dual to the original $2DXY$ model, but following in the footsteps of Einhorn and Savit [26, 24], we want to write Z in a form which displays explicitly the topological excitations corresponding to vortices. By again using the Poisson summation formula Equation (1.33) to replace $\hat{h}$ with real valued fields h, we get

$$Z = \int \mathcal{D}h \sum_{\{m\}} \mathrm{e}^{-\sum_{i,\mu}[\frac{1}{2\beta}(\Delta_\mu h_i)^2 - 2\pi \mathrm{i} m_i h_i]}, \tag{1.36}$$

with the new integer fields m. Finally, we evaluate the integral over h and find

$$Z_{\mathrm{CG}} = Z_0 \sum_{\{m\}} \mathrm{e}^{-4\pi^2\beta \sum_{i,j} m_i V(\mathbf{r}_j - \mathbf{r}_i) m_j}. \tag{1.37}$$

The interaction $V(\mathbf{r}_j - \mathbf{r}_i)$ between the objects m_i, m_j at positions $\mathbf{r}_i$ and $\mathbf{r}_j$ is the two dimensional lattice Green's function given by

$$\Delta_\mu^2 V(\mathbf{r}_j - \mathbf{r}_i) = \delta_{ij}. \tag{1.38}$$

Furthermore, Z_0 is the partition function of the spin waves, which decouple from the vortex excitations in this approximation. Focusing only on the qualitative features of the model's phase transition, we can safely ignore Z_0 since it is the proliferation of vortex pairs that is responsible for destroying the quasi short range order.

The integer valued objects m_i in Z_{CG} correspond to the vortices in the original $2DXY$ model Equation (1.30) and can be thought of as charges, since

[1] The dual lattice is shifted half a lattice spacing in each direction with respect to the original lattice.

$V(\mathbf{r}_j - \mathbf{r}_i)$ has the form of the Coulomb potential. To avoid divergence, we write the Coulomb gas Hamiltonian as

$$H_{\mathrm{CG}} = 4\pi^2 \Big[\sum_{i \neq j} m_i V(\mathbf{r}_j - \mathbf{r}_i) m_j + V(0) \Big(\sum_i m_i \Big)^2 \Big], \tag{1.39}$$

where the first sum is nonsingular. Now, we see that no configuration with $\sum_i m_i \neq 0$ will contribute to the partition function since $V(0) = \infty$ [27], corresponding to periodic boundary conditions in the $2DXY$ model. In other words, only neutral configurations are possible.

Chapter 2

Monte Carlo simulations

In the previous chapter we only demonstrated what we in principle are able to do if we calculate the partition function Z, but we ignored the obvious difficulties with performing this calculation. Using the Ising model Equation (1.13) in two dimensions as an example, we soon run out of paper trying to write down every term in the partition function as we let the number of lattice sites increase. With 16 sites, there are 2^{16} terms, but we are still far from the thermodynamic limit that we are ultimately interested in. However, this particular model is solved analytically by Onsager [28], and since most models can not be solved, the $2D$ Ising model is frequently employed as a benchmarking model for numerical studies.

In the following we will review the numerical methods used in the studies presented in Chapters 3, 4, and 5.

2.1 Monte Carlo integration

We employ Monte Carlo simulations to estimate thermodynamic quantities as in Equation (1.2), but basically Monte Carlo methods are just a set of related techniques for doing integrals. One of the simplest can be described by considering the integral $I = \int_a^b f(x)\mathrm{d}x$, illustrated as the shaded area in Figure 2.1 (a). In order to estimate I, we randomly pick N values of x, uniformly distributed on the interval $[a, b)$. The estimator is then given by

$$I_{\mathrm{est}} = \frac{(b-a)}{N} \sum_{i=1}^{N} f(x_i), \tag{2.1}$$

and it is clear that in the limit $N \to \infty$ this will converge to the correct value of I. The rate of convergence can however be slow, for instance if $f(x)$ is relatively small in large regions of the interval, as is the case in Figure 2.1 (b). For such a situation, a natural improvement would be to divide the interval into the subintervals $[a, c)$

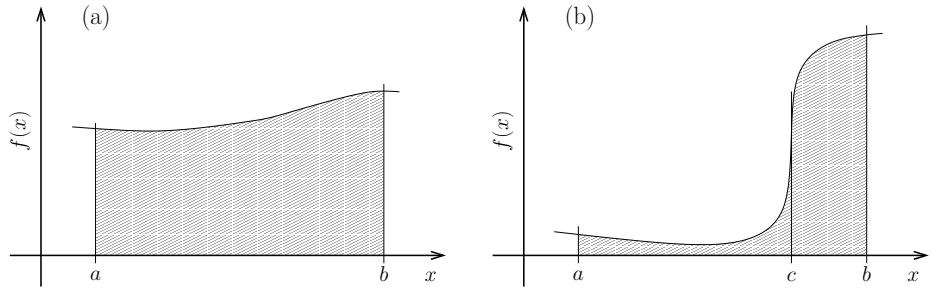

Figure 2.1: The definite integral of a general function $f(x)$ from a to b illustrated as the area below the graph (a). If the function has large variations on the interval $[a, b)$, the integration can be divided into subintervals $[a, c)$ and $[c, b)$ (b).

and $[c, b)$ and instead calculate

$$I_{\text{est}} = \frac{c-a}{N_1} \sum_{i=1}^{N_1} f(x_i) + \frac{b-c}{N_2} \sum_{i=1}^{N_2} f(y_i), \tag{2.2}$$

using N_1 samples x_i from the first interval and N_2 samples y_i from the second. This is a simple version of the principle called *importance sampling* where we try to sample from a nonuniform distribution favoring the most important regions in our integral. A more precise formulation of the method would be to write

$$I_{\text{est}} = \sum_i p^{-1}(x_i) f(x_i), \tag{2.3}$$

i.e. we sample from a probability distribution $p(x)$ and weight the terms in the estimator accordingly.

2.2 Simulating thermodynamics

At this point we go back to our original goal, namely to estimate expectation values of thermodynamic quantities $\langle O \rangle$ Equation (1.2). Both the partition function Z and $\langle O \rangle$ are essentially integrals that can be estimated by the same methods as for I. The variables here are the configurations, or states, ψ consisting of many degrees of freedom and therefore making the integrals harder to estimate than I which has only one single degree of freedom, x. Still, the Monte Carlo methods

are well up to this task. The estimator takes the form

$$\langle O\rangle_{\text{est}} = \frac{\sum_i p_{\psi_i}^{-1} O_{\psi_i} \mathrm{e}^{-\beta H_{\psi_i}}}{\sum_i p_{\psi_i}^{-1} \mathrm{e}^{-\beta H_{\psi_i}}}. \tag{2.4}$$

If the distribution p_{ψ_i} from which we pick the sample configurations ψ_i is chosen equal to the Boltzmann weight,

$$p_{\psi_i} = \mathrm{e}^{-\beta H_{\psi_i}}, \tag{2.5}$$

then the estimator takes the particularly simple form

$$\langle O\rangle_{\text{est}} = \frac{1}{N} \sum_i O_{\psi_i}. \tag{2.6}$$

Here, the sample distribution has cancelled the Boltzmann weights so that neither of them explicitly appear in the calculation.

2.2.1 The Metropolis algorithm

The next important issue in a Monte Carlo simulation is how we should efficiently generate the samples ψ_i. We do this by choosing a dynamics so that the system can evolve in discrete time steps t_i from state to state. Generally this dynamics has little in common with actual physical dynamics, it is only chosen with the purpose of effectively generating new states distributed according to p_{ψ_i}. Consequently, the *Monte Carlo time* t_i is not a physical time scale. Usually, the dynamics is also chosen so that the corresponding series of states ψ_i is a *Markov chain*, and therefore this family of methods is often called Markov chain Monte Carlo methods. A sequence of states is a Markov chain if the probability of moving to a proposed state is only dependent on that state and on the present state, and not on any of the preceding history of states. The most commonly used recipe for the dynamics is the *Metropolis–Hastings algorithm* [29], in physics normally only known as the Metropolis algorithm after its first appearance [30]. We have almost exclusively used this algorithm, however the Multicanonical sampling method [31, 32] was tried at one point during the work of chapter 4 and turned out not to be working very well with that particular model. In Figure 2.2 we summarize the Metropolis–Hastings algorithm applied to the Ising model Equation (1.13). In the algorithm, two important conditions are fulfilled for the Markov chain, namely the *accessibility assumption* and the principle of *microreversibility* [33]. The former demands that it must be possible to reach any configuration of the system from a given starting point through a finite number of iterations. Microreversibility on the other hand is the following requirement,

$$p_{\psi_k} \mathcal{P}_{\psi_k \to \psi_l} = p_{\psi_l} \mathcal{P}_{\psi_l \to \psi_k}, \tag{2.7}$$

1. In a configuration ψ_k choose a site i whose spin variable s_i is to be updated.
2. Propose a change, in this case flip the spin $s_i \to -s_i$ to obtain a new configuration ψ_l.
3. Calculate the energy change $\Delta H = H_{\psi_l} - H_{\psi_k}$.
4. Calculate the acceptance probability $\mathcal{P}_{\psi_k \to \psi_l} = \mathrm{e}^{-\beta \Delta H}$ (if $\mathrm{e}^{-\beta \Delta H} > 1$, set $\mathcal{P}_{\psi_k \to \psi_l} = 1$).
5. Generate a random number r such that $0 < r \leq 1$.
6. If $r \leq \mathcal{P}_{\psi_k \to \psi_l}$ accept the proposed change, else keep the initial configuration ψ_k.
7. Go to 1.

Figure 2.2: The Metropolis–Hastings algorithm. One iteration is called a Monte Carlo step, and going through every site in the lattice once is one Monte Carlo sweep. We define the Monte Carlo time in units of one sweep.

where $\mathcal{P}_{\psi_k \to \psi_l}$ is the transition probability between two states ψ_k and ψ_l. This is sometimes also called *detailed balance*. The factor p_{ψ_k} is the desired probability of being in state ψ_k. Provided that $\mathcal{P}_{\psi_k \to \psi_l}$ meets the condition Equation (2.7), it can be shown that the probability of the system being in state ψ_k at time t_n converges with increasing n to the Gibbs probability $\exp(-\beta H_{\psi_k})/Z$.

2.3 Reweighting

Temperature is normally an input parameter in our simulations, but it is not allways known in advance which temperature is the most interesting. Quantities such as specific heat and the other moments of the energy (Equations (1.10–1.12)), or internal energy histograms may change dramatically as phase transitions are approached – we will encounter this behaviour repeatedly in the models investigated in this work. A helpful tool in this respect is *reweighting*, a set of techniques for utilizing fluctuations in a system around some mean at a specific temperature to gain insight into nearby temperatures [34]. It can be thought of as an advanced form for inter- and extrapolation.

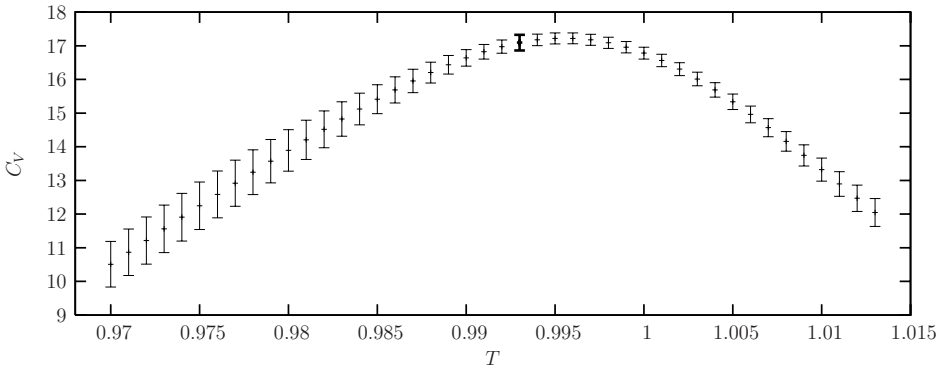

Figure 2.3: The heat capacity of one of the models investigated in this work. The bold data point is calculated directly from data measured during simulations at that temperature. All the other points are reweighted from that single simulation run.

The basic principle of the reweighting we have used is to store the time series (Markov chains) of energies and observables during a simulation. From Equations (1.2) and (2.6) we know how to estimate the expectation value of an observable O at the particular temperature $T_1 = 1/\beta_1$ the simulation was run:

$$\langle O \rangle_{\beta_1} \equiv \frac{1}{Z_{\beta_1}} \sum_{\{\psi\}} O_\psi \mathrm{e}^{-\beta_1 H_\psi} \approx \frac{1}{N} \sum_i O_i. \tag{2.8}$$

An estimate of the same observable at a slightly different temperature $T_2 = 1/\beta_2$ can be found from the original set of data by the following derivation. Consider the somewhat strange observable $O \exp[-(\beta_2 - \beta_1)H]$ with the expectation value

$$\langle O \mathrm{e}^{-(\beta_2-\beta_1)H} \rangle_{\beta_1} = \frac{\sum_\psi \left[O_\psi \mathrm{e}^{-(\beta_2-\beta_1)H_\psi} \right] \mathrm{e}^{-\beta_1 H_\psi}}{Z_{\beta_1}} \approx \frac{1}{N} \sum_i O_i \mathrm{e}^{-(\beta_2-\beta_1)H_i}, \tag{2.9}$$

and yet another observable $\exp[-(\beta_2 - \beta_1)H]$ with expectation

$$\langle \mathrm{e}^{-(\beta_2-\beta_1)H} \rangle_{\beta_1} = \frac{\sum_\psi \left[\mathrm{e}^{-(\beta_2-\beta_1)H_\psi} \right] \mathrm{e}^{-\beta_1 H_\psi}}{Z_{\beta_1}} \approx \frac{1}{N} \sum_i \mathrm{e}^{-(\beta_2-\beta_1)H_i}. \tag{2.10}$$

Note that the latter equation is nothing but the ratio Z_{β_2}/Z_{β_1}. Combining Equations (2.9) and (2.10) we obtain the following estimate for O at T_2,

$$\langle O \rangle_{\beta_2} = \frac{\sum_\psi O_\psi \mathrm{e}^{-\beta_2 H_\psi}}{Z_{\beta_2}} \approx \frac{\sum_i O_i \mathrm{e}^{-(\beta_2-\beta_1)H_i}}{\sum_i \mathrm{e}^{-(\beta_2-\beta_1)H_i}}, \tag{2.11}$$

that is, an estimate based only upon measurements made at temperature T_1. An error analyzis is given in the next section, but we mention briefly here that errors increase when the distance $|\beta_2 - \beta_1|$ increases. As a rule of thumb, the energy

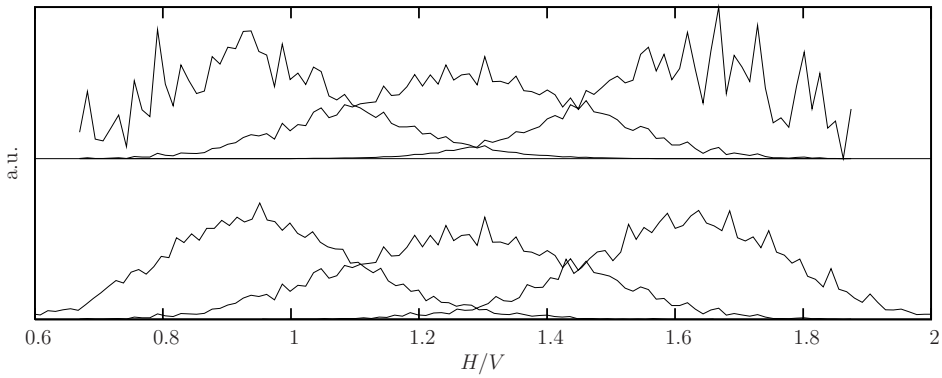

Figure 2.4: Energy histograms from a Monte Carlo simulation for three different temperatures. In the top panel, only the histogram in the middle is actually obtained from simulations, whereas the other two are calculated from the former through reweighting. In the lower panel, direct measurements for all three temperatures are showed.

histograms for the system at T_1 and T_2 should have substantial overlaps. In Figure 2.4 we see that the reweighting is satisfactory as long as the energy fluctuations of the original data provides information on the energies in the reweighted histograms. Originally the method was expressed in terms of these histograms instead of the Markov chains of H_i and O_i directly. The drawback then is that observables have to be functions of the energy, whereas in the present formulation H and O are both functions of the configuration.

2.3.1 Multiple histogram reweighting

In our work, we have used a more advanced version of reweighting though the underlying principles are the same. *The multiple histogram reweighting* by Ferrenberg and Swendsen [35] improves the quality of the estimates by combining data in time series obtained from simulation runs at several different temperatures, see Figure 2.5. This involves solving a set of nonlinear equations self consistently, and can be quite tricky to implement properly. Fortunately we have been provided with a software package developed by Rummukainen (first used in Reference [36]) which has been highly appreciated in several works of our research group for almost a decade.

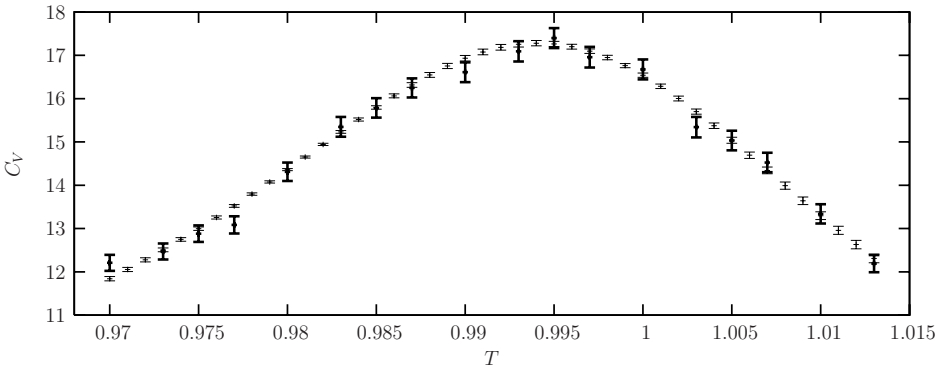

Figure 2.5: The heat capacity of the same system as in Figure 2.3. This time, all the bold points where simulated and combined to produce the significantly improved intermediate points by using multiple histogram reweighting.

Additionally, we have lately used a related method implemented by Hove [37], aimed at calculating the density of states $g(H)$, from which we can derive expectations of essentially all thermodynamic observables O as long as they can be written in terms of the energy H,

$$\langle O \rangle_\beta = \frac{\sum_H O(H) g(H) \mathrm{e}^{-\beta H}}{\sum_H g(H) \mathrm{e}^{-\beta H}}. \tag{2.12}$$

The free energy is given by

$$F(T) = -T \ln\Big[\sum_H g(H) \mathrm{e}^{-\beta H}\Big], \tag{2.13}$$

and from this, moments of the energy can be derived through Equations (1.10–1.12).

In principle the two methods should yield the same results when analyzing identical Markov chains of simulation data, and they have similar limitations. A simulation performed at a given finite temperature does not provide information of the full range of energies in $g(H)$, and insight into which energies are covered can again be found in the energy histograms of the raw data. However, the density of states method does not fail as easy if there are insufficient overlaps between some of the raw histograms involved, as is the case in the process of solving sets of nonlinear equations in the multiple histogram method.

2.4 Error analysis

An important part of calculating estimates or taking measurements in physics, is to estimate corresponding errors. For a set of N uncorrelated measurements $O_1, O_2, O_3, ..., O_N$, the error is just the standard error estimated from the sample variance S^2,

$$\delta\langle O\rangle_{\text{est}} = \sqrt{S^2/N} = \sqrt{\frac{\sum_{i=1}^{N}(O_i - \langle O\rangle_{\text{est}})^2}{N(N-1)}}. \tag{2.14}$$

In typical Monte Carlo simulations however, the samples are highly correlated due to their originating Markov chain. The degree of correlation can be quantified through the autocorrelation function

$$\phi(t) = \frac{\langle O_{s+t}O_s\rangle - \langle O\rangle^2}{\langle O^2\rangle - \langle O\rangle^2}, \tag{2.15}$$

where O_s is a sample taken from a simulation at Monte Carlo time s. In a Markov chain $\phi(t)$ is proportional to $\exp(-t/\tilde{t})$ for large t. Close to a critical point the characteristic time $\tilde{t}$ can be very large, and in fact in the thermodynamic limit it diverges as T_C is approached. This phenomenon is known as *critical slowing down*. Large correlation times can cause problems in two respects. First of all, when we start a simulations, we want the system to *thermalize*, that is we want the system to relaxe and fluctuate around its global energy minimum. The number of Monte Carlo sweeps required to reach such a situation depends on the initial conditions as well as on the autocorrelation time $\tilde{t}$. There is no general recipe for determining the relaxation time, but a pragmatic way is to start sampling from the beginning of the simulation, and then in the post processing stage try to exclude a various number of the first samples before calculating the means. Provided that the simulation has been run for a sufficiently long total Monte Carlo time, an appropriate number of samples have been excluded when an estimate $\langle O\rangle_{\text{est}}$ does not seem to depend appreciably on further increasing the number of excluded samples. It should be noted here that there may be more than one relaxation time in the problem. Various observables may therefore require different thermalization times.

2.4.1 Correlated measurements

The second problem of a large correlation time, is that the error can no longer be calculated directly from Equation (2.14). Several methods exist for taking correlations into account, but we will focus on the jackknife method [38], where the full data set of N samples is divided into M subsets $\{\varphi_1, \varphi_2, \varphi_3, ..., \varphi_M\}$.

From these subsets we calculate $M-1$ estimates

$$\langle O\rangle_j = \frac{M}{(M-1)N}\sum_{i\notin\varphi_j} O_i \tag{2.16}$$

where the samples in subset φ_j are excluded from the sum. Along with the mean of the complete set,

$$\langle O\rangle_{\text{est}} = \frac{1}{N}\sum_{i=1}^{N} O_i, \tag{2.17}$$

we can then calculate the error estimate

$$\delta\langle O\rangle_{\text{est}} = \sqrt{\frac{M-1}{M}\sum_{j=1}^{M}\left(\langle O\rangle_j - \langle O\rangle_{\text{est}}\right)^2}. \tag{2.18}$$

Each subset φ_j should contain measurements taken over a time interval much larger than $\tilde{t}$. A simpler method only for finding simple averages of the sampled quantities O is simply to consider the means

$$Q_j = \frac{M}{N}\sum_{i\in\varphi_j} O_i \tag{2.19}$$

of each subset as uncorrelated stochastic variables, calculate the estimator $\langle O\rangle_{\text{est}}$ based on these Q_j, and then use the expression for sample variance Equation (2.14) with O replaced by Q. However, we often want to calculate complicated and nonlinear functions of the sampled quantities, for instance in the process of reweighting. This can be done quite straightforwardly using the estimates Equations (2.16) repeatedly as arguments of the functions, and calculating the corresponding errors of the function using Equations (2.18) this time with O replaced by the function itself.

2.5 Finite size scaling

Ultimately, when we do simulations we hope to apply the results to physical systems in the thermodynamic limit, but external limitation such as storage capacity and computer performance obviously limit the size of the simulated systems. Addititionally there are intrinsic properties of the models that restrict us from studying too large numerical grids: The above mentioned critical slowing down in the vicinity of phase transitions grows increasingly severe when increasing the system size and there will consequently be more correlations in the Markov chain. Hence, the statistics will deteriorate due to the larger correlations, forcing

us to raise the number of Monte Carlo steps. This trade-off between large systems versus accurate statistics is allways an important issue in Monte Carlo methods.

To exploit the information in results from finite systems, we do *finite size scaling*. That is, we look for scaling behaviour in observed quantities when varying the system size L. It turns out that close to critical points many thermodynamic quantities obey power-law dependence on the system size because the *correlation length* ξ diverges as $\tau^{-\nu}$, but is limited by L in a finite system. The exponents in these power-laws can be related to critical exponents such as β in Equation (1.15). Estimates of the critical exponents can in turn be used to classify the nature of a phase transition.

A full treatment of the subject should involve the renormalization group theory [39], but in the present works this has not been directly touched, and the reader is referred to the literature, see e.g. References [12, 40, 33]. Instead we turn to Widom's homogeneity postulate [41] that the singular part of the free energy F_s obeys the following relation,

$$F_s(\lambda^a \tau) = \lambda F_s(\tau), \tag{2.20}$$

where λ is an arbitrary scaling factor and a is an unknown constant. Since we want an expression for the scaling of F_s with respect to L, it is natural to choose $\lambda^a = L^{1/\nu}$ to obtain the explicit L-dependence as $\tau \to 0$,

$$F_s(\tau, L) = L^{1/(a\nu)} F_s(L^{1/\nu}\tau). \tag{2.21}$$

From Equations (1.9) and (1.11), we know that the heat capacity C_V is proportional to the second derivative of the free energy with respect to temperature, so the leading behaviour close to T_C can be found from

$$C_V \propto \frac{\partial^2 F_s}{\partial \tau^2} = L^{2/\nu + 1/(a\nu)} \mathcal{F}(L^{1/\nu}\tau). \tag{2.22}$$

$\mathcal{F}(x)$ is just some derivative of F_s and analytical in x. The singular part of the heat capacity is normally given as $C_V \sim |\tau|^{-\alpha}$, and from this we identify $a = 1/(2-\alpha)$. Thus, by measuring C_V at T_C for different system sizes, we can extract the ratio α/ν from

$$C_V \propto L^{\alpha/\nu}. \tag{2.23}$$

Similar scaling arguments for other thermodynamic quantities lead to a set of relations coupling the corresponding exponents, and from the *hyperscaling relation*,

$$d\nu = 2 - \alpha, \tag{2.24}$$

we can calculate α and ν. However, hyperscaling is known to be violated in certain systems [18].

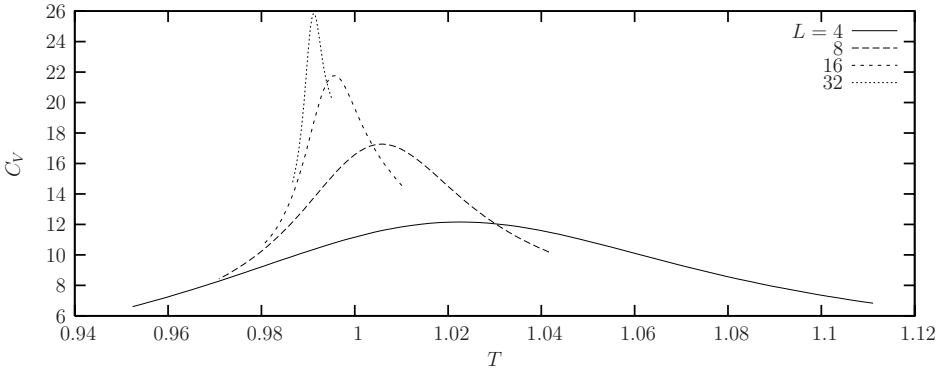

Figure 2.6: The heat capacity of a system with a phase transition in the $3DXY$ universality class. Equation (2.23) predicts that the peak should be close to constant when increasing the system size, since α is very small and even slightly negative. However, finite size effects in the nonsingular part of C_V obscure this behaviour for small L.

2.5.1 The third moment of the energy

When the α exponent is close to zero, or even slightly negative as in the $3DXY$ model[1], reliable results are hard to obtain from C_V due to significant deviations from scaling in small systems. Equation (2.23) is *asymptotically* correct, but as shown in Figure 2.6, the heat capacity can actually increase with L because the analytic background dominates over the singular part for small L. In References [13, 14] Sudbø and coworkers presented a solution to this problem by, rather than computing C_V, using the third moment of the energy Equation (1.12),

$$M_3 \equiv \frac{\partial^3 F_s}{\partial \tau^3} = L^{(1+\alpha)/\nu} \mathcal{F}'(L^{1/\nu}\tau), \tag{2.25}$$

shown in Figure 2.7. Here, it is the peak-to-peak height $(\Delta M_3)_{\text{height}}$ that scales as $L^{(1+\alpha)/\nu}$, and linear background terms will cancel as a result of subtraction. Additionally M_3 provides a direct measure for the only length scale in the problem through the peak-to-peak *width*, which scales according to

$$(\Delta M_3)_{\text{width}} \propto \tau \sim L^{-1/\nu}. \tag{2.26}$$

The hyperscaling relation Equation (2.24) is no longer needed since M_3 provides independent measures for α and ν.

[1] High precicion measurements yield $\alpha \simeq -0.0146(8)$ [42].

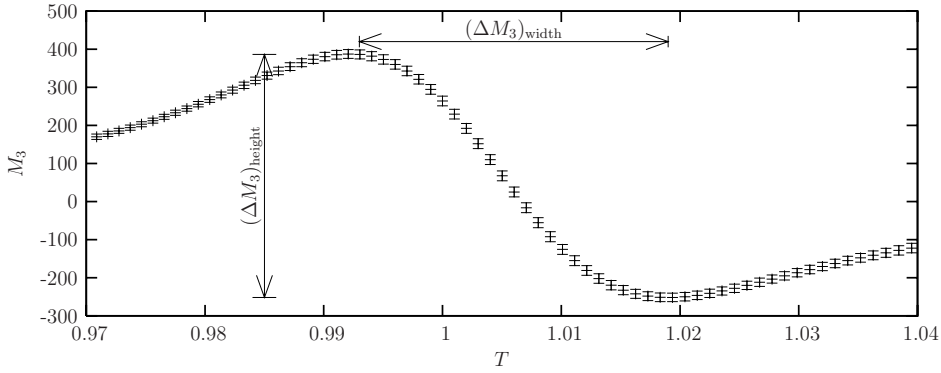

Figure 2.7: The third moment of the energy, corresponding to the $L = 8$ data for the heat capacity in Figure 2.6.

2.5.2 Beyond continuous transitions

So far, we have only considered continuous transitions in our finite size discussion. Berezinskii–Kosterlitz–Thouless transitions are different in that there is no single temperature where the correlation length ξ diverges. Instead, we stated in section 1.3.2; the entire low temperature phase is critical, and there exists no local order parameter we can monitor. Still, a finite size analysis is useful and often the helicity modulus Υ_μ Equation (1.29) has been used to estimate the transition temperature through finite size deviations from its bulk form [43, 44]. In full analogy, the inverse dielectric constant ϵ^{-1} has been used in the two dimensional Coulomb gas [27, 45, 46]. More conclusive evidence from Monte Carlo simulations for the very existence of a Berezinskii–Kosterlitz–Thouless in a model, is hard to find, but a novel method was proposed by Minnhagen and Kim in Reference [47]. We have further developed the method and we will come back to this in Chapter 3.

At a first order transition there are two or more noncritical phases coexisting, and no ordinary diverging correlation length is associated with the switching between them, even though quantities such as the heat capacity diverge. However, it is possible to consider first order transitions as limiting cases of continuous transtitions [48, 49] where finite size scaling still makes sense. The critical exponents then attain corresponding limiting values, in particular $\alpha = 1$ and $\nu = 1/d$.

2.6 The Lee–Kosterlitz method for first order transitions

Finite size scaling and determination of the critical exponents as described above, may give a good indication on the nature of a phase transition. Yet, a more direct approach put forward by Lee and Kosterlitz [50, 51] allows us to be more definitive about the nature of the transitions after analyzing Monte Carlo data. The idea is to identify and do finite size scaling of the domain wall energy between the coexisting phases at a first order transition. The domain walls have a surface tension corresponding to a free energy barrier $\Delta F(L)$, which vanishes for continuous transitions whereas it scales as L^{d-1} at a first order transition provided that L is sufficiently large.

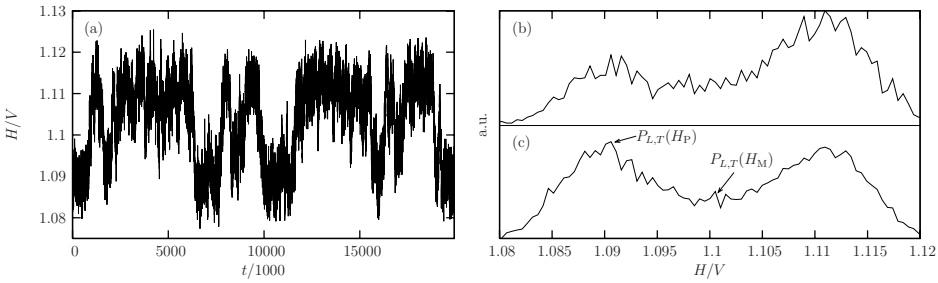

Figure 2.8: The Monte Carlo time series of the energy (a) indicates that there are two coexisting phases between which the system jumps. The raw histogram of the data (b) can be reweighted to a nearby temperature (c) where the two peaks are of the same height, corresponding to the transition temperature. Finite size scaling of the barrier height between the two phases will then determine the nature of the phase transition.

To calculate $\Delta F(L)$ we again turn to the energy histograms we referred to in the context of reweighting in section 2.3, and again reweighting itself is a valuable tool. For long simulations, these histograms directly estimate the probability distribution $P_{L,T}(H)$ for the energy H at a given system size and temperature. Two coexisting phases are reflected by two peaks in $P_{L,T}(H)$ which are of the same height precicely at the transition temperature. Generally we do not know that exact temperature, but the histograms can then be reweighted, and from the equal height histogram $\Delta F(L)$ can be found as

$$\Delta F(L) = \ln\left(\frac{P_{L,T}(H_{\mathrm{P}})}{P_{L,T}(H_{\mathrm{M}})}\right). \tag{2.27}$$

Here, H_{P} is the energy of one of the two pure states for which $P_{L,T}(H)$ has a

maximum, and H_{M} is the mixed state energy corresponding to the minimum between the two peaks in the histogram as shown in Figure 2.8.

Chapter 3

Logarithmic plasmas in two and three dimensions

In the papers [1, 2] we study a closely related model of the Ginzburg–Landau model Equation (1.18), with focus on three dimensions arising out of a quantum mechanical problem in *two* spatial dimensions as briefly discussed in section 1.3. The study is motivated by the work in References [52, 53] where a Berezinskii–Kosterlitz–Thouless phase transition is proposed in a matter coupled compact U(1) gauge theory. This is hoped to be applicable to the proposed phenomenon of spin–charge separation in strongly correlated electron systems at zero temperature.

3.1 Strongly correlated electron systems

Many of the properties of high temperature superconductors can not be described by the successful theory of Bardeen, Cooper, and Schrieffer [54] for the conventional superconductors. The main issue is the strong Coulomb repulsion between the electrons with resulting breakdown of fermi liquid theory in the non superconducting phases of cuprate superconductors. For a better understanding of the cuprates, the physics of Mott insulators is considered to be crucial.

3.1.1 The Hubbard model

An appearantly simple model accounting for the strong electron repulsion, is the Hubbard model,

$$H = -t \sum_{\langle i,j\rangle,\sigma} C^\dagger_{i\sigma} C_{j\sigma} + U \sum_i n_{i\uparrow} n_{i\downarrow} + \text{H.c.}, \tag{3.1}$$

in the large $U/|t|$ limit. $C^\dagger_{i\sigma}$ and $C_{j\sigma}$ are the usual creation and destruction operators for electrons with spin $\sigma = \uparrow, \downarrow$, and $n_{i\sigma} = C^\dagger_{i\sigma} C_{i\sigma}$ is the number of electrons at lattice site i with spin σ. As $U/|t| \to \infty$, double occupancy of a lattice site is prohibited even if the electrons are of opposite spins, as illustrated in

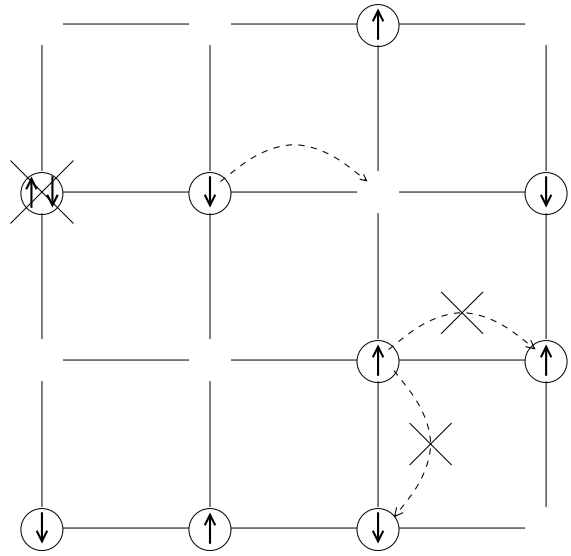

Figure 3.1: Possible dynamics of the large $U/|t|$ Hubbard model. Hopping to an occupied site is not allowed even if the electrons have opposite spins.

Figure 3.1. At half filling this limit of the Hubbard model is a nearest neighbour Heisenberg antiferromagnet, believed to be an effective model for the parent compound of the cuprate superconductors, La_2CuO_4. The ground state of the system is a Mott insulator, but doping may introduce new phases. The crystal of La_2CuO_4 has a layered structure of essentially independent square Cu lattices on which the low energy electron dynamics takes place [55]. In the $U/|t| \to \infty$ limit we write the hamiltonian

$$H = -t \sum_{\langle i,j \rangle, \sigma} C^\dagger_{i\sigma} C_{j\sigma} + \text{H.c.}, \tag{3.2}$$

where we now have the additional constraint

$$\sum_\sigma C^\dagger_{i\sigma} C_{i\sigma} \leq 1, \tag{3.3}$$

expressing the prohibition of double occupancy. Instead of dealing with this inequality, we represent the electron operators by

$$\begin{aligned} C^\dagger_{i\sigma} &= f^\dagger_{i\sigma} b_i, \\ C^\dagger_{i\sigma} &= f_{i\sigma} b^\dagger_i, \end{aligned} \tag{3.4}$$

called the slave boson method.

The operators $f^\dagger_{i\sigma}$ and $b^\dagger_i$ create a chargeless fermionic spin and a spinless bosonic hole respectively, and the constraint consequently takes the form of an equality,

$$Q_i|\Phi\rangle \equiv \sum_\sigma (f^\dagger_{i\sigma} f_{i\sigma} + b^\dagger_i b_i)|\Phi\rangle = |\Phi\rangle, \tag{3.5}$$

i.e. the site i is either occupied by a fermionic spin or else it is a positively charged hole.

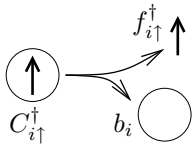

Figure 3.2: Slave bosonization where an electron is represented as the composite particle of a spinon carrying the spin and a holon carrying the charge.

3.1.2 Effective lattice gauge theory

In order to do statistical mechanics we want the partition function Z, and this we find as a Feynman path integral over Grassmann and complex fields f and b respectively [21, 56],

$$\begin{aligned} Z = \int \mathcal{D}f^*\mathcal{D}f\mathcal{D}b^*\mathcal{D}b \prod_{i,\tau} \delta(Q_i - 1) \exp\Big\{ - \int_0^\beta \mathrm{d}\tau \\ \Big[\sum_{\langle i,j\rangle,\sigma} \Big(f^*_{i\sigma}(\partial/\partial\tau) f_{i\sigma} + b^*_i(\partial/\partial\tau) b_i + \text{H.c.} \Big) + H \Big] \Big\}, \end{aligned} \tag{3.6}$$

where we have incorporated the constraint Equation (3.5) in the theory through the factors $\prod_{i,\tau} \delta(Q_i - 1)$. H is the hamiltonian of Equation (3.2) and τ is imaginary time. We then use Abrikosov's trick of writing

$$\delta(Q_i - 1) = \int_{-\pi}^{\pi} \frac{\mathrm{d}\lambda_i}{2\pi} \mathrm{e}^{-\mathrm{i}\lambda_i(Q_i - 1)}, \tag{3.7}$$

so that the partition function can be written

$$\begin{aligned} Z = \int \mathcal{D}f^*\mathcal{D}f\mathcal{D}b^*\mathcal{D}b\mathcal{D}\lambda \exp\Big\{ - \int_0^\beta \mathrm{d}\tau \\ \Big[\sum_{\langle i,j\rangle,\sigma} \Big(f^*_{i\sigma}(\partial/\partial\tau) f_{i\sigma} + b^*_i(\partial/\partial\tau) b_i + \mathrm{i}\lambda_i(Q_i - 1) + \text{H.c.} \Big) + H \Big] \Big\}. \end{aligned} \tag{3.8}$$

The important feature here is that the original constraint Equation (3.3) appears in the theory in the form of a *compact gauge field* $\lambda_i \in [-\pi, \pi)$. After decoupling the quartic fermion terms in H by a Hubbard–Stratonovich transformation [57], the fermion sector can be integrated out. Left is a theory of a compact gauge field coupled to a bosonic field with the fundamental charge. A simplified model believed to capture the essential physics is the abelian Higgs model with a compact U(1) gauge field $\mathbf{A}$ fundamentally[1] coupled to a bosonic U(1) matter field $\Psi = |\Psi| \mathrm{e}^{\mathrm{i}\theta}$ defined on a Euclidian $(2+1)$ dimensional lattice [58]. In the London limit, we may write the effective hamiltonian

$$H = -\sum_{i,\mu} \Big[\cos(\Delta_\mu \theta_i - A_{i\mu}) + \kappa \cos(\varepsilon_{\mu\nu\lambda} \Delta_\nu A_{i\lambda}) \Big]. \tag{3.9}$$

The charge part in the underlying theory is represented by the matter field, whereas the constraint is fulfilled by fluctuations in the gauge field. We want to see if the model can support spin–charge separation in a so-called *confinement–deconfinement* transition, since a frozen gauge field would correspond to independent dynamics of the slave fermions and bosons. It should be mentioned here that this is also closely related to the issue of quark confinement in high energy physics [59].

It has long been established that a pure compact gauge theory without matter fields sustains a permanent confining phase in three dimensions [60]. Such a theory supports stable topological defects defined by surfaces where the field jumps by 2π, forming a gas of space-time instantons. These are point like objects interacting through a $1/r$ potential, analogous to a three dimensional Coulomb gas where the charges are always in a metallic phase due to Debye screening. If matter fields are present the fate of the instantons is however less clear. It has been argued that this does not destroy the permanent confinement [58, 59], but there has been much controversy on this point [61, 62, 63, 52, 53, 64, 65, 66, 67, 68].

In References [52, 53] a duality transformation is demonstrated for the model Equation (3.9) where the theory is expressed in terms of the gauge field instantons q_i,

$$H = \frac{1}{2} \sum_{i,j} q_i V_{ij} q_j. \tag{3.10}$$

On a $d = (2+1)$ dimensional lattice the interaction can be expressed through a discrete Fourier transformation,

$$V_{ij} \equiv V(\mathbf{r}_j - \mathbf{r}_i) = \frac{4\pi^2}{N a^d} \sum_{\mathbf{k}} \frac{\mathrm{e}^{\mathrm{i}\mathbf{k}\cdot(\mathbf{r}_j - \mathbf{r}_i)}}{[2(d - \sum_{\alpha=1}^{d} \cos k_\alpha a)]^{d/2}}. \tag{3.11}$$

[1] The *fundamental charge* $e = 1$ is omitted but would appear in the theory in the coupling term $\cos(\Delta_\mu \theta_i - e A_{i\mu})$.

Here, the presence of a matter field has modified the interaction from $\sim 1/r$ in the pure gauge theory to an anomalous $-\ln r$ interaction in the matter coupled version. This is very similar to the *two dimensional* Coulomb gas of section 1.3.3 which is known to exhibit a Berezinskii–Kosterlitz–Thouless phase transition. Furthermore, renormalization group arguments are used to indicate that also the three dimensional logarithmic gas may undergo a phase transition of this type. A phase transition in such a system would correspond to a proliferation of space-time instantons in the gauge theory Equation (3.9). This is in turn hoped to serve as a possible mechanism for spin–charge separation through a confinement–deconfinement transition in strongly correlated systems.

As a remark, it should be mentioned that if the matter field carries a charge other than the fundamental $e = 1$, the situation is very different, and the model is known to have a continuous phase transition [14].

3.2 Numerical studies of a metal–insulator transition

The two dimensional Coulomb gas has enjoyed much attention over the last decades, see e.g. References [69, 70, 45, 27, 46, 71], and can therefore be considered as a model with well known properties. A review of the model is given in Reference [72]. Due to its similarities with our three dimensional logarithmically interacting gas of instantons, we have studied these two models simultaneously for direct comparison and benchmarking purposes. Additional comparisons with the three dimensional Coulomb gas have also been made.

Figure 3.3: In the two dimensional Coulomb gas, dipoles unbind in a Berezinskii–Kosterlitz–Thouless phase transition to form a metallic plasma.

Screening of the interaction potential is the essential property responsible for a phase transition in the two dimensional Coulomb gas. A finite screening length means that the system is a metallic plasma. On the other hand, since dipoles can-

not screen the Coulomb potential [73], a system initially consisting of dipoles will be in a stable dielectric phase where opposite charges are tightly bound in pairs. In two dimensions these pairs break and unbind at a finite temperature through the Berezinskii–Kosterlitz–Thouless phase transition, whereas there is only one stable phase in the *three dimensional* Coulomb gas. A permanent metallic phase in the latter model corresponds by duality to the permanent confinement of the pure U(1) gauge theory [60].

3.2.1 Polarizability

The theorem that dipoles cannot screen does however not apply to the *logarithmic* potential in three dimensions. This warrants numerical investigations, and in Reference [1] we use Monte Carlo simulations to investigate the screening properties of such a system. Information on this is provided by the dielectric constant, given in a low density approximation as

$$\epsilon = 1 + n_d \Omega_d p, \tag{3.12}$$

where n_d is the dipole density and Ω_d the solid angle in a d dimensional system. The polarizability p is proportional to the mean square separation $\langle s^2 \rangle$ between the charges in a dipole, and by focusing on this quantity in the simulations we can determine wether the system is a dielectric or a metal. For the two dimensional Coulomb gas, the behaviour of $\langle s^2 \rangle$ to leading order in L can be found using a low density argument [17] yielding

$$\langle s^2 \rangle = \begin{cases} \text{Const.} & ; \ T < T_{KT} \\ aL^{(T-T_{KT})/T} & ; \ T_{KT} < T < 2T_{KT} \\ bL^2 & ; \ 2T_{KT} < T. \end{cases} \tag{3.13}$$

Here, the prefactors a and b are unimportant, whereas the constant for $T < T_{KT}$ is of the order of the lattice constant. Even though the screening effects were neglected in this calculation, the conclusion still holds – the only correction due to screening in the above result is in value of the transition temperature T_{KT} [17]. Monte Carlo simulations confirmes this behaviour in two dimensions, and the three dimensional logarithmic gas shows a remarkably similar behaviour, see Figure 3.4.

These results demonstrates clearly the existence of two different temperature regimes in the models. The scaling with L of the polarizability has a nonanalytic change at some intermediate temperature, and there must therefore be a phase transition separating the two regimes. The nature of the transition can however not be determined from the above, and further investigations are necessary. This will be presented in the next section.

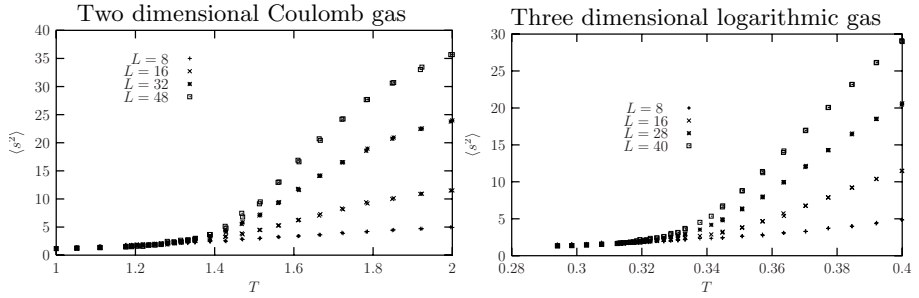

Figure 3.4: Results from Monte Carlo simulations showing two distinct temperature regimes in both models for the mean square dipole moment $\langle s^2 \rangle$.

3.2.2 Numerical evidence of a Berezinskii–Kosterlitz–Thouless transition

A Berezinskii–Kosterlitz–Thouless phase transition is characterized by a universal jump to zero in some generalized stiffness parameter [16, 17]. In the $2DXY$ model, this is the helicity modulus Υ_μ (Equation (1.29)), whereas the inverse dielectric constant ϵ^{-1} is the corresponding quantity in the two dimensional Coulomb gas. Due to the finite sizes used in computer simulations, it is diffi-

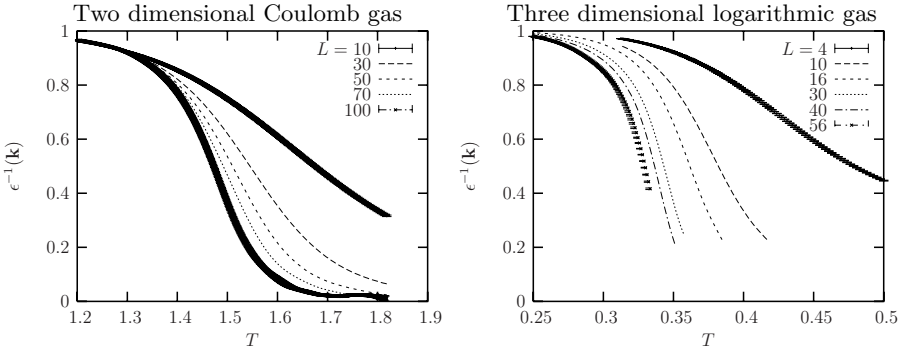

Figure 3.5: The inverse dielectric constant $\epsilon^{-1}(\mathbf{k})$ as a function of the temperature T, using the smallest possible wave vector in a finite system, $\mathbf{k} = 2\pi\hat{\mathbf{e}}_y/L$.

cult to prove a dicontinuity in ϵ^{-1} or Υ_μ on numerical grounds. The plots in Figure 3.5 shows that the drop towards zero gets steeper as the system size is increased, but this alone does not guarantee a discontinuity in the thermodynamic limit. Yet, a simple and elegant method to prove this characteristic feature in

such phase transitions from Monte Carlo simulations, was recently put forth by Minnhagen and Kim [47]. They considered the $2DXY$ model and its helicity modulus Υ_μ, defined by Equation 1.29. This is the coefficient of the second order term in a free energy expansion in an imposed phase twist: An arbitrarily small perturbation δ that *inreases* the free energy. Since only even order terms are nonzero in this expansion, the next term is of fourth order and the expansion can be written

$$\Delta F = F(\delta \neq 0) - F(\delta = 0) = \pi_2 \, \delta^2 + \pi_4 \, \delta^4 + ..., \tag{3.14}$$

where $\pi_2 \propto \Upsilon_\mu$. The simple argument is that if the fourth order coefficient can be proven to be finite and negative at the transition temperature in the thermodynamic limit, then the helicity modulus has to be finite and positive in order to maintain stability of the system. If Υ_μ goes to zero at the transition, it necessarily cannot do so in a continuous fashion.

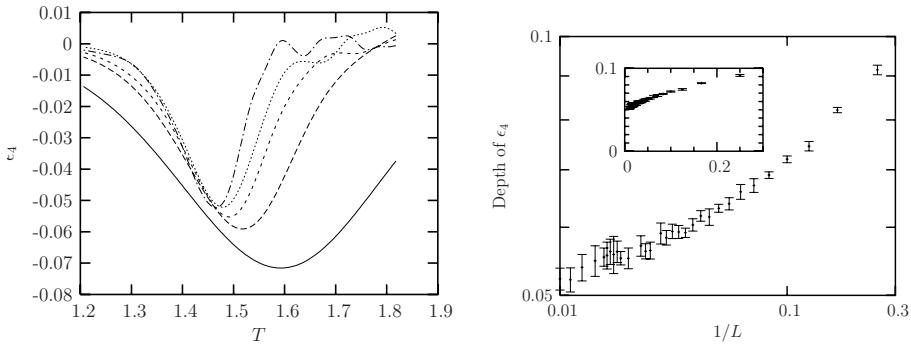

Figure 3.6: For the two dimensional Coulomb gas, the coefficient ϵ_4 of the fourth order term in the free energy expansion is finite and negative at the transition temperature. In the left panel ϵ_4 is plotted for increasing system size and the depth decreases monotonically with L.

We have applied the same stability argument to our logarithmically interacting plasmas in two and three dimensions, and derived the following coefficients in the corresponding free energy expansion [2]. The second order term is proportional to the inverse dielectric constant,

$$\epsilon^{-1}(\mathbf{k}) = 1 - \frac{V_\mathbf{k}}{L^3 T} \langle q_\mathbf{k} q_{-\mathbf{k}} \rangle, \tag{3.15}$$

and the fourth order term is proportional to

$$\epsilon_4(\mathbf{k}) \equiv \frac{1}{T^3} \left(\langle q_\mathbf{k} q_{-\mathbf{k}} \rangle^2 - \frac{1}{2} \langle (q_\mathbf{k} q_{-\mathbf{k}})^2 \rangle \right). \tag{3.16}$$

$V_{\mathbf{k}}$ and $q_{\mathbf{k}}$ are the interaction and point charge respectively, given in the Fourier representation defined by $f_{\mathbf{k}} = \sum_{\mathbf{k}} f(\mathbf{r}) \exp(\mathrm{i}\mathbf{k} \cdot \mathbf{r})$. Some care had to be taken in the choice of perturbation in order to make the change in free energy Equation (3.14) nondivergent as $L \to \infty$. In our choice $\mathbf{k}$, is either of the d smallest possible vectors $\mathbf{k} = 2\pi\hat{\mathbf{e}}_\mu / L$ in the given system.

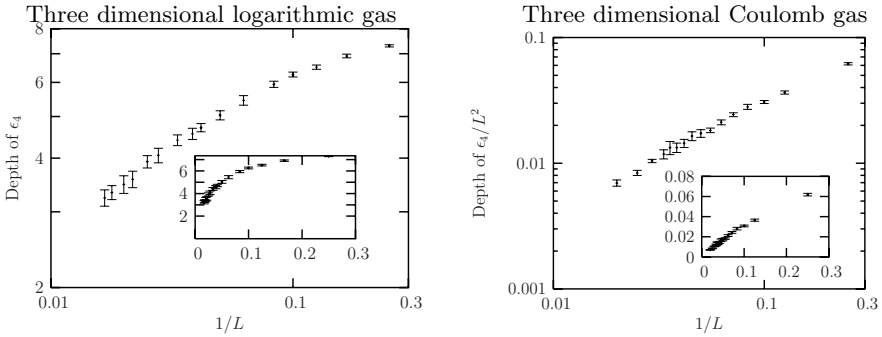

Figure 3.7: The depth of the fourth order coefficient vanishes in the thermodynamic limit for the $3DCG$ model (ϵ_4 is divided by L^2 in order to obtain the corresponding nondivergent quantity in this case). In the logarithmically interacting model, no such conclusions can be drawn.

For the two dimensional Coulomb gas, we confirm the results obtained in Reference [47]. The results (Figure 3.6) are similar to those for the $2DXY$ model, and thus establish the discontinuous character of the inverse dielectric constant based on finite size scaling of ϵ_4. The minimum of the fourth order coefficient can safely be associated with the phase transition where ϵ^{-1} goes to zero. By plotting the corresponding temperature against $1/L$ and extrapolating to the limit $L \to 0$, we can estimate the transition temperature T_{KT}, but the convergence to the known value of T_{KT} is however slow and the method is consequently not very precise.

The Berezinskii–Kosterlitz–Thouless characteristic of a discontinuous jump in the inverse dielectric constant for the three dimensional logarithmic gas can not be ruled out. Unfortunately though, the feature turns out to be hard to prove or disprove from computer simulations alone. The fourth order term has the same characteristic shape as for the $2DCG$ model, and scaling of the depth is shown in Figure 3.7 along with results from simulations of the three dimensional Coulomb gas. In the latter case, the depth of the corresponding quantity ϵ_4/L^2 vanishes in the thermodynamic limit whithout any doubt. However, the results from the three dimensional logarithmic gas are inconclusive and either improved methods or larger system sizes are required.

Chapter 4

Deconfined criticality

In this chapter we use the term *deconfinement* in a somewhat different meaning than that of spin–charge separation in Chapter 3. We will however still be concerned with the physics of Mott insulators in two spatial dimensions in search for better understanding of the cuprate superconductors, but the approach will be different. Materials such as La_2CuO_4 and Cs_2CuCl_4 feature states with an odd number of $S = 1/2$ spins per unit cell, but can also *dimerize* so that each unit cell consists of two $S = 1/2$ spins, spontaneously breaking the lattice symmetry [74]. It is the dimerization of spins that in this specific context is named *confinement*. These states are paramagnetic valence bond solids and may exhibit a gap to spin excitations.

In paper [3] we study an effective model proposed by Senthil and coworkers [74, 75, 76] for the transition from a quantum Heisenberg antiferromagnet with Néel order to a dimerized spin gap state on a two dimensional square lattice. They claim that this order–order transition is continuous, in contradiction to what would be expected from the Landau–Ginzburg–Wilson framework for phase transitions. The antiferromagnetic Néel order corresponds to a broken SU(2) symmetry in spin space, whereas the valence bond solid state breaks the discrete translational symmetry in real space. According to the Landau–Ginzburg–Wilson paradigm a transition between two such ordered states must either be of first order, or there must be an intermediate disordered region. However, quantum interference effects can obscure this picture and the confining order of the two phases may be separated by a critical region where the order parameters are deconfined.

4.1 Square lattice antiferromagnet

The quantum Heisenberg antiferromagnet can be described by the Hamiltonian

$$H_S = J \sum_{\langle ij \rangle} \mathbf{S}_i \cdot \mathbf{S}_j + ... \tag{4.1}$$

on a square two dimensional lattice, where $\mathbf{S}_i$ are $S = 1/2$ spin operators and the nearest neighbour coupling $J > 0$. The groundstate is the desired Néel state,

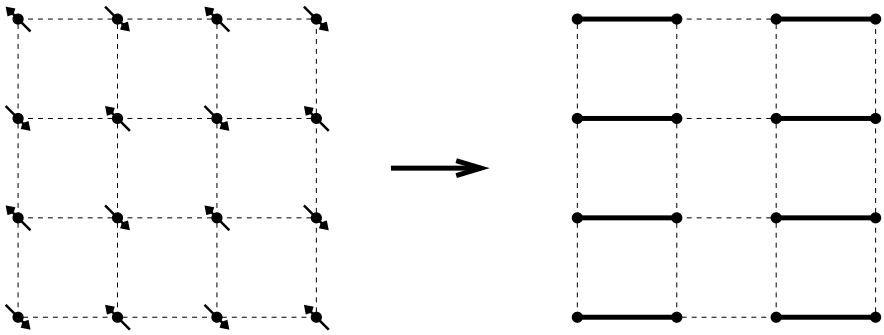

Figure 4.1: Schematic examples of a Néel ordered antiferromagnet and a valence bond dimer state where the discrete translational symmetry is broken.

and by adding additional terms in the Hamiltonian, it is possible to tune the system through transistions into other states such as the paramagnetic valence bond solid in Figure 4.1.

Now, a similar procedure to the one in the previous chapter can be followed to obtain an effective model for quantum fluctuations about the Néel state. It is believed that the essential physics of this system is captured by the path integral $Z_B = \int \mathrm{D}\theta^{(1)}\mathrm{D}\theta^{(1)}\mathrm{D}\mathbf{A}\exp(-H)$, with the effective $(2+1)$ dimensional Hamiltonian [74, 75, 76],

$$H = -\sum_i \Big\{ \beta \sum_\mu \Big[\cos(\Delta_\mu \theta_i^{(1)} - A_{i\mu}) + \cos(\Delta_\mu \theta_i^{(2)} - A_{i\mu}) + \kappa \cos(\varepsilon_{\mu\nu\lambda}\Delta_\nu A_{i\lambda}) \Big] + \mathrm{i}2S\eta_i A_{i\tau} \Big\}. \tag{4.2}$$

Here, both the phases $\theta^{(1)}, \theta^{(2)}$ and the gauge field $A_{i\mu}$ are compact, i.e. they are only defined on the interval $[-\pi, \pi)$. Even though the compact abelian Higgs model Equation (3.9) has many similarities with the above Hamiltonian, there are a few important differences to be explained. The most prominent is the so-called *Berry phase* term $\mathrm{i}2S\eta_i A_{i\tau}$, accounting by a phase factor for the evolution in imaginary time τ of each spin S_i [77, 78]. The spins are described in this theory with the identification $\mathbf{S}_i = \eta_i S \mathbf{n}_i$, where $\mathbf{n}_i$ is a unit vector and $\eta_i = \pm 1$ is a staggering factor making $\mathbf{n}_i$ a slowly varying function of i close to the Néel ordered groundstate. η_i is constant in the time direction. Furthermore, in order to simplify the model, an easy-plane anisotropy is assumed so that the SU(2) symmetry of the spins is reduced to the U(1) group where spins are locked to the xy plane. The Néel vector can then be parametrized in terms of the two

component spinor $z_i = (\mathrm{e}^{\mathrm{i}\theta^{(1)}}, \mathrm{e}^{\mathrm{i}\theta^{(2)}})/\sqrt{2}$,

$$\mathbf{n}_i = z_i^\dagger \vec{\sigma} z_i, \tag{4.3}$$

where $\vec{\sigma}$ is a vector of Pauli matrices. In the limit of large β the partition function Z_B is dominated by configurations with small fluctuations in the phases $\theta^{(1)}, \theta^{(2)}$. This corresponds to the Néel ordered state with a finite $\mathbf{n}_i$, and $\theta^{(1)} - \theta^{(2)}$ represents the direction of $\mathbf{n}_i$. The valence bond order on the other hand is connected to the factor $\exp\left[-\mathrm{i}\sum 2S\eta_i A_{i\tau}\right]$ in Z_B, as the Berry phases lead to a broken lattice symmetry for small β.

The compact gauge field of the effective Hamiltonian Equation (4.2) gives rise to the same topological defects as in the compact abelian Higgs model Equation (3.9), but now these instantons carry Berry phases. Exactly at the critical point, the combined effect of compactness and Berry phases makes the instantons cancel each other completely [74, 75, 76]. In other words, the critical theory can equally well be described by the noncompact theory

$$H = -\beta \sum_{i,\mu} \Big[\cos(\Delta_\mu \theta_i^{(1)} - A_{i\mu}) + \cos(\Delta_\mu \theta_i^{(2)} - A_{i\mu}) - \frac{\kappa}{2} (\varepsilon_{\mu\nu\lambda} \Delta_\nu A_{i\lambda})^2 \Big], \tag{4.4}$$

and this argument applies to arbitrary number of components $\theta^{(\rho)}$.

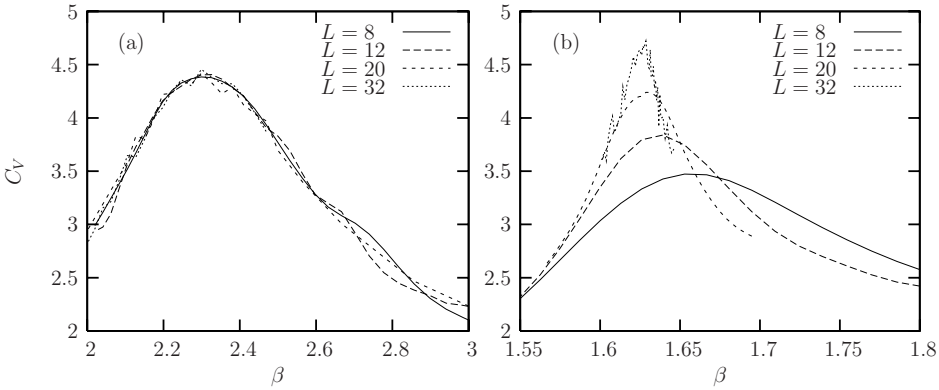

Figure 4.2: The peak in the heat capacity for a model with one matter field coupled to a compact gauge field does not indicate a diverging behaviour (a). If an additional Berry phase term is present (b), the heat capacity scales consistently with the $3DXY$ model.

If we were to consider only one component, we know from the previous chapter that with a compact gauge field and no Berry phase term we get a model with no

ordinary continuous phase transition. However, if the Berry phases are included, then the critical properties would be that of the inverted $3DXY$ universality class[1]. In Figure 4.2 we plot the heat capacity for the single component version of the model Equation (4.2) with and without Berry phases, and the effect is clear: The version without Berry phases shows no sign of scaling behaviour. On the other hand, for the model with the Berry phase term present, scaling of the corresponding third moment of the energy Equation (1.12) yields critical exponents in consistency with the $3DXY$ universality class. Our main focus will be on the two component version of the model, however the same mechanism takes place: The Berry phases and instantons cancel each other at the critical point.

4.1.1 Dualization to avoid a complex hamiltonian

The effective model in the form of Equation (4.2) is difficult perform Monte Carlo simulations on because it is complex. The imaginary Berry phase term may cause the partition function Z_B to contain negative terms, and consequently the normalizing factor $1/Z_B$ in the expectation value of an observable Equation (1.2) may easily diverge. This is known as the sign problem and often encountered in quantum Monte Carlo simulations [79]. Fortunately, we are in a position where we can recast the model into a real Hamiltonian through a duality transformation akin to the one in section 1.3.3.

First we apply the Villain approximation which leaves the partition function in the form

$$Z = \int \mathrm{D}\theta^{(1)}\mathrm{D}\theta^{(1)}\mathrm{D}\mathbf{A} \sum_{\{\mathbf{n}^{(1)},\mathbf{n}^{(2)},\mathbf{n}^{(A)}\}} \mathrm{e}^{-H_V}, \tag{4.5}$$

with

$$H_V = \sum_i \Big\{ \frac{\beta}{2} \sum_\mu \Big[\Big(\Delta_\mu \theta_i^{(1)} - A_{i\mu} + 2\pi n_{i\mu}^{(1)} \Big)^2 + \Big(\Delta_\mu \theta_i^{(2)} - A_{i\mu} + 2\pi n_{i\mu}^{(2)} \Big)^2 + \kappa \Big(\varepsilon_{\mu\nu\lambda} \Delta_\nu A_{i\lambda} + 2\pi n_{i\mu}^{(A)} \Big)^2 \Big] + \mathrm{i}2S\eta_i A_{i\tau} \Big\}. \tag{4.6}$$

Then we employ the standard set of tricks: The Hubbard-Stratonovich transformation and the Poisson summation formula which enable us to integrate out the $\theta^{(1)}$ and $\theta^{(2)}$ fields as well as the gauge field $A_{i\mu}$. Appearantly, the partition function now becomes particularly simple,

$$Z = \sum_{\{\mathbf{v}^{(1)},\mathbf{v}^{(2)},\mathbf{v}^{(A)}\}} \mathrm{e}^{-\frac{1}{2\beta}\sum_i \left({\mathbf{v}_i^{(1)}}^2 + {\mathbf{v}_i^{(2)}}^2 + \frac{1}{\kappa} {\mathbf{v}_i^{(A)}}^2 \right)} \tag{4.7}$$

[1] An abelian Higgs model in three dimensions with a noncompact gauge field is dual to the $3DXY$ model [24].

but then it must meet the following constraints,

$$\Delta \cdot \mathbf{v}_i^{(\rho)} = 0 \qquad \text{where } \rho = 1, 2, \tag{4.8}$$

$$\varepsilon_{\mu\nu\lambda}\Delta_\nu v_{i\lambda}^{(A)} - v_{i\mu}^{(1)} - v_{i\mu}^{(2)} - \delta_{\mu\tau}\eta_i = 0 \qquad \text{where } \mu = x, y, \tau. \tag{4.9}$$

The constraints of Equation (4.8) are fulfilled by writing $v_{i\mu}^{(1)} = \varepsilon_{\mu\nu\lambda}\Delta_\nu h_{i\mu}^{(1)}$, $v_{i\mu}^{(2)} = \varepsilon_{\mu\nu\lambda}\Delta_\nu h_{i\mu}^{(2)}$, where $\mathbf{h}_i^{(1)}, \mathbf{h}_i^{(2)}$ are dual lattice fields. If we additionally write the staggering term $\delta_{\mu\tau}\eta_i$ as the curl of a new static field $\mathbf{f}_i$, the last constraint can be written

$$\varepsilon_{\mu\nu\lambda}\Delta_\nu\Big(v_{i\lambda}^{(A)} - h_{i\lambda}^{(1)} - h_{i\lambda}^{(2)} - f_{i\lambda}\Big) = 0, \tag{4.10}$$

and will be met if the parenthesis equals the gradient of a discrete scalar field s_i. Solving for $\mathbf{v}_i^{(A)}$,

$$v_{i\lambda}^{(A)} = h_{i\lambda}^{(1)} + h_{i\lambda}^{(2)} + f_{i\lambda} + \Delta_\lambda s_i, \tag{4.11}$$

we end up with the real and gauge invariant *dual* partition function

$$\begin{aligned} Z = \sum_{\{\mathbf{h}^{(1)},\mathbf{h}^{(2)},s\}} \exp\Big\{-\frac{1}{2\beta}\sum_{i\mu}\Big[\Big(\varepsilon_{\mu\nu\lambda}\Delta_\nu h_{i\lambda}^{(1)}\Big)^2 + \Big(\varepsilon_{\mu\nu\lambda}\Delta_\nu h_{i\lambda}^{(2)}\Big)^2 \\ + \frac{1}{\kappa}\Big(h_{i\mu}^{(1)} + h_{i\mu}^{(2)} + f_{i\mu} + \Delta_\lambda s_i\Big)^2\Big]\Big\}. \end{aligned} \tag{4.12}$$

The gauge invariance in Equation (4.12) allows us to choose a gauge in which the gradient term is zero and the scalar field s_i consequently is absent in the theory. In principle, we could proceed from here and express the theory in terms of its topological excitations as we did for the $2DXY$ model, but the corresponding Hamiltonian then again turns out to be complex.

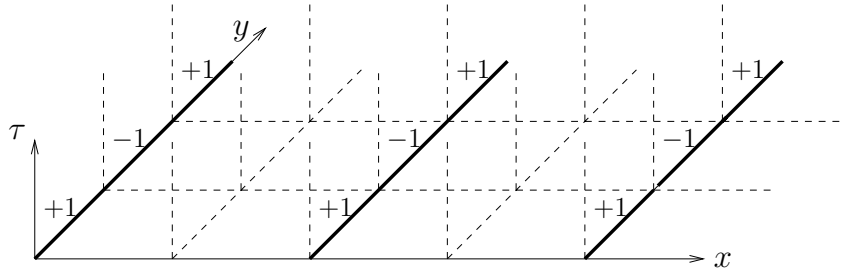

Figure 4.3: The components of $\mathbf{f}_i = (f_{ix}, f_{iy}, f_{i\tau})$ are interpreted as link variables: All components are zero except for the solid links which are given the indicated values. Additionally, there is no variation in the τ direction.

4.2 Monte Carlo study of a first order transition

In paper [3] we present large scale Monte Carlo simulations of the model Equation (4.12) in the $\Delta_\mu s_i = 0$ gauge. This is a faithful representation of the two component effective theory Equation (4.2) for the Néel order to valence bond solid transition. Here, the Berry phases are represented by the field $\mathbf{f}_i$, which is defined only so that it satisfies $\varepsilon_{\mu\nu\lambda}\Delta_\nu f_{i\lambda} = \delta_{\mu\tau}\eta_i$, and we conveniently use the choice of Reference [74], see Figure 4.3.

However, by setting $\mathbf{f}_i = 0$, we can easily study the compact model *without* the Berry phases as well. It is known that such a theory can be rewritten in terms of a neutral mode of the XY type and a charged mode which couples to the gauge field [80, 81, 82]. Because of the compactness, the latter mode is just of the type we investigated in Chapter 3 with no continuous phase transition. Hence, we expect this theory to be in the $3DXY$ universality class, which is in good agreement with our simulation results.

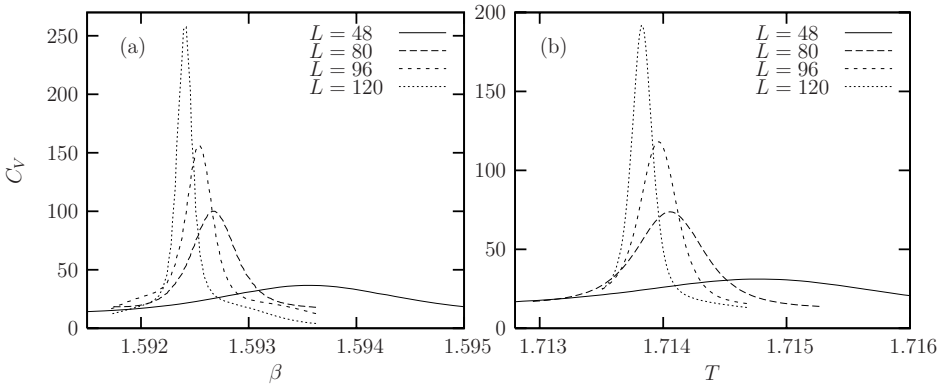

Figure 4.4: The heat capacity as a function of β or temperature respectively for the two component model with compact gauge field and Berry phases (a), and for the two component noncompact model. The symmetric peaks develop into delta functions in the thermodynamic limit, a characteristic of first order phase transitions

Finally, we perform Monte Carlo simulations on the noncompact version of the model, Equation (4.4). If the two cosine terms appear in the Hamiltonian with unequal prefactors - or phase stiffnesses - this theory is believed to be applicable to exotic systems like the Hydrogen atom at extreme pressure [83]. As in the case of a compact gauge field, we can express Equation (4.4) by a charged and a neutral mode. However this time, even the charged mode gives rise to a phase transition of $3DXY$ type. When on the other hand the phase stiffnesses are

equal as in the present study, the theory can be shown to be *self dual* [84], in contradiction to the asymmetric $3DXY$ phase transition.

It is argued that the critical properties of the compact model with Berry phases and the noncompact model are identical [74, 75, 76], and indeed we obtain similar results from the Monte Carlo simulations. In Figure 4.4, we see that the peaks in the heat capacity are almost perfectly symmetric in both models, and scaling of the third moment of the energy reveals practically identical critical exponents. These exponents are however surprisingly different from previous investigations [84, 82], and hint that the nature of the phase transition is not continuous, rather than *first order*. To settle this issue we have carried out a Lee–Kosterlitz analysis (see Section 2.6) and find strong evidence for a first order phase transition in these models. Thus, the peaks in the heat capacity are actually developing delta functions.

Chapter 5

Thermal fluctuations in trapped vortex systems

Extending the XY model from two to three dimensions, the topological objects described in section 1.3.3 becomes lines instead of points. These are vortices, objects found in systems ranging from the giant internal structure of neutron stars [85], to tiny containers of rotating superfluid ^{4}He [86], and to extreme weather conditions like tornadoes and cyclones. In the context of high T_C superconductors, the ordering and interactions among larger numbers of vortices have been a deep and rich field of research for decades, see for example References [87, 88, 83, 89].

In certain regimes of physical parameters the $3DXY$ model turns out to be well suited for investigations of vortex systems [90, 22, 91, 92], and the computer programs developed for the Monte Carlo studies of the last two chapters can be applied with small modifications to this problem [4]. The problem we have in mind is thermal fluctuations in arrays of vortices seen in ultracold rotating gases of bosons, the Bose–Einstein condensates. At the lowest temperatures, these arrays have a high degree of regularity [93], ordered as Abrikosov lattices, the well known form for ordering of quantized magnetic flux lines in type-II superconductors [94]. The Bose–Einstein condensates have superfluid properties, and since their experimental realization in alkali gases just over a decade ago [95, 96], they have proved to be useful testing grounds for a variety of different physical concepts. An important reason for this is that they are easily controllable in large ranges of the parameters such as total particle number, density, interparticle interaction, rotation rates and so on.

Our Monte Carlo results are believed to be applicable to harmonically trapped Bose–Einstein condensates [93] away from the extremely dilute limit of rapidly rotating systems where the rotation frequency is close to the trap frequency [97]. With small additional adjustments we have also simulated anharmonic situations where the condensate is trapped in a harmonic plus quartic potential, directly related to experiments by Bretin and coworkers [98]. Another related case is to replace the trap by a hard-walled cylinder with a uniform bare phase stiffness within, resulting in a model applicable to a rotating container of superfluid ^{4}He [99].

5.1 Trapped Bose–Einstein condensates

Here, we will not review the fundamentals of Bose–Einstein condensation other than refer to a few concepts important for this work - more general introductions can be found in References [100, 101]. In order to confine the condensate atoms in space, various techniques can be used, however most experiments have a magnetic trap with axial symmetry. The potential is usually that of a harmonic oscillator and can be written

$$V(r,z) = const. + \frac{1}{2}M\omega_r^2 r^2 + \frac{1}{2}M\omega_z^2 z^2, \tag{5.1}$$

where M is the single particle mass and ω_r (ω_z) is the radial (axial) oscillator frequency. By tuning the ratio ω_r/ω_z, the shape of the system can be manipulated. We will consider elongated systems where the cloud of condensed atoms have a cigar shape, with extension Z in z direction a few times larger than the radial extension R. In certain setups the cloud can take the form of a pancake, leaving the physics essentially two dimensional, but in the present study $3D$ effects are important.

The size of the cloud can be estimated by simple energy considerations. In a system of N atoms rotating around the z axis with an angular rotation frequency Ω, the rotating frame energy is

$$E_{\text{cloud}} \sim \frac{1}{2}M(\omega_r^2 - \Omega^2)R^2 N. \tag{5.2}$$

In order to maintain stability, this must be comparable to the total interaction energy

$$E_{\text{int}} \sim gnN, \tag{5.3}$$

with $g = 4\pi a_s \hbar^2/M$ the interaction strength and n the condensate density. Here is a_s the low energy s-wave scattering length. Assuming for simplicity a qubic system, then $n = N/R^3$, and we get

$$E_{\text{cloud}} \sim E_{\text{int}} \tag{5.4}$$

$$\Rightarrow R \sim \left[\frac{gN}{M(\omega_r^2 - \Omega^2)}\right]^{1/5}. \tag{5.5}$$

We see that when the rotation rate approaches the trap frequency, the system flies apart and other trapping methods are necessary to confine the atoms, see for example Reference [98]. Otherwise, changing the total number of atoms in the trap offers great flexibility for controlling the size and density of the system. If N is sufficiently large, the Thomas–Fermi approximation can be applied to give the following radial density distribution of the atoms [101],

$$n(r) = n(0)\Big(1 - (r/R)^2\Big). \tag{5.6}$$

Close to $r = R$ where the density is small, the approximation is not good and the condensate vanishes more smoothly than predicted by Equation (5.6). In a rotating system where vortices appear, the density profile $n(r)$ must be viewed as the coarse grained density since a vortex core corresponds to a complete depletion of the condensate. The vortex core size is of the same order of magnitude as the healing length, $\xi \sim \hbar/\sqrt{gnm}$.

Typical experiments with Na or ^{87}Rb may have N in the range of 10^5-10^7 atoms, and trapping frequency of the order 100 Hz. For example, in Reference [93] this yields systems of up to 130 vortices with cloud size $R \sim 29\mu$m and healing length $\xi \sim 0.2\mu$m.

5.2 The frustrated, nonuniform $3DXY$ model

In paper [4] we present results obtained by Monte Carlo simulations of a frustrated $3DXY$ model with a position dependent, but fixed, bare phase stiffness. The *uniform* $3DXY$ model has been used extensively for over a decade in the context of high T_C superconductors [90, 22, 91, 92] and is assumed to work well when the average vortex separation is larger than the healing length ξ. On the contrary, when the vortex cores start to overlap as in very rapidly rotating Bose–Einstein condensates, the systems enter the lowest Landau level regime [102, 103] and the $3DXY$ model does not apply. This happens when the interaction energy is much smaller than the harmonic trap energy.

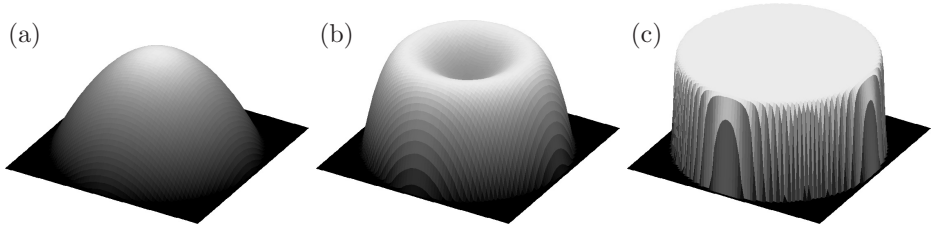

Figure 5.1: Various radial density distribution P_{ij} used in our simulations: With a harmonic trap (a), an anharmonic trap with a harmonic plus a quartic term (b), and a hard-walled cylindric container (c).

We use a Hamiltonian which is a generalization of Equation (1.27) and can be written

$$H = -\sum_{\langle ij \rangle} P_{ij} \cos(\theta_j - \theta_i - A_{ij}). \tag{5.7}$$

The bare phase stiffness P_{ij} can be chosen so as to represent the Thomas–Fermi

density profile of a harmonically trapped Bose–Einstein condensate,

$$P_{ij} = \begin{cases} \left(1 - (r_{ij}/R)^2\right) & \text{when } r_{ij} \leq R, \\ 0 & \text{when } r_{ij} > R, \end{cases} \tag{5.8}$$

where r_{ij} is the radial distance from the z directed trap center axis. However, as far as the simulations are concerned, we can equally well choose other profiles, see Figure 5.1. The gauge field A_{ij} in Equation (5.7) is kept fixed during the simulations, and serves as a uniform frustration which induces a certain number of vortices in the system corresponding to some fixed rotation frequency Ω. It is defined by

$$A_{ij} = \int_i^j \mathrm{d}\mathbf{l} \cdot (2\pi f x \hat{\mathbf{e}}_y), \tag{5.9}$$

and in a qubic $L \times L \times L$ lattice, there will consequently be fL^2 vortex lines penetrating the system parallel to the z axis. The position of these vortices are

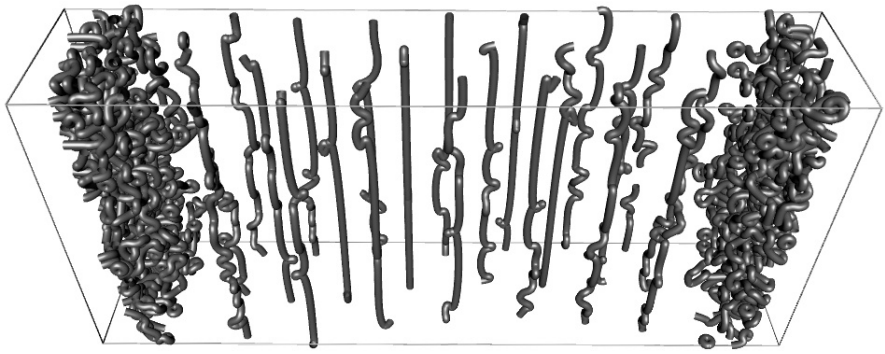

Figure 5.2: A snapshot of the vortices in a 72×72×72 system at $T = 0.5$, where the selection consists of 72 lattice spacings in x direction, 16 in y direction, and 32 in z direction. In the central part there are small fluctuations and the vortex lines are almost straight objects, whereas fluctuations increase and vortex loops eventually proliferate closer to the edge. The radius of the vortices is 0.4 times the lattice spacing, only *chosen* so for visualization reasons, and should not be compared to the physical size of the vortex cores.

determined by calculating around each plaquette $\square_k$ the sum

$$\sum_{\square_k} (\theta_j - \theta_i - A_{ij}) = 2\pi n_k, \tag{5.10}$$

where the integer n_k is the number of vortices penetrating that particular plaquette in the positive direction. Fluctuations of the phases θ_i are responsible for

the dynamics of the vortex lines, but can also cause the creation of closed vortex loops in the system. High temperature favours fluctuations and so the amount of vortex *loops* increase with increasing temperature. Since temperature appears in the partition function only through the prefactor $\beta = 1/T$, we can view the total prefactor βP_{ij} as an effective, position dependent inverse temperature. Hence, in the trapped system we expect large vortex fluctuations close to the edge and gradually more of a low temperature phase in the central parts. In Figure 5.2 a snapshot of a typical vortex configuration is shown for a relatively small T. Surface effects where the vortex lines leave or enter the system are ignored in this study by use of periodic boundary conditions. A qubic model system can therefore be considered as a section of an elongated cloud.

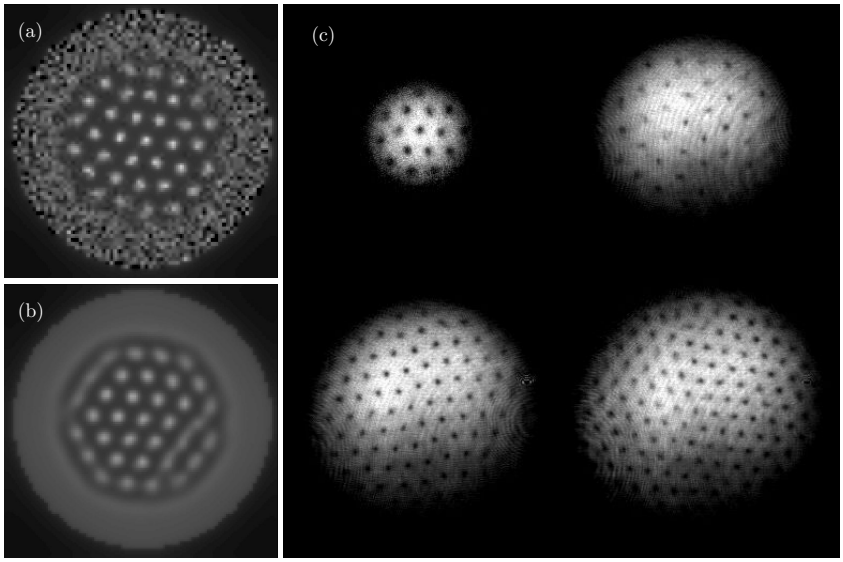

Figure 5.3: The vorticity in a simulation snapshot, integrated along the z direction (a). In (b) such snapshots are averaged over every tenth of $5{\cdot}10^5$ Monte Carlo sweeps in order to produce a thermal average. Experimental pictures (c) usually reflects density variations in the cloud, and vortices are only indirectly visible through the absence of the condensate. Image cortesy (c) Wolfgang Ketterle [104].

5.2.1 Vortex position average

We want to monitor how the presence of a harmonic trap affects the vortex fluctuations and use Monte Carlo simulations on the nonuniform $3DXY$ model

Equation (5.7) to produce snapshots of vortex configurations. Normally, Monte Carlo simulations are used to calculate thermal averages from large numbers of configurations. Now however, we hope to mimick the experimental situation in which the pictures indeed are snapshots.

For a given vortex configurations, we integrate the vorticity over the z direction and in this way obtain two dimensional visualizations of the three dimensional vortex systems. An example is shown in Figure 5.3 (a). In such a picture, two closed vortex loops situated on top of each other will cancel out if they are opposite in direction. On the other hand, straight vortex *lines* will be sharply defined spots, with bent lines being more smeared out regions. The main difference of these pictures from most of the pictures taken in experiments (see e.g. Figure 5.3 (c)), is that the intensity in the latter reflects local density variations in the condensate cloud, whereas in the simulated pictures, it is the vortex matter that is visualized. In real systems, vortices correspond to depletion of the condensate density and are thus only indirectly visible. Still, both visualizations provide information on the vortex position.

However, an additional feature of the simulation pictures, is that we can also do thermal averages of vortex configurations. Then, large phase fluctuations will correspond to many closed vortex loops effectively cancelling each other out, leaving behind only the sample penetrating vortex lines. Stable vortex lattice regions will remain clear in such pictures, whereas in molten regions where the vortex lines can move, the pictures will be blurred as shown in Figure 5.3 (b).

5.2.2 Modified helicity modulus

In the pictures of the above section, we notice a rather sharp boundary between the ordered vortex line lattice and the disordered region outside, possibly a molten phase. In order to investigate this boundary we employ a modified version of the helicity modulus Υ_μ. From investigations on high T_C superconductors, it is known that the superconducting to normal transition can be characterized by the vanishing of the helicity modulus: When vortex lines are present, Υ_z is discontinuous because the vortex line lattice melts in a first order phase transition [22, 92]. The helicity modulus is proportional to the superfluid density ρ_s, and can be defined in a uniform system as the lowest order response in the free energy with respect to an infinitesimal phase twist across the system in μ direction. In that sense, Υ_μ can be considered as the measure of an effective phase stiffness, renormalized by vortex fluctuations. Since the free energy is a global quantity, Υ_μ has no rigorous meaning in the trapped system where the bare phase stiffness P_{ij} depends on position. Nevertheless, we introduce a modified helicity modulus $\tilde{\Upsilon}_z$ only defined between two cylinders of radii R_1 and R_2. We do so by applying

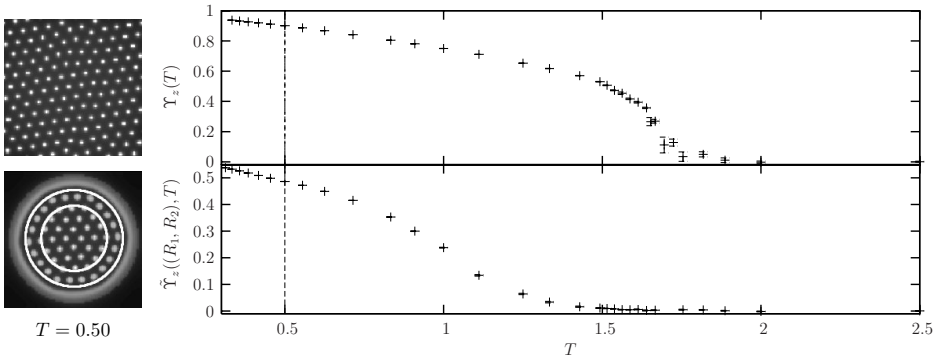

Figure 5.4: A comparison between the ordinary helicity modulus Υ_z of a uniform system with vortex lines (top row), and the modified version $\tilde{\Upsilon}_z$ (lower panel). The radii R_1 and R_2 for wich $\tilde{\Upsilon}_z$ is calculated, are indicated by the white circles in the picture on the left. Due to the larger effective temperature $1/(\beta P_{ij})$ in this region, the stiffness vanishes at lower T than in the uniform system.

a twist

$$\boldsymbol{\Delta}(r_{ij}) \equiv \boldsymbol{\Delta}_{ij} = \begin{cases} \Delta \hat{\mathbf{e}}_z & \text{if } R_1 \leq r_{ij} < R_2, \\ 0 & \text{otherwise,} \end{cases} \tag{5.11}$$

to the model Eq. (5.7) to get a twist dependent energy function

$$H_{\text{trap}}(\Delta) = -\sum_{\langle ij \rangle} P_{ij} \cos(\theta_j - \theta_i - A_{ij} - \frac{1}{L} \boldsymbol{\Delta}_{ij} \cdot \hat{\mathbf{e}}_{ij}), \tag{5.12}$$

where $\hat{\mathbf{e}}_{ij}$ is the unit direction vector of link ij. The cylinder version of the helicity modulus can then be defined

$$\begin{aligned} \tilde{\Upsilon}_z(R_1, R_2) \equiv \left. \frac{\partial^2 F'}{\partial \Delta^2} \right|_{\Delta=0} &= \frac{1}{N'} \left\langle {\sum}' P_{ij} \cos(\theta_j - \theta_i - A_{ij}) \right\rangle \\ &- \frac{1}{TN'} \left\langle {\sum}' \Big[P_{ij} \sin(\theta_j - \theta_i - A_{ij}) \Big]^2 \right\rangle \end{aligned} \tag{5.13}$$

where $\sum'$ is over all links where $\boldsymbol{\Delta}_{ij}$ is nonzero (depends on R_1 and R_2) and N' is the number of these links. The total free energy F of the system will have contributions due to the large gradient in the phase twist normal to the surfaces defined by R_1 and R_2, and we therefore *choose* only to calculate the response in free energy F' for the subsystem between the two surfaces. It is clear that in the

limit where the volume of this subsystem goes to infinity, $\tilde{\Upsilon}_z$ converges to Υ_z. Yet, we also believe that the modified helicity modulus is a useful probe of the states in a finite system. This is further discussed in paper [4].

5.2.3 Renormalized density

An alternative way of visualizing the vortex lattice is to create two dimensional plots similar to those in Section 5.2.1, but this time integrating *density* rather than vortex positions. The density is estimated simply by associating the underlying lattice constant of the numerical grid with the vortex core size: A unit cell in the grid has density $1/L$ if it is empty and 0 if it is penetrated by a vortex. This we integrate along the z direction and modulate with the a priori density given by P_{ij}. The resulting two dimensional plots now provides information both on the vortex line lattice structure and on the density of the condensate cloud itself, renormalized by vortex fluctuations.

This is directly comparable to the experimental pictures, and in particular, we consider [105] results from experiments performed by Bretin and coworkers [98]. They used a trap with an additional quartic term in order to confine the atoms

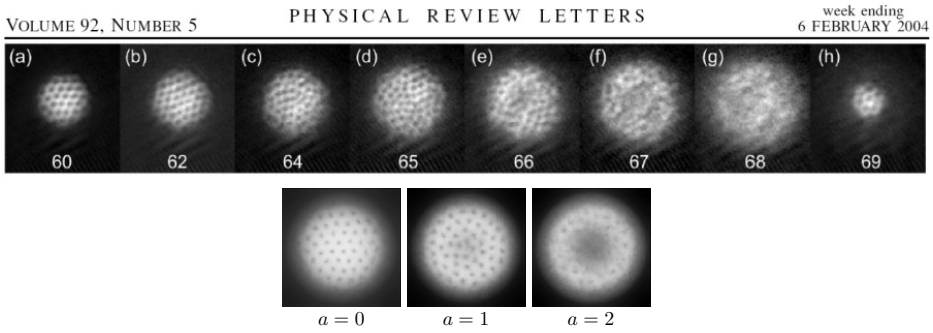

Figure 5.5: Observation of vortices in an experiment where the condensate was confined by a harmonic plus quartic potential (top row), after Bretin and coworkers [98]. Renormalized condensate density from simulations with a similar density profile is shown in the bottom row. Note the loss in visibility when the strength of the harmonic term increases, corresponding to faster rotation relative the trap frequency.

even when approaching the harmonic trap frequency ω_r. An unexplained feature in their results was the loss in visibility of the vortices at high rotation rates (see Figure 5.5), which we believe is due to the reduced density in the central parts of the cloud. Such a reduction is readily interpreted as an increased effective

temperature leading to enhanced fluctuations when incorporated through the trap factor

$$P_{ij} = \begin{cases} c\Big(1 + a(r_{ij}/R)^2 - b(r_{ij}/R)^4\Big) & \text{when } r_{ij} \leq R, \\ 0 & \text{when } r_{ij} > R, \end{cases} \tag{5.14}$$

in our model. We have chosen a as the free parameter, with $b = 1 + a$ and $c = 4(1+a)/[4(1+a)+a^2]$ for normalization. Thus, at a sufficiently high overall temperature $T = 1/\beta$, the central part simply melts and looses its superfluid properties, as is also indicated by the vanishing of the modified helicity modulus in Figure 5.6.

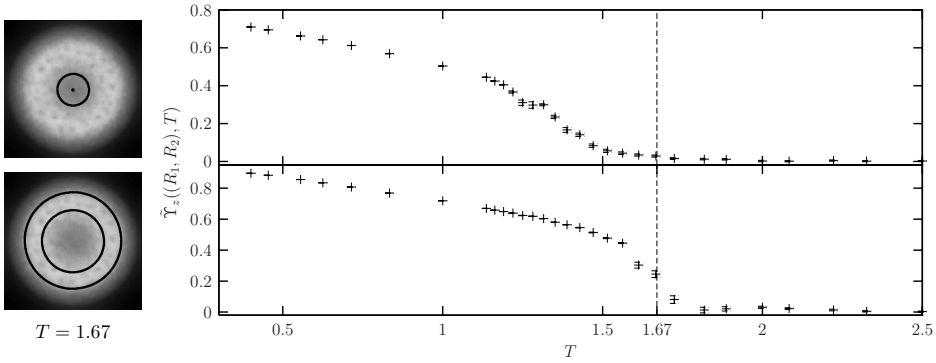

Figure 5.6: Modified helicity modulus $\tilde{\Upsilon}_z$ in a system with a harmonic plus quartic density profile, calculated for the radii indicated by the circles in the leftmost pictures.

Finally, we mention briefly that our model possibly can be applied to the currently very active field of crossover of paired fermion systems from the BCS[1] to the Bose–Einstein regime. Recent work of Schunck and coworkers [106] show remarkably similar structures of the condensate when compared to the renormalized density plots of our simulations with a harmonic trap (Figure 5.7). This

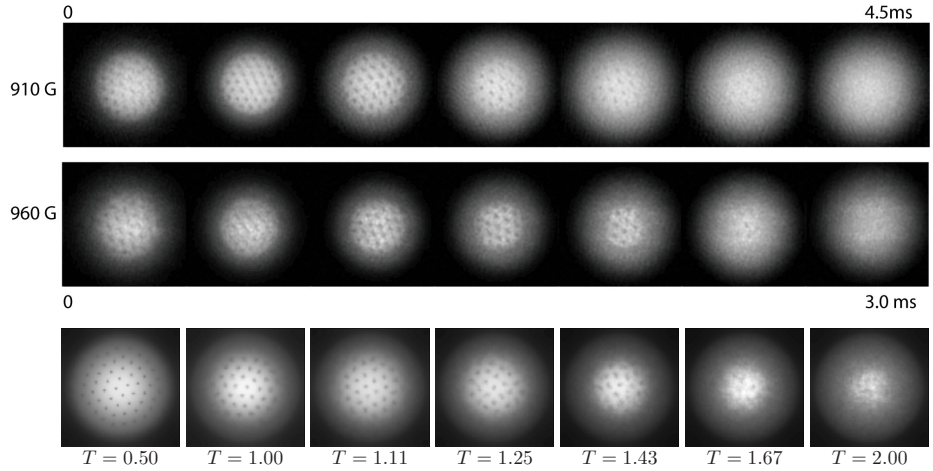

Figure 5.7: Observations of vortices in rotating systems where strongly interacting fermions pair up to form a superfluid according to BCS theory (first and second row), after Schunck and coworkers [106]. In the last row, we demonstrate the renormalized condensate density obtained from simulations with a harmonic a priori density profile.

comparison requires further study. It is not clear whether the outer regions of the experiemental pictures correspond to unpaired fermions, in which case the $3DXY$ model does not apply, or fermions in Cooper pairs effectively above the condensation temperature due to low density. In the latter situation, the similarities in Figure 5.7 may not be incidental.

[1] BCS refers to the Bardeen–Cooper–Schrieffer theory for superconductivity.

Bibliography

[1] S. Kragset, A. Sudbø, and F. S. Nogueira, Phys. Rev. Lett. **92**, 186403 (2004).

[2] K. Børkje, S. Kragset, and A. Sudbø, Phys. Rev. B **71**, 085112 (2005).

[3] S. Kragset, E. Smørgrav, J. Hove, F. S. Nogueira, and A. Sudbø, cond-mat/0609336 , submitted to Phys. Rev. Lett.

[4] S. Kragset, E. Babaev, and A. Sudbø, cond-mat/0604416 , accepted for publication in Phys. Rev. Lett.

[5] A. K. Nguyen, *Phase transitions in extreme type-II superconductors: topological defects, and dual description of the vortex system*, PhD thesis, NTNU, 1999.

[6] S. Mo, *Phase structure and critical properties of an abelian gauge theory*, PhD thesis, NTNU, 2001.

[7] J. Hove, *Critical properties of the Abelian Higgs model*, PhD thesis, NTNU, 2002.

[8] J. Smiseth, *Criticality and novel quantum liquid phases in Ginzburg–Landau theories with compact and non-compact gauge fields*, PhD thesis, NTNU, 2005.

[9] E. Smørgrav, *Critical properties of effective gauge theories for novel quantum fluids*, PhD thesis, NTNU, 2005.

[10] R. K. Pathria, *Statistical Mechanics, Second Edition* (Butterworth-Heinemann, 1996).

[11] P. M. Chaikin and T. C. Lubensky, *Principles of condensed matter physics* (Cambridge University Press, 2000).

[12] N. Goldenfeld, *Lectures on phase transitions and the renormalization group* (Addison-Wesley Publishing Company, 1992).

[13] A. Sudbø, E. Smørgrav, J. Smiseth, F. S. Nogueira, and J. Hove, Phys. Rev. Lett. **89**, 226403 (2002).

[14] J. Smiseth, E. Smørgrav, F. S. Nogueira, J. Hove, and A. Sudbø, Phys. Rev. B **67**, 205104 (2003).

[15] H. E. Stanley, *Introduction to phase transitions an critical phenomena* (Clarendon Press Oxford, 1971).

[16] V. Berezinskii, Sov. Phys. JETP **32**, 493 (1970).

[17] J. M. Kosterlitz and D. J. Thouless, J. Phys. C **6**, 1181 (1973).

[18] D. P. Landau and K. Binder, *A guide to monte carlo simulations in statistical physics* (Cambridge University Press, Cambridge, 2000).

[19] L. D. Landau and E. M. Lifshitz, *Statistical physics, 2nd edition* (Pergamon Press, Oxford, 1969).

[20] V. L. Ginzburg, Sov. Phys. JETP **4**, 153 (1957).

[21] J. B. Kogut, Rev. Mod. Phys. **51**, 659 (1979).

[22] A. K. Nguyen and A. Sudbø, Phys. Rev. B **60**, 15307 (1999).

[23] N. D. Mermin and H. Wagner, Phys. Rev. Lett. **17**, 1307 (1966).

[24] R. Savit, Rev. Mod. Phys. **52**, 453 (1980).

[25] H. Kleinert, *Gauge fields in condensed matter physics, Vol. 1* (World Scientific, Singapore, 1989).

[26] M. B. Einhorn and R. Savit, Phys. Rev. D **17**, 2583 (1978).

[27] J.-R. Lee and S. Teitel, Phys. Rev. B **46**, 3247 (1992).

[28] L. Onsager, Phys. Rev. **65**, 117 (1944).

[29] W. K. Hastings, Biometrika **57**, 97 (1970).

[30] N. Metropolis, A. W. Rosenbluth, M. N. Rosenbluth, A. H. Teller, and E. Teller, J. Chem. Phys. **21**, 1087 (1953).

[31] B. A. Berg and T. Neuhaus, Phys. Rev. Lett. **68**, 9 (1992).

[32] B. A. Berg, Comput. Phys. Commun. **153**, 397 (2003).

[33] J. J. Binney, N. J. Dowrick, A. J. Fisher, and M. E. J. Newman, *The theory of critical phenomena, an introduction to the renormalization group* (Oxford University Press, Oxford, 1992).

[34] A. M. Ferrenberg and R. H. Swendsen, Phys. Rev. Lett. **61**, 2635 (1988).

[35] A. M. Ferrenberg and R. H. Swendsen, Phys. Rev. Lett. **63**, 1195 (1989).

[36] K. Kajantie, L. Kärkkäinen, and K. Rummukainen, Nucl. Phys. B **333**, 100 (1990).

[37] J. Hove, Phys. Rev. E **70**, 056707 (2004).

[38] B. A. Berg, Comput. Phys. Commun. **69**, 7 (1992).

[39] K. G. Wilson, Rev. Mod. Phys. **47**, 773 (1975).

[40] P. W. Anderson, *Basic notions of condensed matter physics* (Benamin/Cummings, 1984).

[41] B. Widom, The Journal of Chemical Physics **43**, 3892 (1965).

[42] M. Campostrini, M. Hasenbusch, A. Pelissetto, P. Rossi, and E. Vicari, Phys. Rev. B **63**, 214503 (2001).

[43] H. Weber and P. Minnhagen, Phys. Rev. B **37**, 5986 (1988).

[44] P. Olsson and P. Holme, Phys. Rev. B **63**, 052407 (2001).

[45] J.-R. Lee and S. Teitel, Phys. Rev. Lett. **64**, 1483 (1990).

[46] J. Lidmar and M. Wallin, Phys. Rev. B **55**, 522 (1997).

[47] P. Minnhagen and B. J. Kim, Physical Review B **67**, 172509 (2003).

[48] M. E. Fisher and A. N. Berker, Phys. Rev. B **26**, 2507 (1982).

[49] J. L. Cardy and P. Nightingale, Phys. Rev. B **27**, 4256 (1983).

[50] J. Lee and J. M. Kosterlitz, Phys. Rev. Lett. **65**, 137 (1990).

[51] J. Lee and J. M. Kosterlitz, Phys. Rev. B **43**, 3265 (1991).

[52] H. Kleinert, F. S. Nogueira, and A. Sudbø, Phys. Rev. Lett. **88**, 232001 (2002).

[53] H. Kleinert, F. S. Nogueira, and A. Sudbø, Nucl. Phys. B **666**, 361 (2003).

[54] J. Bardeen, L. N. Cooper, and J. R. Schrieffer, Phys. Rev. **108**, 1175 (1957).

[55] S. Sachdev, Reviews of Modern Physics **75**, 913 (2003).

[56] J. B. Marston and I. Affleck, Phys. Rev. B **39**, 11538 (1989).

[57] P. A. Lee and N. Nagaosa, Phys. Rev. B **46**, 5621 (1992).

[58] N. Nagaosa and P. A. Lee, Phys. Rev. B **61**, 9166 (2000).

[59] E. Fradkin and S. H. Shenker, Phys. Rev. D **19**, 3682 (1979).

[60] A. M. Polyakov, Nucl. Phys. B **120**, 429 (1977).

[61] M. B. Einhorn and R. Savit, Phys. Rev. D **19**, 1198 (1979).

[62] I. Ichinose and T. Matsui, Phys. Rev. B **51**, 11860 (1995).

[63] I. Ichinose, T. Matsui, and M. Onoda, Phys. Rev. B **64**, 104516 (2001).

[64] I. F. Herbut and B. H. Seradjeh, Physical Review Letters **91**, 171601 (2003).

[65] I. F. Herbut, B. H. Seradjeh, S. Sachdev, and G. Murthy, Physical Review B **68**, 195110 (2003).

[66] M. J. Case, B. H. Seradjeh, and I. F. Herbut, Nucl. Phys. B **676**, 572 (2004).

[67] M. N. Chernodub, E. M. Ilgenfritzc, and A. Schillerd, Phys. Lett. B **547**, 269 (2002).

[68] M. N. Chernodub, E. M. Ilgenfritzc, and A. Schillerd, Phys. Lett. B **555**, 206 (2003).

[69] Y. Saito and H. Müller-Krumbhaar, Phys. Rev. B **23**, 308 (1981).

[70] P. Minnhagen and M. Wallin, Phys. Rev. B **36**, 5620 (1987).

[71] P. Gupta and S. Teitel, Phys. Rev. B **55**, 2756 (1997).

[72] P. Minnhagen, Rev. Mod. Phys. **59**, 1001 (1987).

[73] J. Fröhlich and T. Spencer, J. Stat. Phys. **24**, 617 (1981).

[74] S. Sachdev, Quantum phases and phase transitions of mott insulators, in *Lecture Notes in Physics: Quantum magnetism*, edited by U. Schollwock, J. Richter, D. J. J. Farnell, and R. A. Bishop, Springer, Berlin, 2004.

[75] T. Senthil, L. Balents, S. Sachdev, A. Vishwanathand, and M. P. A. Fisher, **303**, 1490 (2004).

[76] T. Senthil, L. Balents, S. Sachdev, A. Vishwanath, and M. P. A. Fisher, Phys. Rev. B **70**, 144407 (2004).

[77] M. V. Berry, Physics Today **43**, 34 (1990).

[78] F. D. M. Haldane, Phys. Rev. Lett. **61**, 1029 (1988).

[79] E. Dagotto, Rev. Mod. Phys. **66**, 763 (1994).

[80] E. Babaev, Phys. Rev. Lett. **89**, 067001 (2002).

[81] E. Babaev, Nuclear Physics B **686**, 397 (2004).

[82] J. Smiseth, E. Smørgrav, E. Babaev, and A. Sudbø, Phys. Rev. B **71**, 214509 (2005).

[83] E. Babaev, A. Sudbø, and N. W. Ashcroft, Nature **431**, 666 (2004).

[84] O. I. Motrunich and A. Vishwanath, Phys. Rev. B **70**, 075104 (2004).

[85] G. Baym, C. Pethick, and D. Pines, Nature **224**, 673 (1969).

[86] E. J. Yarmchuk, M. J. V. Gordon, and R. E. Packard, Phys. Rev. Lett. **43**, 214 (1979).

[87] A. Houghton, R. A. Pelcovits, and A. Sudbø, Phys. Rev. B **40**, 6763 (1989).

[88] G. Blatter, M. V. Feigel'man, V. B. Geshkenbein, A. I. Larkin, and V. M. Vinokur, Rev. Mod. Phys. **66**, 1125 (1994).

[89] E. Smørgrav, J. Smiseth, E. Babaev, and A. Sudbø, Phys. Rev. Lett. **94**, 096401 (2005).

[90] Y.-H. Li and S. Teitel, Phys. Rev. Lett. **66**, 3301 (1991).

[91] R. E. Hetzel, A. Sudbø, and D. A. Huse, Phys. Rev. Lett. **69**, 518 (1992).

[92] X. Hu, S. Miyashita, and M. Tachiki, Phys. Rev. Lett. **79**, 3498 (1997).

[93] J. R. Abo-Shaeer, C. Raman, J. M. Vogels, and W. Ketterle, Science **292**, 476 (2001).

[94] A. A. Abrikosov, Zh. Eksp. Teor. Fiz. **32**, 1442 (1957).

[95] M. H. Anderson, J. R. Ensher, M. R. Matthews, C. E. Wieman, and E. A. Cornell, Science **269**, 198 (1995).

[96] K. B. Davis *et al.*, Phys. Rev. Lett. **75**, 3969 (1995).

[97] V. Schweikhard, I. Coddington, P. Engels, V. P. Mogendorff, and E. A. Cornell, Physical Review Letters **92**, 040404 (2004).

[98] V. Bretin, S. Stock, Y. Seurin, and J. Dalibard, Physical Review Letters **92**, 050403 (2004).

[99] L. J. Campbell and R. M. Ziff, Phys. Rev. B **20**, 1886 (1979).

[100] C. Pethick and H. Smith, *Bose-Einstein Condensation in Dilute Gases* (Cambridge University Press, 2001).

[101] A. J. Leggett, Rev. Mod. Phys. **73**, 307 (2001).

[102] N. R. Cooper, S. Komineas, and N. Read, Physical Review A **70**, 033604 (2004).

[103] G. Watanabe, G. Baym, and C. J. Pethick, Physical Review Letters **93**, 190401 (2004).

[104] `http://cua.mit.edu/ketterle_group`.

[105] S. Kragset, E. Babaev, and A. Sudbø, unpublished .

[106] C. H. Schunck, M. W. Zwierlein, A. Schirotzek, and W. Ketterle, cond-mat/0607298 (2006).

Paper I

Metal-insulator transition in two- and three-dimensional logarithmic plasmas

Physical Review Letters **92**, 186403 (2004)

Metal-Insulator Transition in Two- and Three-Dimensional Logarithmic Plasmas

S. Kragset,[1,*] A. Sudbø,[1,†] and F. S. Nogueira[2,‡]

[1]*Department of Physics, Norwegian University of Science and Technology, N-7491 Trondheim, Norway*
[2]*Institut für Theoretische Physik, Freie Universität Berlin, Arnimallee 14, D-14195 Berlin, Germany*

(Received 23 November 2003; published 5 May 2004)

We consider the scaling of the mean square dipole moment in a plasma with logarithmic interactions in a two- and three-dimensional systems. In both cases, we establish the existence of a low-temperature regime where the mean square dipole moment does not scale with system size and a high-temperature regime where it does scale with system size. Thus, there is a nonanalytic change in the polarizability of the system as a function of temperature and hence a metal-insulator transition in both cases. The relevance of this transition in three dimensions to quantum phase transitions in $(2 + 1)$-dimensional systems is briefly discussed.

DOI: 10.1103/PhysRevLett.92.186403 PACS numbers: 71.30.+h, 52.65.Pp, 64.60.Cn

Gauge theories where matter fields are coupled to compact gauge fields in $2 + 1$ dimensions have recently been much studied as effective theories for Mott insulators with competing orders [1–3]. Compact $U(1)$ gauge theories in $2 + 1$ dimensions are capable of sustaining topological defects in the gauge fields in the form of space-time instantons [4]. Such theories generically offer the possibility of featuring confinement-deconfinement transitions associated with a proliferation of topological defects in the gauge sector. It is hoped that phase transitions in matter coupled such theories [5,6] may be connected to difficult problems in condensed matter physics, such as the breakdown of Landau Fermi liquid theory and possibly also spin-charge separation in strongly correlated systems at zero temperature in two spatial dimensions [7]. One such model considered recently is the compact Abelian Higgs model where the gauge field is coupled to matter fields with the *fundamental charge* [8]. By itself, the compact $U(1)$ gauge sector may be mapped onto the $(2 + 1)$-dimensional Coulomb gas with $1/R$ interactions between "point charges," i.e., the instantonic topological defects of the theory [4]. As shown by Polyakov, the latter system is always in a metallic phase (when the instantons are regarded as electric charges) [4]. More recently, it was shown that when matter carrying the fundamental charge was coupled to the compact gauge sector, and critical matter field fluctuations were integrated out, the system could be mapped onto a gas of point charges interacting with a potential $-\ln(R)$ in $2 + 1$ space-time dimensions, instead of $1/R$ [8]. Using renormalization group (RG) arguments, it was demonstrated that the system with the $(2 + 1)$-dimensional logarithmic interaction may undergo a finite-temperature phase transition driven by the unbinding of dipole configurations [8], from a low-temperature dielectric regime to a high-temperature metallic regime (again when the instantons are regarded as electric charges). Here, we demonstrate this using Monte Carlo (MC) simulations.

Whether or not there exists a low-temperature dielectric regime separated from a high-temperature metallic regime in a three-dimensional system of point charges interacting with logarithmic interactions and overall charge neutrality is presently a matter of debate in both the condensed matter and lattice gauge theory literature [8–10]. The theorem that dipoles cannot screen the Coulomb potential (in any dimension) [11] does not apply to the case of a logarithmic pair potential between point charges in three dimensions. It is due to this inability of the dipoles to screen a Coulomb potential that the Kosterlitz-Thouless (KT) transition is possible: the low-temperature dielectric phase is always critical below the KT-transition temperature. In three dimensions, on the other hand, Debye-Hückel theory is essentially exact. Thus, starting from a system of charges, screening is such that the screening length cannot become infinite, and the system is always in the metallic phase. On the other hand, if one starts from a three-dimensional dipole system, the system always stays in the dielectric phase, since dipoles cannot screen. Once more, there is no phase transition. If some departure from the Coulomb potential occurs in three dimensions, dipoles could conceivably be able to screen. A 3D logarithmic interaction could, in principle, be screened to a potential that decays with separation between the charges [9]. If so, no metal-insulator transition occurs at any finite temperature, analogous to the situation in a three-dimensional Coulomb plasma [4]. If one thinks of the gas of point charges as a gas of instantonic defects in a compact gauge field, the lack of a metal-insulator transition due to nonstandard screening by dipoles would correspond to permanent confinement in the compact gauge theory.

We therefore consider a logarithmic plasma in two and three dimensions on the lattice using MC simulations and study the polarizability of the system as a function of temperature. The screening properties of these systems determine whether they are insulators or metals and are governed by the dielectric constant ε, which in a low-density approximation is given by the polarizability p of the system, $\varepsilon = 1 + n_d \Omega_d p$. Here n_d is the dipole density, and Ω_d is the solid angle in a d-dimensional system.

Since the polarizability of the system is proportional to the mean square separation $\langle s^2\rangle \equiv \langle|\vec{r}_i - \vec{r}_j|^2\rangle$ between the charges constituting the dipoles, it is natural to focus on $\langle s^2\rangle$ in order to investigate whether the system is a dielectric or a metal. We find a low-temperature regime where dipoles are tightly bound, separated from a high-temperature regime where they are unbound. This implies the existence of a low-temperature insulating regime and a high-temperature metallic regime, separated by a genuine phase transition. For comparison and benchmark purposes, we compute the same quantities for the two-dimensional logarithmic plasma, where a metal-insulator transition in the form of a KT phase transition is known to exist [12,13].

We consider the Hamiltonian

$$\mathcal{H} = \frac{1}{2}\sum_{i,j} q_i V(\vec{r}_i - \vec{r}_j) q_j, \tag{1}$$

with

$$V(\vec{r}) = \frac{4\pi^2}{Na^d}\sum_{\vec{k}} \frac{[e^{i\vec{k}\cdot\vec{r}} - 1]}{[2(d - \sum_{\alpha=1}^{d}\cos k_\alpha a)]^{d/2}}, \tag{2}$$

where the sum is over all pairs of sites of a two- or three-dimensional periodic lattice and q_i is the charge at site i, $N = L^d$ is the total number of sites, and a is the lattice spacing. We have subtracted $V(\vec{r} = 0)$ from the potential, since only neutral configurations contribute to the partition function, and we work at zero chemical potential for the instantons [14]. This has the usual Coulomb form for $d = 2$ but differs from it in the $d = 3$ case: instead of the usual $1/R$ potential of the three-dimensional Coulomb gas (3DCG), the power $3/2$ results in a logarithmic potential. Taking the continuum limit of Eq. (2) for $d = 3$, we find

$$\begin{aligned} V(\vec{r}) &= \int \frac{d^3k}{(2\pi)^3}\frac{[e^{i\vec{k}\cdot\vec{r}} - 1]}{(k^2 + m^2)^{3/2}} \\ &= \frac{1}{2\pi^2}\left[K_0(mr) + \frac{\Lambda}{\sqrt{\Lambda^2 + m^2}} - \operatorname{arcsinh}\left(\frac{\Lambda}{m}\right)\right], \end{aligned} \tag{3}$$

where $K_0(x)$ is a Bessel function, $\Lambda = 2\pi/a$, and the Debye-Hückel screening length m^{-1} was introduced as an infrared regulator. As $m \to 0$ we have

$$V(r) = \frac{1}{2\pi^2}[1 - \gamma - \ln(\Lambda r)] + \mathcal{O}\left(\frac{m}{\Lambda}\right)^2, \tag{4}$$

where γ is the Euler constant. Therefore, Eq. (2) behaves exactly in the same way as the two-dimensional potential.

Let us first turn to the 2DCG which we use as a benchmark on our method of probing the metal-insulator transition, before proceeding to the three-dimensional logarithmic gas (3DLG). At low temperatures this model consists of tightly bound dipoles with the two opposite charges separated by a distance $|\vec{r}_i - \vec{r}_j| \equiv s$ of the order of the lattice constant.

In a 2D system, it is well-known that dipoles begin to unbind at a critical temperature T_{KT} [13] and at high temperatures the 2DCG is a fully ionized metallic plasma, separated from the low-temperature dielectric insulating phase by a genuine KT phase transition. Thus, we expect no finite-size scaling of $\langle s^2\rangle$ below the KT transition, whereas we should expect $\langle s^2\rangle \propto L^{\alpha(T)}$ with $\alpha(T) \leq 2$ at higher temperatures. Using an intuitive low-density argument, neglecting screening effects [13], we can calculate the behavior of $\langle s^2\rangle$ to leading order in L,

$$\langle s^2\rangle \propto \begin{cases} \text{const}; & T < T_{\mathrm{KT}}, \\ L^{(T-T_{\mathrm{KT}})/T}; & T_{\mathrm{KT}} < T < 2T_{\mathrm{KT}}, \\ L^2; & 2T_{\mathrm{KT}} < T. \end{cases} \tag{5}$$

Hence, $\alpha(T)$ is zero for low temperatures and a monotonically increasing function of temperature just above T_{KT}.

Including screening effects in 2D shows that this conclusion still holds; however, the temperature at which it occurs is determined by screening. This is ultimately related to the fact that dipoles contribute only through a correction to the coefficient of the bare logarithmic pair potential. Hence, in 2D the functional form of the renormalized potential is unaltered; only prefactors are changed. In three dimensions, it is far from obvious that dipoles do not have a much more disruptive effect on a bare logarithmic pair potential.

To address the issue of scaling of $\langle s^2\rangle$, we use MC simulations and finite-size scaling to study $\langle s^2\rangle$ both in the 2DCG as well as in the 3DLG. In our simulations, the particle number is not conserved. However, during the simulations the system is maintained electrically neutral. The MC moves involve creation and annihilation of charges, applying the Metropolis algorithm in this process. Starting at some randomly chosen lattice site, an attempt to insert a negative or positive charge at random at this site is made, with an opposite charge at a nearest-neighbor site. The move is accepted with probability $\exp(-\Delta E/T) = \exp[-(\mathcal{H}_{\mathrm{new}} - \mathcal{H}_{\mathrm{old}})/T]$, and this is done in all d directions, before we move to the next site. It is clear that placing a charge on top of an opposite one corresponds to the annihilation of the existing one. In order to measure s we have to keep track of which two charges belong to each other in a dipole, since there is no physical link defining the dipole. Two charges inserted into the lattice at the same MC move is chosen as a dipole, and if one of these charges subsequently is annihilated, the effect of this annihilation is to diffuse one of the charges in the dipole. Hence, such a diffusion may increase or decrease s for this dipole [15]. One sweep is defined as going through all the sites in the lattice once, and at every tenth sweep we sample s^2 averaged over the system. The sample is, however, rejected if there are no charges in the system at this MC time, since there is no information on $\langle s^2\rangle$ in such a configuration. The thermal

average obtained at the end of the simulation is thus taken only over nonempty configurations.

The results from the simulations on the 2DCG are presented in Fig. 1. A total of 10^5 MC sweeps at each temperature are used to produce the first plot. From the $\langle s^2 \rangle$ data of system sizes $L = 8, 12, 16, 20, 24, 28, 32, 36, 40$, and 48, we extract α for temperatures in the interval (1.0, 1.52), which is shown in the second plot. It is evident that there are two distinct regimes of temperatures, one in which the charges of almost all dipoles are bound as tightly as possible; the separation of the charges correspond to the lattice constant. In the high-temperature regime the dipoles have started to separate, reflected by a scaling of $\langle s^2 \rangle \sim L^{\alpha(T)}$ with the system size. The two regimes are necessarily separated by a phase transition, since in the low-temperature regime $\alpha(T) = 0$ while in the high-temperature regime $\alpha(T) \neq 0$. This necessarily implies a nonanalytic behavior of $\alpha(T)$. An attempt to determine the transition temperature from these plots yields approximately 1.32. This is slightly less than the early results of Saito and Müller-Krumbhaar of 1.35 in our units [16] but is in excellent agreement with much more recent simulations by Olsson [17]. It provides confidence in the method of locating the critical point by monitoring the quantity $\langle s^2 \rangle$, even when the system is subjected to periodic boundary conditions [15].

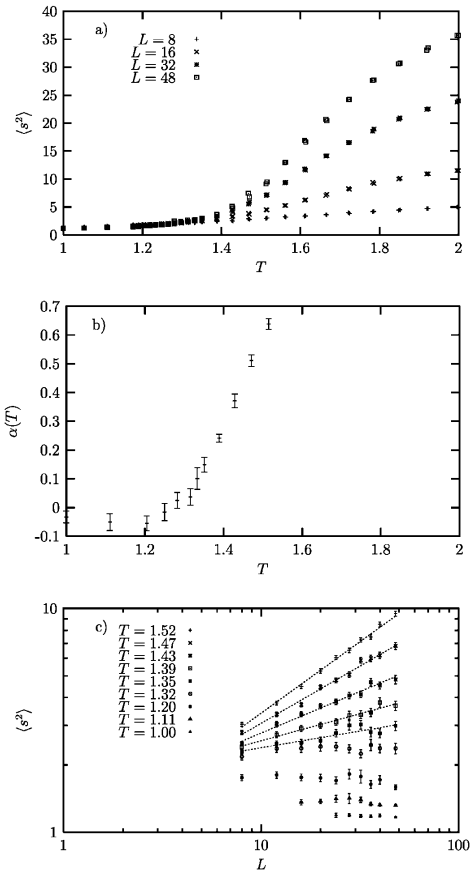

FIG. 1. Results from MC simulations of the 2DCG, where 1.0×10^5 sweeps were used at each temperature. (a) $\langle s^2 \rangle$ versus T for a selection of the simulated system sizes $L = 8, 12, 16, 20, 24, 28, 32, 36, 40$, and 48. Error bars are smaller than the symbols used. (b) α versus T found from fitting the data of $\langle s^2 \rangle$ at different T to AL^{α}, where A is a constant. A selection of such fits are shown in (c). We note that $\langle s^2 \rangle$ is practically independent of L up to a certain T.

Exactly the same simulation technique is applied to the 3DLG, and the results are shown in Fig. 2. The finite-size analysis of $\langle s^2 \rangle$ in order to extract α is here done on the basis of system sizes $L = 8, 12, 16, 20, 24, 28, 32, 36$, and 40 and up to 2.0×10^5 MC sweeps are used. As in the 2DCG we see that the system exhibits two distinct regimes, one insulating regime consisting of tightly bound dipoles and one metallic. There is no scaling of $\langle s^2 \rangle$ with L below $T \simeq 0.32$ with the system size. Note that the change in scaling of the mean square dipole moment occurs at a significantly lower temperature than in the 2DCG. This is to be expected, since there is more configurational entropy available in 3D than in 2D. It is worthwhile comparing this result with the one obtained in Ref. [8] where the coupling $4\pi^2/t$ corresponds to the temperature T here. There the critical value $t_c = 12\pi^2$ was obtained, corresponding to $T_c = 1/3$ in our case and agreeing well with our numerical result.

The main result is that in the 3DLG and in the 2DCG, a low-temperature regime exists where positive and negative charges are bound in tight dipole pairs. This regime is separated from a high-temperature regime where at least a finite fraction of charges are free. The results obtained in three dimensions have the same features as those found in 2D. The scaling exponent $\alpha(T)$ for $\langle s^2 \rangle$ is zero in the low-temperature phase and positive in the high-temperature phase. Such a change in $\alpha(T)$ cannot be analytical, and therefore the two scaling regimes must be separated from each other via a phase transition. Since $\langle s^2 \rangle$ is a measure of the polarizability of the system, we conclude that the above demonstrates a nonanalytic change in the polarizability of the system, i.e., a nonanalytic change in the dielectric function of the system as a function of temperature. Hence, a system of point charges with overall charge neutrality interacting with a bare logarithmic interaction undergoes a metal-insulator transition in both 2D and 3D.

The 3DLG can be shown to be equivalent to an anomalous sine-Gordon theory in $d = 3$ where the usual k^2 dispersion is replaced by a $|k|^3$ one [8], which is nonanalytic. This leads to technical difficulties in a standard RG calculation, where in a perturbative treatment only *analytic* singularities are generated. Therefore, in a standard RG analysis an analytic correction $\sim k^2$ to the

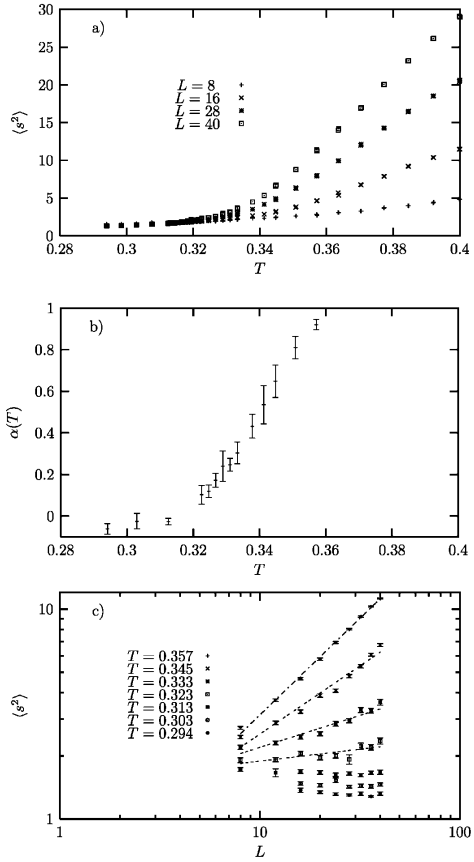

FIG. 2. Results from simulations of the 3DLG. Up to 2.0×10^5 MC sweeps were used at each temperature. (a) $\langle s^2 \rangle$ vs T for some of the simulated system sizes $L = 8$, 12, 16, 20, 24, 28, 32, 36, and 40. Error bars are smaller than the symbols used. (b) $\alpha(T)$ vs T found from fitting the data of $\langle s^2 \rangle$ at different T to AL^{α}, where A is a constant. A selection of such fits are shown in (c). It is evident that a low-temperature regime where $\langle s^2 \rangle$ is independent of L exists in the 3D log gas in the same way that it exists in the 2D log gas.

dispersion can be generated. On the other hand, since $|k|^3$ is nonanalytic, it cannot be renormalized within a standard RG analysis. It is conceivable that this is one of the reasons why a recent RG analysis of this theory did not find evidence for a dielectric phase [9].

We emphasize that although it is known that a metal-insulator transition occurs in 2D via a KT transition [13], our numerics by themselves do not demonstrate this. To establish the KT nature of the transition on purely numerical grounds requires convincing numerical evidence that there is a universal jump in the inverse dielectric constant at the transition. The main point of the present simulations is that they settle the difficult question of whether a low-temperature dielectric regime exists at all in a 3DLG, which is a system not subject to standard electrostatics, and for which the usual theorems on screening of charges by dipoles do not apply. The answer is in the affirmative, and we have applied our method also to the 2D case for comparison and as a benchmark on the correctness of method of monitoring $\langle s^2 \rangle$ to establish the existence of two scaling regimes separated by a phase transition.

The authors acknowledge stimulating discussions and correspondence with I. F. Herbut and S. Sachdev. This work received financial support from the Norwegian University of Science and Technology through the Norwegian High Performance Computing Program (NOTUR), from the Research Council of Norway, Grants No. 158518/431, No. 158547/431 (NANOMAT), and No. 157798/432 (A. S), and from DFG Priority Program SPP 1116 (F. S. N.). One of us (S. K.) thanks the Norwegian University of Science and Technology for support.

*Electronic address: steinar.kragset@phys.ntnu.no
†Electronic address: asle.sudbo@phys.ntnu.no
‡Electronic address: nogueira@physik.fu-berlin.de

[1] S. Sachdev and K. Park, Ann. Phys. (N.Y.) **298**, 58 (2002); S. Sachdev, Rev. Mod. Phys. **75**, 913 (2003).
[2] R. Moessner, S. L. Sondhi, and E. Fradkin, Phys. Rev. B **65**, 024504 (2002).
[3] T. Senthil, A. Vishwanath, L. Balents, S. Sachdev, and M. P. A. Fisher, Science **303**, 1490 (2004).
[4] A. M. Polyakov, Nucl. Phys. **B120**, 429 (1977).
[5] E. Fradkin and S. H. Shenker, Phys. Rev. D **19**, 3682 (1979); see also N. Nagaosa and P. A. Lee, Phys. Rev. B **61**, 9166 (2000).
[6] M. Einhorn and R. Savit, Phys. Rev. D **19**, 1198 (1979).
[7] T. Senthil and M. P. A. Fisher, Phys. Rev. B **62**, 7850 (2000).
[8] H. Kleinert, F. S. Nogueira, and A. Sudbø, Phys. Rev. Lett. **88**, 232001 (2002); Nucl. Phys. **B666**, 361 (2003).
[9] I. F. Herbut and B. H. Seradjeh, Phys. Rev. Lett. **91**, 171601 (2003); I. F. Herbut, B. H. Seradjeh, S. Sachdev, and G. Murthy, Phys. Rev. B **68**, 195110 (2003); M. J. Case, B. H. Seradjeh, and I. F. Herbut, Nucl. Phys. **B676**, 572 (2004).
[10] M. N. Chernodub, E.-M. Ilgenfritz, and A. Schiller, Phys. Lett. B **547**, 269 (2002); **555**, 206 (2003).
[11] J. Fröhlich and T. Spencer, J. Stat. Phys. **24**, 617 (1981).
[12] P. Minnhagen, Rev. Mod. Phys. **59**, 1001 (1987).
[13] J. M. Kosterlitz and D. J. Thouless, J. Phys. C **6**, 1181 (1973).
[14] See Eqs. (8) and (10) in J.-R. Lee and S. Teitel, Phys. Rev. B **46**, 3247 (1992).
[15] Periodic boundary conditions are enforced by decomposing the dipole vectors in Cartesian components s_α, $\alpha \in (x, y, z)$ and letting $s_\alpha \to L - s_\alpha$ if $s_\alpha > L/2$.
[16] Y. Saito and H. Müller-Krumbhaar, Phys. Rev. B **23**, 308 (1980).
[17] P. Olsson (private communication).

Paper II

Instanton correlators and phase transitions in two- and three-dimensional logarithmic plasmas

Physical Review B **71**, 085112 (2005)

Instanton correlators and phase transitions in two- and three-dimensional logarithmic plasmas

K. Børkje,[1,*] S. Kragset,[1,†] and A. Sudbø[1,‡]
[1]*Department of Physics, Norwegian University of Science and Technology, N-7491 Trondheim, Norway*
(Received 22 June 2004; published 14 February 2005)

The existence of a discontinuity in the inverse dielectric constant of the two-dimensional (2D) Coulomb gas is demonstrated on purely numerical grounds. This is done by expanding the free energy in an applied twist and performing a finite-size scaling analysis of the coefficients of higher-order terms. The phase transition, driven by unbinding of dipoles, corresponds to the Kosterlitz-Thouless transition in the 2D *XY* model. The method developed is also used for investigating the possibility of a Kosterlitz-Thouless phase transition in a three-dimensional system of point charges interacting with a logarithmic pair-potential, a system related to effective theories of low-dimensional strongly correlated systems. We also contrast the finite-size scaling of the fluctuations of the dipole moments of the two-dimensional Coulomb gas and the three-dimensional logarithmic system to those of the three-dimensional Coulomb gas.

DOI: 10.1103/PhysRevB.71.085112 PACS number(s): 04.50.+h, 11.25.−w, 98.80.−k

I. INTRODUCTION

Compact $U(1)$ gauge fields in three dimensions are of great interest in condensed matter theory, as they arise in effective theories of strongly correlated two-dimensional (2D) systems at zero temperature.[1–4] Lightly doped Mott-Hubbard insulators, such as high-T_c cuprates, are examples of systems possibly described by such theories, where the compact gauge field emerges from strong local constraints on the electron dynamics.[2,5–7] High-T_c cuprates appear to fall outside the Landau-Fermi-liquid paradigm, and a so-called confinement-deconfinement transition in the gauge theories may be associated with breakdown of Fermi liquid and quasiparticles in 2D at $T=0$.[6–8] Obliteration of electronlike quasiparticles and spin-charge separation in the presence of interactions is well known to occur in one spatial dimension. However, the mechanism operative in that case, namely singular forward scattering, is unlikely to be operative in higher dimensions due to the much less restrictive kinematics at the Fermi surface.[9] Proliferation of instantons of emergent gauge fields show more promise as a viable candidate mechanism. This line of pursuit has recently been reinvigorated in the context of understanding the physics of lightly doped Mott-Hubbard insulators and unconventional insulating states.[10]

The compact nature of a constraining gauge field on a lattice model introduces topological defects defined by surfaces where the field jumps by 2π, forming a gas of instantons (or "monopoles") in $2+1$ dimensions.[11] Considering the gauge sector only, the interactions between these instantonic defects are the same as between charges in a 3D Coulomb gas, i.e., $1/r$-interactions. Such a gas is always in a metallic or plasma phase with a finite screening length,[11,12] and there is no phase transition between a metallic regime and an insulating regime. However, in models where compact gauge fields are coupled to *matter fields*, the interaction between the magnetic monopoles may be modified by the emergence of an anomalous scaling dimension of the gauge field due to critical matter-field fluctuations.[13] This is the case for the compact abelian Higgs model with matter fields in the fundamental representation.[14]

In Refs. 14, it was shown that the introduction of a matter field with the fundamental charge leads to an anomalous scaling dimension in the gauge field propagator.[13] The effect is to alter the interaction potential between the magnetic monopoles from $1/r$ to $-\ln r$. The existence of a confinement-deconfinement transition in the gauge theory is thus related to whether a phase transition occurs in a 3D gas of point charges with logarithmic interactions. However, one should note that the legitimacy of a monopole action based on just pairwise interactions has been questioned, particularly when viewed as an effective description of an effective gauge theory of strongly interacting systems.[15] The 3D logarithmic plasma is however of considerable interest in its own right.

In two dimensions, where $-\ln r$ is the Coulomb potential, it is known that the logarithmic gas experiences a phase transition from a low-temperature insulating phase consisting of dipoles to a high-temperature metallic phase. This is nothing but the Coulomb-gas representation of the Kosterlitz-Thouless transition in the 2D *XY* model. In a 3D logarithmic gas, the existence of a phase transition is still subject to debate.[14,16,17] Renormalization group arguments have been used[14] to demonstrate that a transition may occur, driven by the unbinding of dipoles. Others have claimed that the 3D logarithmic gas is always in the metallic phase.[16] In a recent paper,[18] large scale Monte Carlo simulations indicated that two distinct phases of the 3D-log gas exists; a low-T regime where the dipole moment does not scale with system size and a high-T regime where the dipole moment is system size dependent. Those results do not, however, determine the character of the phase transitions. That will be the main subject of this paper.

The Kosterlitz-Thouless transition in the 2D *XY* model is characterized by the universal jump to zero of the helicity modulus.[19] In the corresponding 2D Coulomb gas, it is the inverse of the macroscopic dielectric constant ϵ that experiences a jump to zero when going from the insulating to the metallic phase. According to Ref. 14, such a universal discontinuity should also take place for ϵ^{-1} in the 3D logarithmic gas associated with the confinement-deconfinement transition. Proving that such discontinuities exist numerically is a

subtle task. The discontinuous character of the helicity modulus in the 2D *XY* model is very hard to see in a convincing manner by computing the helicity modulus, due to severe finite-size effects. It was only recently proven on purely numerical grounds that such a discontinuity exists[20] in a simple, but yet clever manner. By imposing a twist across the system and expanding the free energy in this twist to the fourth order, a stability argument was used to show that the second order term in the expansion, the helicity modulus, must be nonzero at T_c. The proof relies on the ability to conclude that the fourth order term is negative in the thermodynamic limit, from which the discontinuity follows immediately. In this paper, we will repeat this procedure, but now in the language of the 2D Coulomb gas. In addition to confirming the results of Minnhagen and Kim, the method which we develop here could be suitable for proving the possibly discontinuous behavior of ϵ^{-1} in the 3D logarithmic gas. This is a main motivation for translating the procedure of Ref. 20 to the vortex language, since the 3D logarithmic gas is not the dual theory of any simple spin model. After having demonstrated the discontinuity in the 2D Coulomb gas, we go on to apply the method on the 3D logarithmic gas. We also compare the scaling with system size of the mean square dipole moment for these logarithmic plasmas, and contrast the results with those of the 3D Coulomb gas. This is important, since the mean square dipole moment does not scale with system size below a certain temperature for the logarithmic plasmas.[18] This indicates that two phases exist, where the low-temperature regime consists of tightly bound pairs. However, the results for the 3D Coulomb gas are qualitatively different, in accordance with the fact that such a low-temperature phase is absent in that case.

II. MODEL

The Hamiltonian of the 2D *XY* model on a square lattice modified with a twist $\mathbf{T}(x,y)$ is

$$H_{XY} = -J\sum_{\langle i,j\rangle} \cos(\theta_i - \theta_j - 2\pi \mathbf{r}_{ij}\cdot\mathbf{T}), \tag{1}$$

where $\mathbf{r}_{ij}$ is the displacement between the nearest neighbor pairs to be summed over. We set the coupling constant J to unity. The volume of the system, i.e., the number of lattice points, is L^2, and the angle θ_i is subject to periodic boundary conditions. In the Villain approximation, a duality transformation leads to the Hamiltonian

$$H = \frac{1}{2}\sum_{i,j} (m + \varepsilon^{\mu\nu}\Delta^\mu T^\nu)_i V_{ij} (m + \varepsilon^{\rho\sigma}\Delta^\rho T^\sigma)_j, \tag{2}$$

where m_i are point charges on the dual lattice, corresponding to vortex excitations in the *XY* model. Δ^μ is a lattice derivative and $\varepsilon^{\mu\nu}$ is the completely antisymmetric symbol. The potential V_{ij} is given by

$$V(|\mathbf{r}_i - \mathbf{r}_j|) = \frac{2\pi^2}{L^2}\sum_{\mathbf{q}} \frac{e^{-i\mathbf{q}\cdot(\mathbf{r}_i - \mathbf{r}_j)}}{2 - \cos q_x - \cos q_y}, \tag{3}$$

which has a logarithmic long-range behavior. Details of the dualization are found in Appendix A. As is well known, Eq. (2) at zero twist describes the two-dimensional Coulomb gas (2D CG). In this representation, the Kosterlitz-Thouless phase transition of the 2D *XY* model is recognized by a discontinuous jump to zero of the inverse macroscopic dielectric constant ϵ^{-1} at T_c. We note that the curl of the twist $\mathbf{T}$ acts as a modification of the charge field in the 2D CG.

The free energy of the system is $F=-T\ln Z$, where the partition function is given by summing the Boltzmann factor over all charge configurations

$$Z = \sum_{\{m\}} e^{-H/T}. \tag{4}$$

Let us write the Hamiltonian in Fourier representation

$$H = \frac{1}{2L^2}\sum_{\mathbf{q}} (m_{\mathbf{q}} + \varepsilon^{\nu\lambda} Q^\nu_{-\mathbf{q}} T^\lambda_{\mathbf{q}}) V_{\mathbf{q}} (m_{-\mathbf{q}} + \varepsilon^{\rho\sigma} Q^\rho_{\mathbf{q}} T^\sigma_{-\mathbf{q}}), \tag{5}$$

where the discrete Fourier transform is defined as in Appendix B and $\Delta^\mu e^{\pm i\mathbf{q}\cdot\mathbf{r}} \equiv e^{\pm i\mathbf{q}\cdot\mathbf{r}} Q^\mu_{\pm\mathbf{q}}$.

III. STABILITY ARGUMENT

From Eq. (1), it is clear that $F(\mathbf{T}) \geqslant F(0)$ in the low-temperature phase, i.e., the free energy is minimal for zero twist. This inequality is also valid at the critical temperature T_c, since the free energy must be a continuous function of temperature. As a consequence, the Taylor expansion

$$F(\mathbf{T}) - F(0) = \sum_\alpha \sum_{\mathbf{q}_1} \left.\frac{\partial F}{\partial T^\alpha_{\mathbf{q}_1}}\right|_{\mathbf{T}=0} T^\alpha_{\mathbf{q}_1} + \sum_{\alpha,\beta}\sum_{\mathbf{q}_1\mathbf{q}_2} \left.\frac{\partial^2 F}{\partial T^\alpha_{\mathbf{q}_1}\partial T^\beta_{\mathbf{q}_2}}\right|_{\mathbf{T}=0} \frac{T^\alpha_{\mathbf{q}_1} T^\beta_{\mathbf{q}_2}}{2} + \cdots \tag{6}$$

cannot be negative for any $T \leqslant T_c$. Expressions for the derivatives of the free energy with respect to a general twist are found in Appendix B. Only terms of even order will contribute to the series, since m_i may take equally many positive and negative values. We are free to *choose* the twist to be

$$\mathbf{T}(x,y) = \frac{\Delta}{L^\eta}\sin\left(\frac{2\pi y}{L}\right)\hat{\mathbf{x}}, \tag{7}$$

where Δ is an arbitrarily small constant and $\eta=1$ for the two-dimensional Coulomb gas. To the fourth order, this long-wavelength twist turns Eq. (6) into

$$F(\mathbf{T}) - F(0) = \frac{\Delta^2}{4} C_{\mathbf{k}} \left(1 - \frac{V_{\mathbf{k}}}{L^2 T}\langle m_{\mathbf{k}} m_{-\mathbf{k}}\rangle\right) + \frac{\Delta^4}{32}\frac{(C_{\mathbf{k}} V_{\mathbf{k}})^2}{L^4 T^3}\left(\langle m_{\mathbf{k}} m_{-\mathbf{k}}\rangle^2 - \frac{1}{2}\langle (m_{\mathbf{k}} m_{-\mathbf{k}})^2\rangle\right), \tag{8}$$

where $\mathbf{k}=(0,2\pi/L)$ and $C_{\mathbf{k}} = Q^y_{\mathbf{k}} Q^y_{-\mathbf{k}} V_{\mathbf{k}}$. We recognize the paranthesis in the second order term as the dielectric response function $\epsilon^{-1}(\mathbf{k})$, where $\mathbf{k}$ is now the smallest nonzero wave vector in a finite system. Note that the prefactors in both terms are independent of system size as $L\to\infty$. The crucial argument to use is the same as in Ref. 20. If the

fourth order term approaches a finite negative value at T_c in the limit $L\to\infty$, the second order term, $\epsilon^{-1}(\mathbf{k}\to 0)$, must be positive to satisfy the inequality $F(\mathbf{T})\geqslant F(0)$. Furthermore, since we know that the inverse dielectric constant is zero in the high-temperature phase, it necessarily experiences a discontinuity at T_c. As we shall see, Monte Carlo simulations show that the fourth order term is indeed negative at T_c in the thermodynamic limit.

The argument described above will also apply to a three-dimensional gas of point charges interacting via a pair potential of some sort, as long as the twist raises the free energy in the low-temperature regime. Since the curl of the twist $\mathbf{T}$ is a vector in that case, one may for instance choose the z component of this vector as the perturbing charge in Eq. (2). The two three-dimensional systems we will consider are the logarithmic gas and the Coulomb gas. The expansion (6) is valid for any system size L. However, to make the change in free energy nondivergent as $L\to\infty$, the twist must be chosen such that the terms in the expansion are independent of system size. This is obtained by choosing $\eta=2$ for the logarithmic gas and $\eta=3/2$ for the Coulomb gas. η is defined in Eq. (7). In both cases, the second order term will be proportional to

$$\epsilon^{-1}(\mathbf{k}) = 1 - \frac{V_{\mathbf{k}}}{L^3 T}\langle m_{\mathbf{k}} m_{-\mathbf{k}}\rangle. \tag{9}$$

The fourth order term will be proportional to

$$\epsilon_4(\mathbf{k}) \equiv \frac{1}{T^3}\left(\langle m_{\mathbf{k}} m_{-\mathbf{k}}\rangle^2 - \frac{1}{2}\langle (m_{\mathbf{k}} m_{-\mathbf{k}})^2\rangle\right) \tag{10}$$

in the logarithmic case. In the case of a 3D Coulomb gas, the interesting quantity will be ϵ_4/L^2, which is independent of system size since $\langle m_{\mathbf{k}} m_{-\mathbf{k}}\rangle \sim L$ in that case.

IV. SIMULATION RESULTS

Standard Metropolis Monte Carlo simulations are carried out on the model (2) at zero twist. An $L\times L$ square lattice with periodic boundary conditions is used and the system is kept electrically neutral at all times during the simulations. This is achieved by inserting dipoles with probability according to the Metropolis algorithm: An insertion of a negative or positive charge is attempted at random at a given lattice site, and an opposite charge is placed at one of the nearest-neighbor sites to make the dipole. This is one move, accepted with probability $\exp(-\Delta E/T)=\exp[-(\mathcal{H}_{\text{new}}-\mathcal{H}_{\text{old}})/T]$, and the sequence of trying this for all sites in the system once is defined as one sweep. If a charge is placed on top of an opposite one, the effect is to annihilate the existing one. All simulations are performed going from high to low temperature and after simulating one system size L the sampled data are postprocessed using Ferrenberg-Swendsen reweighting techniques.[21]

A. 2D Coulomb gas

We consider first the 2D Coulomb gas, which is known to suffer a metal-insulator transition via a Kosterlitz-Thouless phase transition. In this case, Monte Carlo data are obtained for $L=4-100$ and for each L up to 200 000 sweeps at each temperature is used.

We start by taking the Hamiltonian (2) and computing the mean square of the dipole moment $\langle s^2\rangle$ as a function of system size and temperature. A mean square dipole moment which is independent of system size indicates the existence of tightly bound dipoles and a dielectric or insulating phase. If the mean square dipole moment scales with system size, this demonstrates the existence of free unbound charges and hence a metallic phase. In other words, we expect in the low-temperature dielectric insulating phase no finite-size scaling of $\langle s^2\rangle$, whereas we should expect $\langle s^2\rangle \propto L^{\alpha(T)}$ with $\alpha(T)\leqslant 2$ at higher temperatures. Using an intuitive low density argument, neglecting screening effects,[22] we can calculate the behavior of $\langle s^2\rangle$ to leading order in L,

$$\langle s^2\rangle \propto \begin{cases} \text{const.}, & T < T_{\text{KT}}, \\ L^{(T-T_{\text{KT}})/T}, & T_{\text{KT}} < T < 2T_{\text{KT}}, \\ L^2, & 2T_{\text{KT}} < T. \end{cases} \tag{11}$$

Hence, $\alpha(T)$ is zero for low temperatures and a monotonically increasing function of temperature just above T_{KT}. Including screening effects in 2D shows that this conclusion still holds, however the temperature at which it occurs is determined by screening.

Details of the simulations may be found in Ref. 18. The result is shown in Fig. 1 where we have the mean square dipole moment for the 2D case both as a function of temperature for various system sizes, and as function of system size for various temperatures. From this we may extract the scaling constant $\alpha(T)$ which is shown in the center panel of Fig. 1. A related method for using dipole fluctuations to measure vortex-unbinding has recently been used in Ref. 23.

Below a temperature $T\approx 1.3$, no scaling of $\langle s^2\rangle$ is seen, consistent with a low-temperature dielectric phase. The temperature at which scaling stops is consistent with the known temperature at which the 2D Coulomb gas suffers a metal-insulator transition.

Simulation results for the inverse dielectric constant are shown for a selection of system sizes in Fig. 2. Since ϵ^{-1} is expected to be discontinuous at T_c in the limit $\mathbf{k}\to 0$, we consider only the smallest possible wave vector in each system, $\mathbf{k}=(0,2\pi/L)$, and we see that the decrease of ϵ^{-1} towards zero with increasing T indeed gets sharper as L grows. It is, however, difficult to decide from these plots alone whether or not the dielectric constant is discontinuous at T_c. The fourth order term in the expansion of the free energy, ϵ_4 defined in Eq. (10), is therefore investigated in a corresponding manner and plotted in Fig. 3.

We note that this quantity has a dip at a temperature which can be associated with the transition temperature. If this dip remains finite and negative as L approaches infinity, ϵ^{-1} must exhibit a jump at T_c. The depth of the dip is shown in Fig. 4 for a variety of system sizes ranging from $L=4$ to $L=100$ and as a function of $1/L$. It clearly decreases with increasing L. However, from the positive curvature of the data in the log-log plot we may conclude that the depth remains nonzero when we extrapolate to $1/L=0$, a conclusion

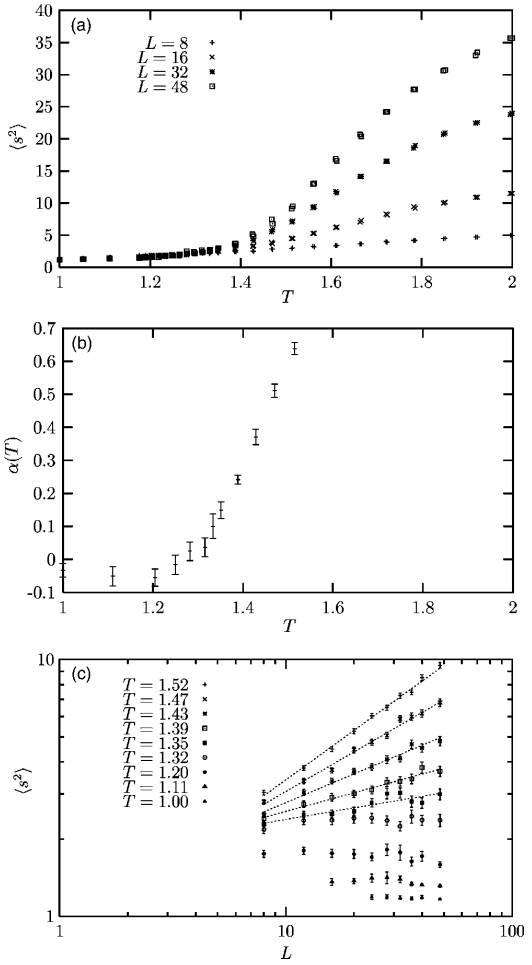

FIG. 1. The mean square dipole moment $\langle s^2\rangle$ as a function of temperature (top panel), and system size (bottom panel) for the 2D Coulomb gas. The middle panel shows the scaling exponent α extracted from $\langle s^2\rangle \sim L^{\alpha(T)}$.

reached by assuming power-law dependence of the depth on L.

We can now subtract from the depth a constant chosen so as to linearize the curve in the log-log plot. This constant consequently corresponds to the depth when extrapolating the data to the thermodynamic limit $1/L=0$, and we find this to be 0.047 ± 0.005.

By plotting the temperature at which the fourth order term has its minimum against $1/L$, we can follow a similar procedure as the above one. This is shown in Fig. 5. We linearize a log-log plot by subtracting a carefully chosen constant and end up with the number 1.36 ± 0.04. This is nothing else than an estimate of the critical temperature of the 2D CG, and compares well to earlier results.[24] The approach towards T_c is however a bit slow, making a precise determination of

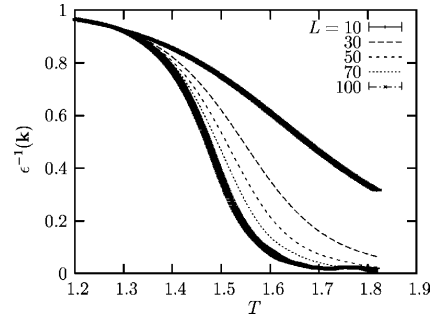

FIG. 2. Inverse dielectric constant taken at the smallest possible wave vector in a finite system $\mathbf{k}=(0,2\pi/L)$ and plotted against temperature T for system sizes $L=10$, 30, 50, 70, and 100 for the 2D Coulomb gas. The decrease of ϵ^{-1} towards zero becomes sharper with increasing L, consistent with the prediction of a discontinuous jump. Errorbars are given in the top and bottom curves, and omitted for clarity in the others.

the critical temperature difficult. This drawback was also noted by Minnhagen and Kim for the corresponding computations on the 2D XY model.[20]

B. 3D logarithmic system

We may carry out the same type of analysis for the mean square dipole moment for a system of point charges interacting via a three-dimensional logarithmic bare pair potential (3D LG). For this system, much less is known. Such a system has recently been considered in the context of studying confinement-deconfinement phase transitions in the $(2+1)$-dimensional Abelian Higgs model.[14] The results are shown in Fig. 6.

Qualitatively and quantitatively the results are the same in the 3D LG as for the 2D case. This strongly suggests that the 3D LG also has a low-temperature dielectric insulating phase

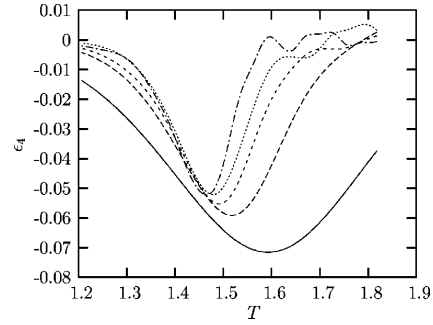

FIG. 3. The coefficient ϵ_4 of the fourth order term of the expansion of the free energy, for the 2D Coulomb gas. The same systems are used in this plot as in Fig. 2, and the depths decrease with increasing L. The important question is whether this dip vanishes at T_c or not. Errorbars are omitted but will be reintroduced in Fig. 4. The oscillation at high T is due to noise from the reweighting.

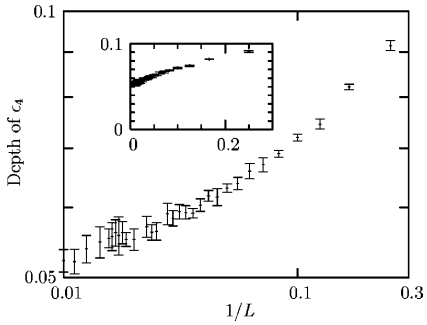

FIG. 4. Depth of the dip in the fourth order term shown in Fig. 3 for the 2D Coulomb gas. The data are obtained from simulations of system sizes ranging from $L=4$ to $L=100$ and plotted both on a linear scale (inset) and on a log-log scale. The positive curvature in the log-log plot clearly indicates a nonzero value of the depth when extrapolating to the limit $L\to\infty$.

separated by a phase transition from a high-temperature phase. In the low-temperature regime the charges of almost all dipoles are bound as tightly as possible, the separation of the charges correspond to the lattice constant. In the high-temperature regime the dipoles have started to separate, reflected by a scaling of $\langle s^2\rangle \sim L^{\alpha(T)}$ with the system size. Since $\alpha(T)=0$ at low temperatures while $\alpha(T)\neq 0$ in the high-temperature regime a non-analytic behavior of $\alpha(T)$ is implied. This necessarily corresponds to a phase transition in the vicinity of $T\approx 0.3$, a temperature which agrees well with Ref. 14 where a critical value of $T_c=1/3$ was obtained.

Note that, although this simple type of analysis of the mean square dipole moment does not by itself suffice to determine the character of these phase transitions either in the case of 3D LG or 2D CG, it does suffice to shed light on the important issue of whether a low temperature insulating phase exists in the 3D LG as well. This is far from obvious, since the screening properties of a three-dimensional system of charges interacting logarithmically is quite different from

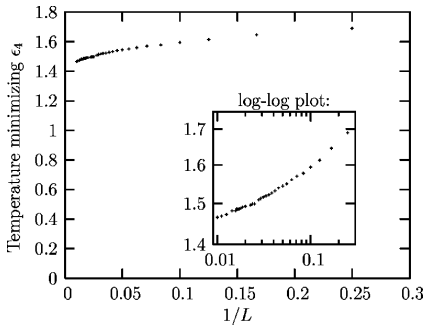

FIG. 5. Temperature minimizing ϵ_4 as a function of inverse system size for the 2D CG. The values are plotted both on a linear scale and on a log-log scale (inset). This temperature reaches a nonzero value at $L\to\infty$ indicated by the positive curvature in the log-log plot. Extrapolation gives $T_c=1.36\pm 0.04$.

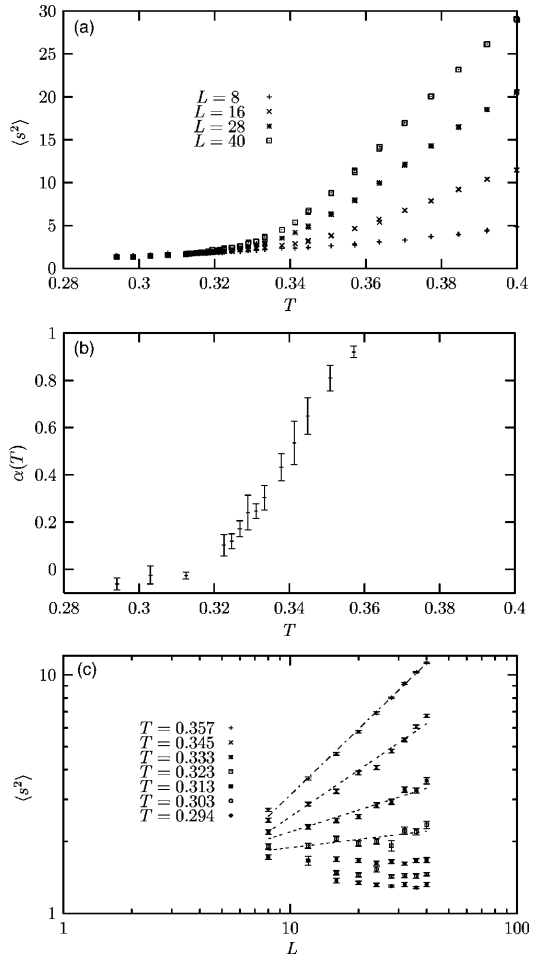

FIG. 6. Mean square dipole moment $\langle s^2\rangle$ as a function of temperature (top panel) and system size (bottom panel) for the 3D system of point charges interacting with a logarithmic bare pair potential (3D LG). The middle panel shows the scaling exponent α extracted from $\langle s^2\rangle \sim L^{\alpha(T)}$.

that of a Coulomb system (in any dimension).[16] It is therefore of considerable interest to repeat the analysis carried out for the 2D Coulomb gas to, if possible, determine the character of a metal-insulator transition in the 3D LG.

In Fig. 7 we show the inverse dielectric constant for the 3D LG as a function of temperature for various system sizes. It shows qualitatively the same behavior as for the 2D CG in that the decrease of ϵ^{-1} towards zero becomes sharper with increasing L. However, the downward drift in the temperature at which the inverse dielectric constant starts decreasing rapidly is more pronounced than in the 2D CG case.

In Fig. 8 we have plotted the fourth order coefficient against temperature for the 3D LG system, and the depth of the dip as a function of system size is shown in Fig. 9. It would clearly have been desirable to be able to access larger

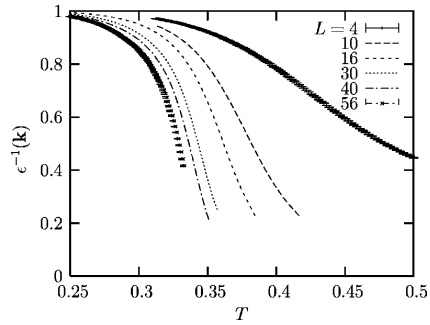

FIG. 7. Inverse dielectric constant taken at the smallest possible wave vector in a finite system, $\mathbf{k}=(0,2\pi/L,0)$, and plotted against temperature T for system sizes $L=4$, 10, 16, 30, 40, and 56, for the 3D LG system. The decrease of ϵ^{-1} towards zero becomes sharper with increasing L, consistent with the prediction of a discontinuous jump. However, the downward drift in the temperature at which the inverse dielectric constant starts decreasing rapidly is more pronounced than in the 2D CG case. Error bars are given in the top and bottom curves, and omitted for clarity in the others.

system sizes than what we have been able to do in the 3D LG case, to bring out a potential positive curvature that was observed in the 2D CG case. From these results, it is unfortunately not possible to tell whether the depth of the dip remains finite and negative as $L\to\infty$ of if it vanishes. Hence, we are presently not able to firmly conclude that the inverse dielectric constant in the 3D LG experiences a discontinuity.

The temperature locating the minimum in ϵ_4 as a function of system size is shown in Fig. 10 for the 3D LG system. Extrapolation gives $T_c=0.30\pm0.04$.

C. 3D Coulomb gas

In this subsection, we contrast the results of the 2D Coulomb gas and the 3D LG to those of the 3D Coulomb gas. The 3D CG is known to be in a metallic high-temperature

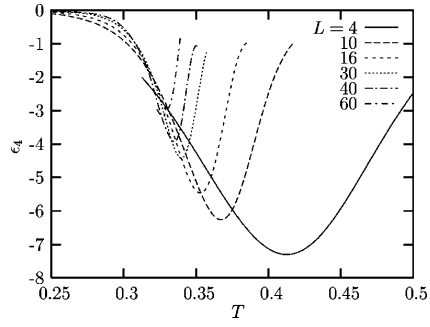

FIG. 8. The coefficient ϵ_4 of the fourth order term of the expansion of the free energy for the 3D LG model. The depths decrease with increasing L, and the important question is whether this dip vanishes at T_c or not. Errorbars are omitted but will be reintroduced in Fig. 9.

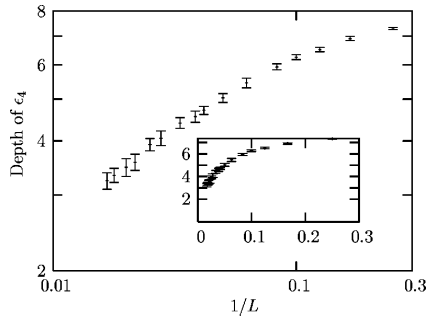

FIG. 9. Depth of the dip in the fourth order term shown in Fig. 8 for the 3D LG. The data are obtained from simulations of system sizes ranging from $L=4$ to $L=60$ and plotted both on a linear scale (inset) and on a log-log scale. The lack of clear positive curvature in the log-log plot that was observed in 2D CG case makes the extrapolation to the limit $L\to\infty$ more difficult for the system sizes we have been able to access in 3D.

phase for *all* finite temperatures and should exhibit quite different finite-size scaling of $\langle s^2\rangle$ compared to the 2D CG case.[11,14,25] The results are shown in Fig. 11. Note that the temperature dependence of the curves for all different system sizes are qualitatively different in the 3D CG compared to those in the 2D CG and the 3D LG. This becomes particularly apparent upon considering the L dependence of $\langle s^2\rangle$ for various temperatures, where the steepness of the curves increases with decreasing temperature, resulting in a scaling exponent $\alpha(T)$ (from $\langle s^2\rangle\sim L^{\alpha(T)}$) which decreases with increasing temperature. This is quite consistent with what is known for the 3D CG, namely, that it exhibits a metallic state for all finite temperatures, equivalently it corresponds to Polyakov's permanent confinement.[11,14] It is evident that the scaling results for $\langle s^2\rangle$ for the 2D CG and the 3D LG are qualitatively and quantitatively the same, and that they are qualitatively different from those exhibited by the 3D CG. For low temperatures, $\langle s^2\rangle$ seem to be increasing with temperature. This is only a vacuum effect, since vacuum con-

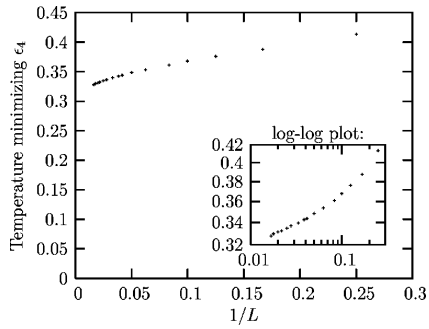

FIG. 10. Temperature minimizing ϵ_4 as a function of inverse system size for the 3D LG system. The values are plotted both on a linear scale and on a log-log scale (inset). This temperature reaches a nonzero value at $L\to\infty$. Extrapolation gives $T_c=0.30\pm0.04$.

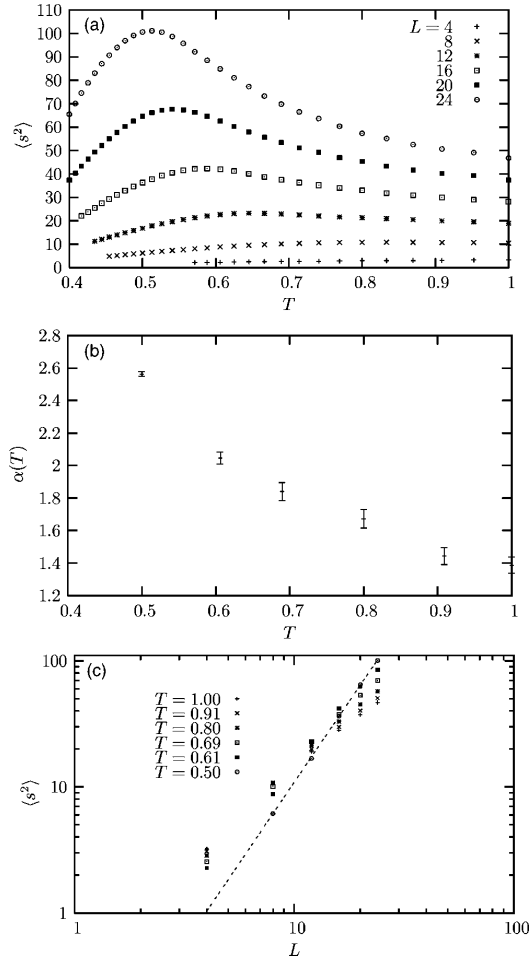

FIG. 11. Mean square dipole moment $\langle s^2\rangle$ as a function of temperature (top panel) and system size (bottom panel) for the 3D Coulomb gas system of point charges interacting with a $1/r$ bare pair potential. The middle panel shows the scaling exponent α extracted from $\langle s^2\rangle \sim L^{\alpha(T)}$.

figurations do not contribute to the measurement of $\langle s^2\rangle$.[18] This means that close to vacuum, only configurations resulting from the insertion of one single dipole at the smallest possible distance will contribute. See also Sec. IV D.

The inverse dielectric constant for the 3D CG is shown as a function of temperature in Fig. 12 with system sizes ranging up to $L=50$. Here also, ϵ^{-1} decreases from unity to zero, but the downward drift in the temperature at which ϵ^{-1} deviates from unity seems to be even stronger than for the 3D LG model. Additionally, the decrease towards zero does not sharpen significantly with increasing L.

We find a similar minimum in the fourth order term in the expansion of the free energy for the 3D CG, ϵ_4/L^2, shown in Fig. 13. However, the dip vanishes as $L\to\infty$ in the current

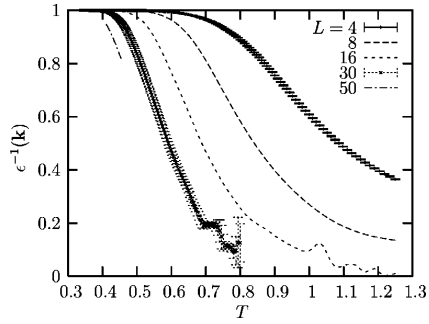

FIG. 12. Inverse dielectric constant taken at the smallest possible wave vector in a finite system, $\mathbf{k}=(0,2\pi/L,0)$, and plotted against temperature T for system sizes $L=4$, 8, 16, 30, and 50, for the 3D CG system. The decrease of ϵ^{-1} towards zero does not sharpen with increasing L, and there is a clear downward drift in the temperature at which ϵ^{-1} deviates from unity. Error bars are given in two of the curves, and omitted for clarity in the others.

model. This is clearly shown in Fig. 14 in contrast to the Figs. 4 and 9 of the other two models.

For completeness we have included in Fig. 15 a plot of the temperature locating the minimum in ϵ_4 as a function of system size also for the 3D CG. There is no phase transition to which this temperature is associated, and the stronger downward drift mentioned above is evident when contrasting this plot to Fig. 10 of the 3D LG. The temperature is reduced by a factor 2 in the largest system considered in the 3D CG compared to the smallest whereas the variation is much smaller in the 3D LG. However, there *is* a weak curvature in the log-log version of Fig. 15. Performing a similar extrapolation as we did for the other two models we end up with a "critical" temperature $T_c=0.24\pm0.04$.

D. Charge density

Finally we present in Fig. 16 the charge density for the three models considered. In all three cases the charge densi-

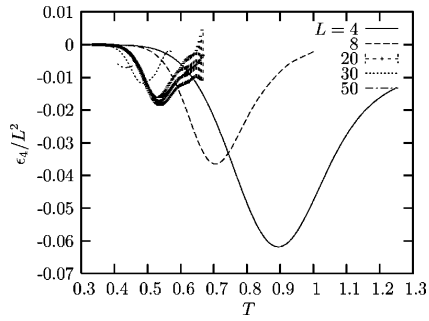

FIG. 13. The coefficient ϵ_4 of the fourth order term of the expansion of the free energy, for the 3D CG. The depths decrease with increasing L and seem to vanish as $L\to\infty$. Errorbars are shown for one of the systems for demonstration.

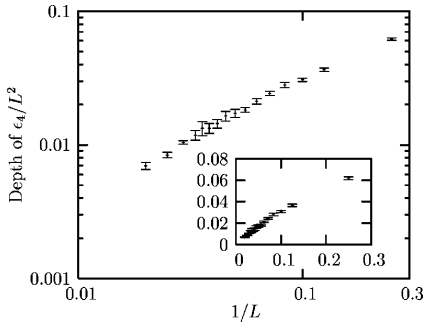

FIG. 14. Depth of the dip in the fourth order term shown in Fig. 13 for the 3D CG. The data are obtained from simulations of system sizes ranging from $L=4$ to $L=50$ and plotted both on a linear scale (inset) and on a log-log scale. It is clear that the dip vanishes in the thermodynamic limit.

ties are independent of L and from these curves we can approximate the average separation r_{mean} between the charges assuming uniform distribution

$$r_{\mathrm{mean}} = \left(\frac{1}{Q_{\mathrm{Sum}}/V}\right)^{1/d}, \tag{12}$$

where d is the dimension. We concentrate on the (L-dependent) temperatures which minimize ϵ_4. In the two logarithmically interacting models, r_{mean} ranges from ~ 4 for the smallest systems and up to ~ 8 for the largest. In the 3D Coulomb gas on the other hand, r_{mean} remains close to L even for the largest system sizes meaning that the systems are close to their vacuum states at these temperatures. This strongly suggests that the features we investigate are only extreme low-density effects in the 3D CG model. Screening, which should take place at all temperatures in a system always being in a metallic state, is not possible in this limit.

In the 2D CG and 3D LG models the situation is different. The interesting temperature domains are smaller and the charge densities are kept close to constant which in turn allows screening for the largest systems.

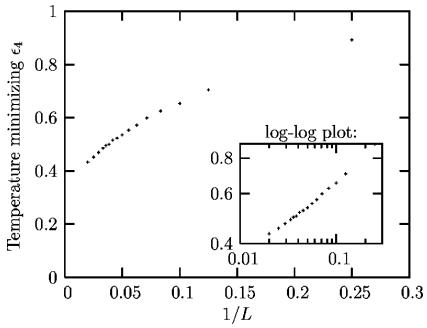

FIG. 15. Temperature minimizing ϵ_4 as a function of inverse system size for the 3D CG system. The values are plotted both on a linear scale and on a log-log scale (inset).

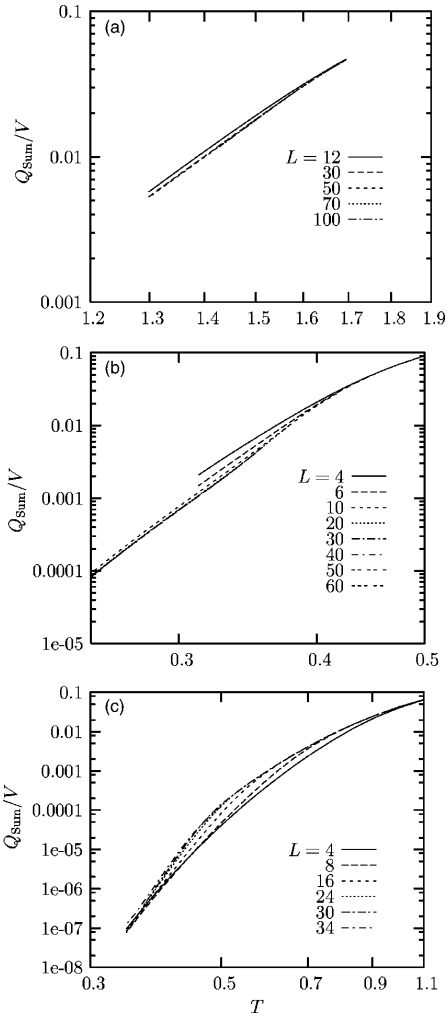

FIG. 16. Charge density Q_{sum}/V plotted vs temperature on log-log scales for the (a) 2D CG, (b) 3D LG, and (c) 3D CG models. The volume V corresponds to the total number of sites L^d. Note that Q_{sum}/V is independent of system size L in all three cases.

V. COMMENTS ON UNIVERSALITY

In the 2D CG, the universal jump to zero of the inverse dielectric constant ϵ^{-1} is given by[19,26]

$$\epsilon^{-1} = \frac{2T_c}{\pi}. \tag{13}$$

Using the estimate for the critical temperature found in section IV A, the value at T_c should, according to Eq. (13), be $\epsilon^{-1}=0.86\pm0.03$. This is in agreement with Fig. 2, since it is in this region the curves seem to split.

In Ref. 20, it was speculated that the finite negative value of the fourth order modulus $\langle Y_4\rangle \approx -0.130$ could be associ-

ated with a universal number. In the 2D CG, $V_k \sim L^2$ and $Q_k^y \sim 2\pi/L$ for large L, such that the modification $\Delta \rightarrow \Delta/(\sqrt{2}\pi)$ turns Eq. (8) into

$$F(\mathbf{T}) - F(0) = \frac{\Delta^2}{2}\epsilon^{-1} + \frac{\Delta^4}{4!}3\epsilon_4. \tag{14}$$

This means that if ϵ^{-1} corresponds to the helicity modulus $\langle Y \rangle$, it is $3\epsilon_4$ that corresponds to the fourth order modulus $\langle Y_4 \rangle$. It is interesting to notice that $3\epsilon_4 = -0.141 \pm 0.015$ fits nicely with the value found in Ref. 20, speculated to be a universal number. One may therefore speculate that the value of ϵ_4 at T_c is a universal number independent of T_c. Whether this is a sign of a true universality or a mere coincidence requires further investigation.

One should also note that with this modification of Δ, the additional twist term in the *XY* Hamiltonian (1) becomes $\sqrt{2}\Delta \sin(2\pi y/L)/L$. It seems natural to suggest that the net effect of a sine twist is given by its r.m.s. value, i.e., $[1/L\int_0^L \sin^2(2\pi y/L)dy]^{1/2} = 1/\sqrt{2}$. This gives a net twist of Δ across the system, which is the same as in Ref. 20.

The universal jump of ϵ^{-1} in the 3D LG is given by the flow equations derived in Ref. 14. In our units, this jump is predicted to be

$$\epsilon^{-1} = \frac{5T_c}{2}, \tag{15}$$

and by using the critical temperature found in section IV B, this amounts to an ϵ^{-1} in the interval (0.65,0.85). Since the different curves in Fig. 7 do not merge in the low-temperature regime, as they do in the 2D CG case, it is difficult to make a precise determination of the jump in the 3D LG based on these simulations. However, one cannot rule out that the jump lies inside the interval mentioned.

VI. CONCLUDING REMARKS

In this paper we have considered various quantities related to a possible phase transition in systems of point charges interacting with bare logarithmic pair potentials, in 2D and 3D. We have also carried out comparisons with the results obtained in the 3D Coulomb gas in some cases. The quantities we have focused on are the fluctuations of the dipole moment $\langle s^2 \rangle$ and the fourth order coefficient of the free energy expanded in an appropriate twist. We have shown that the dipole moment fluctuations, associated with the polarizability of the charge systems, has a scaling exponent $\alpha(T)$ defined by $\langle s^2 \rangle \sim L^{\alpha(T)}$ which is positive above some temperature and zero below this temperature for the 2D CG and the 3D LG cases, and is an increasing function of temperature. On the other hand, for the 3D CG case $\alpha(T)$ is finite positive for all temperatures we have considered, and is a *decreasing* function of temperature. This in itself strongly suggests that the 3D LG has statistical physics much more akin to the 2D CG than to the 3D CG. For the 2D CG we have demonstrated that the inverse dielectric constant experiences a discontinuous jump to zero at the phase transition. This has been done by investigation of a series expansion of free energy using Monte Carlo simulations. The possibility of a universal value of the fourth order term proposed in Ref. 20 has also been commented on, and a possible agreement with this value has been observed. The method developed in this paper will apply to any gas of vortex loops or point charges with any interaction potential. We have applied it to the 3D LG. Although it would have been desirable to be able to access larger system sizes than what we have been able to in the present paper, the results we obtain for the 3D LG suggest that this model may also undergo a metal-insulator transition with a discontinuity in the inverse dielectric function at the critical point, in agreement with the renormalization group results of Ref. 14.

ACKNOWLEDGMENTS

This work was supported by the Research Council of Norway, Grant Nos. 158518/431, 158547/431 (NANOMAT), and by the Norwegian High Performance Computing Consortium (NOTUR). One of us (S. K.) acknowledges support from the Norwegian University of Science and Technology. We acknowledge useful discussions with F. S. Nogueira and Z. Tesanovic.

APPENDIX A: DUALITY TRANSFORMATION

The partition function for the *XY* model with coupling constant $J=1$ is

$$Z = \Pi_i \int \frac{d\theta_i}{2\pi} e^{\beta \Sigma_{\mathbf{r}} \cos(\nabla\theta - 2\pi\mathbf{T})}, \tag{A1}$$

where the sum is over all links between lattice points $\nabla\theta \equiv \theta_i - \theta_j$ and $\mathbf{T}(\mathbf{r})$ is the twist between the two lattice points sharing the link $\mathbf{r}$. We will consider three spatial dimensions and comment on any differences in 2D. Applying the Villain approximation, we get

$$Z = \int \mathcal{D}\theta \sum_{\{\mathbf{n}\}} e^{-(\beta/2)\Sigma_{\mathbf{r}}(\nabla\theta - 2\pi\mathbf{T} - 2\pi\mathbf{n})^2}. \tag{A2}$$

$\mathbf{n}(\mathbf{r})$ is an integer-valued field taking care of the periodicity of the cosine. By a Hubbard-Stratonovich decoupling, one finds

$$Z = \int \mathcal{D}\theta \mathcal{D}\mathbf{v} \sum_{\{\mathbf{n}\}} e^{-\Sigma_{\mathbf{r}}\left[(1/2\beta)\mathbf{v}^2 + i\mathbf{v}\cdot(\nabla\theta - 2\pi\mathbf{T} - 2\pi\mathbf{n})\right]}. \tag{A3}$$

The summation over $\mathbf{n}$ may now be evaluated using the Poisson summation formula

$$\sum_{n=-\infty}^{\infty} e^{2\pi i n v} = \sum_{l=-\infty}^{\infty} \delta(v - l) \tag{A4}$$

at each dual lattice point, yielding

$$Z = \int \mathcal{D}\theta \sum_{\{\mathbf{l}\}} e^{\Sigma_{\mathbf{r}} 2\pi i \mathbf{l}\cdot\mathbf{T} - i\mathbf{l}\cdot\nabla\theta - (1/2\beta)\mathbf{l}^2}. \tag{A5}$$

The field $\mathbf{l}(\mathbf{r})$ is integer valued. Now, performing a partial summation on the second term in the exponent, the θ integration may be carried out. This produces the constraint that $\mathbf{l}$ must be divergence free, solved by the introduction of another integer-valued field such that $\mathbf{l}=\nabla\times\mathbf{h}$. Note that $\mathbf{h}(\mathbf{r})$ is a scalar in 2D. The partition function is now

$$Z=\sum_{\{\mathbf{h}\}} e^{\Sigma_{\mathbf{r}} 2\pi i(\nabla\times\mathbf{h})\cdot\mathbf{T}-(1/2\beta)(\nabla\times\mathbf{h})^2}, \tag{A6}$$

and we observe that $\mathbf{h}\rightarrow\mathbf{h}+\nabla\phi$ is a gauge transformation. In two dimensions, the corresponding gauge transformation is $h\rightarrow h+c$, where c is a constant. Using Poisson's summation formula once more, we get

$$Z=\int \mathcal{D}\mathbf{h}\sum_{\{\mathbf{m}\}} e^{\Sigma_{\mathbf{r}} 2\pi i(\nabla\times\mathbf{h})\cdot\mathbf{T}-(1/2\beta)(\nabla\times\mathbf{h})^2+2\pi i\mathbf{h}\cdot\mathbf{m}}, \tag{A7}$$

leaving $\mathbf{h}$ no longer integer valued. The field $\mathbf{m}(\mathbf{r})$ is what corresponds to vortex excitations in the *XY* model. The gauge invariance of the theory produces the constraint $\Sigma_{\mathbf{r}}\phi(\nabla\cdot\mathbf{m})=0$ for all configurations of $\mathbf{m}$. Choosing for instance $\phi=\nabla\cdot\mathbf{m}$, it is clear that $\mathbf{m}$ must be divergence free, i.e., the field lines are closed loops. In 2D, the corresponding constraint is $\Sigma_{\mathbf{r}} m=0$, indicating an overall charge neutrality in the 2D Coulomb gas or zero total vorticity in the 2D *XY* model.

By another partial summation, we are now left with a Maxwell term and a coupling term between the gauge field $\mathbf{h}$ and the current $\mathbf{M}(\mathbf{r})\equiv\mathbf{m}+\nabla\times\mathbf{T}$:

$$Z=\int \mathcal{D}\mathbf{h}\sum_{\{\mathbf{m}\}} e^{\Sigma_{\mathbf{r}} 2\pi i\mathbf{h}\cdot\mathbf{M}-(1/2\beta)(\nabla\times\mathbf{h})^2}. \tag{A8}$$

One may now perform a partial integration in the second term and use the gauge where $\nabla\cdot\mathbf{h}=0$, such that $\nabla\times\nabla\times\mathbf{h}=-\nabla^2\mathbf{h}$. Then, by going to Fourier space and completing squares, the $\mathbf{h}$ integration becomes Gaussian. This leaves us with

$$Z=Z_0\sum_{\{\mathbf{m}\}} e^{(2\beta\pi^2/N)\Sigma_{\mathbf{q}}\mathbf{M}_{\mathbf{q}}G_{\mathbf{q}}^{-1}\mathbf{M}_{-\mathbf{q}}}, \tag{A9}$$

where $\nabla^2 e^{\pm i\mathbf{q}\cdot\mathbf{r}}\equiv e^{\pm i\mathbf{q}\cdot\mathbf{r}}G_{\mathbf{q}}$ and Z_0 is a constant. Defining the discrete Laplacian by

$$\Delta^2 f(\mathbf{r})=\sum_{\mu}[f(\mathbf{r}+\hat{e}_\mu)+f(\mathbf{r}-\hat{e}_\mu)-2f(\mathbf{r})], \tag{A10}$$

it is clear that $G_{\mathbf{q}}=-2(d-\Sigma_{\mu=1}^{d}\cos q_\mu)$, denoting the number of space dimensions by d. Returning to real-space representation, we arrive at

$$Z=Z_0\sum_{\{\mathbf{m}\}} e^{-(\beta/2)\Sigma_{\mathbf{r}_i,\mathbf{r}_j}\mathbf{M}(\mathbf{r}_i)V(|\mathbf{r}_i-\mathbf{r}_j|)\mathbf{M}(\mathbf{r}_j)}, \tag{A11}$$

the interaction being given by

$$V(\mathbf{r})=\frac{2\pi^2}{L^2}\sum_{\mathbf{q}}\frac{e^{i\mathbf{q}\cdot\mathbf{r}}}{d-\sum_{\mu=1}^{d}\cos q_\mu}. \tag{A12}$$

APPENDIX B: EXPANSION OF FREE ENERGY

Consider the Hamiltonian

$$H_0=\frac{1}{2}\sum_{i,j}\mathbf{m}_i V_{ij}\mathbf{m}_j, \tag{B1}$$

describing a 3D system of integer-valued currents $\mathbf{m}$ on a lattice interacting via the potential $V_{ij}=V(|\mathbf{r}_i-\mathbf{r}_j|)$. We impose periodic boundary conditions on the system. Perturbing the field $\mathbf{m}$ with a transversal twist turns Eq. (B1) into

$$H=\frac{1}{2}\sum_{i,j}(\mathbf{m}+\nabla\times\mathbf{T})_i V_{ij}(\mathbf{m}+\nabla\times\mathbf{T})_j. \tag{B2}$$

We let the linear system size be L and define the discrete Fourier transform by

$$f_{\mathbf{q}}=\sum_{\mathbf{r}} f(\mathbf{r})e^{i\mathbf{q}\cdot\mathbf{r}}, \tag{B3}$$

where $\mathbf{r}=(n_x,n_y,n_z)$ and $n_i=0,\ldots,L-1$. The inverse transform is

$$f(\mathbf{r})=\frac{1}{N}\sum_{\mathbf{q}} f_{\mathbf{q}}e^{-i\mathbf{q}\cdot\mathbf{r}}, \tag{B4}$$

where $\mathbf{q}=2\pi/L(k_x,k_y,k_z)$ and $k_i=-L/2+1,\ldots,L/2$. N is the number of lattice sites. Let us also define $Q_{\pm\mathbf{q}}^{\nu}$ by $\Delta^\nu e^{\pm i\mathbf{q}\cdot\mathbf{r}}=e^{\pm i\mathbf{q}\cdot\mathbf{r}}Q_{\pm\mathbf{q}}^{\nu}$, where Δ^ν is a lattice derivative. In Fourier representation the Hamiltonian becomes

$$H=\frac{1}{2N}\sum_{\mathbf{q}}(m_{\mathbf{q}}^{\mu}+\varepsilon^{\mu\nu\lambda}Q_{-\mathbf{q}}^{\nu}T_{\mathbf{q}}^{\lambda})V_{\mathbf{q}}(m_{-\mathbf{q}}^{\mu}+\varepsilon^{\mu\rho\sigma}Q_{\mathbf{q}}^{\rho}T_{-\mathbf{q}}^{\sigma}). \tag{B5}$$

For later use, we calculate the derivative of H, which is

$$\frac{\partial H}{\partial T_{\mathbf{q}_1}^{\alpha}}=\frac{1}{N}\varepsilon^{\mu\nu\alpha}Q_{-\mathbf{q}_1}^{\nu}(m_{-\mathbf{q}_1}^{\mu}+\varepsilon^{\mu\rho\sigma}Q_{\mathbf{q}_1}^{\rho}T_{-\mathbf{q}_1}^{\sigma})V_{\mathbf{q}_1}. \tag{B6}$$

We also note that

$$\frac{\partial^2 H}{\partial T_{\mathbf{q}_1}^{\alpha}\partial T_{\mathbf{q}_2}^{\beta}}=\frac{1}{N}\varepsilon^{\mu\nu\alpha}\varepsilon^{\mu\rho\beta}Q_{-\mathbf{q}_1}^{\nu}Q_{\mathbf{q}_1}^{\rho}V_{\mathbf{q}_1}\delta_{\mathbf{q}_1+\mathbf{q}_2,0} \tag{B7}$$

is independent of $\mathbf{m}$ and that all higher order derivatives are zero.

The free energy is given by $F=-T\ln Z$, where the partition function is

$$Z=\sum_{\{\mathbf{m}\}} e^{-H/T}, \tag{B8}$$

summing over all possible configurations of $\mathbf{m}$. By Taylor expansion of the free energy in the twist, we get

$$F(\mathbf{T})-F(0)=\sum_{\alpha}\sum_{\mathbf{r}_1}\left.\frac{\partial F}{\partial T^{\alpha}(\mathbf{r}_1)}\right|_{\mathbf{T}=0}T^{\alpha}(\mathbf{r}_1)+\sum_{\alpha,\beta}\sum_{\mathbf{r}_1,\mathbf{r}_2}\left.\frac{\partial^2 F}{\partial T^{\alpha}(\mathbf{r}_1)\partial T^{\beta}(\mathbf{r}_2)}\right|_{\mathbf{T}=0}T^{\alpha}(\mathbf{r}_1)T^{\beta}(\mathbf{r}_2)+\cdots. \tag{B9}$$

Note that $F(\mathbf{T}=0)$ refers to the free energy of the unperturbed system described by H_0. By writing each term in the series in Fourier representation, one finds the equivalent expansion in Fourier components of the twist, i.e.,

$$F(\mathbf{T}) - F(0) = \sum_{\alpha} \sum_{\mathbf{q}_1} \left. \frac{\partial F}{\partial T^{\alpha}_{\mathbf{q}_1}} \right|_{\mathbf{T}=0} T^{\alpha}_{\mathbf{q}_1} + \sum_{\alpha,\beta} \sum_{\mathbf{q}_1 \mathbf{q}_2} \left. \frac{\partial^2 F}{\partial T^{\alpha}_{\mathbf{q}_1} \partial T^{\beta}_{\mathbf{q}_2}} \right|_{\mathbf{T}=0} \frac{T^{\alpha}_{\mathbf{q}_1} T^{\beta}_{\mathbf{q}_2}}{2} + \cdots . \tag{B10}$$

The first derivative becomes

$$\frac{\partial F}{\partial T^{\alpha}_{\mathbf{q}_1}} = \frac{1}{Z} \sum_{\{\mathbf{m}\}} \frac{\partial H}{\partial T^{\alpha}_{\mathbf{q}_1}} e^{-H/T} \equiv \left\langle \frac{\partial H}{\partial T^{\alpha}_{\mathbf{q}_1}} \right\rangle . \tag{B11}$$

Proceeding, we find

$$\frac{\partial^2 F}{\partial T^{\alpha}_{\mathbf{q}_1} \partial T^{\beta}_{\mathbf{q}_2}} = \frac{1}{T} \left\langle \frac{\partial H}{\partial T^{\alpha}_{\mathbf{q}_1}} \right\rangle \left\langle \frac{\partial H}{\partial T^{\beta}_{\mathbf{q}_2}} \right\rangle + \frac{\partial^2 H}{\partial T^{\alpha}_{\mathbf{q}_1} \partial T^{\beta}_{\mathbf{q}_2}} - \frac{1}{T} \left\langle \frac{\partial H}{\partial T^{\alpha}_{\mathbf{q}_1}} \frac{\partial H}{\partial T^{\beta}_{\mathbf{q}_2}} \right\rangle \tag{B12}$$

for the second derivative and

$$\frac{\partial^3 F}{\partial T^{\alpha}_{\mathbf{q}_1} \partial T^{\beta}_{\mathbf{q}_2} \partial T^{\gamma}_{\mathbf{q}_3}} = \frac{1}{T^2} \left[2 \left\langle \frac{\partial H}{\partial T^{\alpha}_{\mathbf{q}_1}} \right\rangle \left\langle \frac{\partial H}{\partial T^{\beta}_{\mathbf{q}_2}} \right\rangle \left\langle \frac{\partial H}{\partial T^{\gamma}_{\mathbf{q}_3}} \right\rangle + \left\langle \frac{\partial H}{\partial T^{\alpha}_{\mathbf{q}_1}} \frac{\partial H}{\partial T^{\beta}_{\mathbf{q}_2}} \frac{\partial H}{\partial T^{\gamma}_{\mathbf{q}_3}} \right\rangle - \left\langle \frac{\partial H}{\partial T^{\alpha}_{\mathbf{q}_1}} \right\rangle \times \left\langle \frac{\partial H}{\partial T^{\beta}_{\mathbf{q}_2}} \frac{\partial H}{\partial T^{\gamma}_{\mathbf{q}_3}} \right\rangle - \left\langle \frac{\partial H}{\partial T^{\beta}_{\mathbf{q}_2}} \right\rangle \left\langle \frac{\partial H}{\partial T^{\alpha}_{\mathbf{q}_1}} \frac{\partial H}{\partial T^{\gamma}_{\mathbf{q}_3}} \right\rangle - \left\langle \frac{\partial H}{\partial T^{\gamma}_{\mathbf{q}_3}} \right\rangle \left\langle \frac{\partial H}{\partial T^{\alpha}_{\mathbf{q}_1}} \frac{\partial H}{\partial T^{\beta}_{\mathbf{q}_2}} \right\rangle \right] \tag{B13}$$

for the third. We have exploited the fact that third derivatives of H vanishes. The fourth derivative is found to be

$$\begin{aligned} \frac{\partial^4 F}{\partial T^{\alpha}_{\mathbf{q}_1} \partial T^{\beta}_{\mathbf{q}_2} \partial T^{\gamma}_{\mathbf{q}_3} \partial T^{\delta}_{\mathbf{q}_4}} = \frac{1}{T^3} \Bigg\{ & 6 \left\langle \frac{\partial H}{\partial T^{\alpha}_{\mathbf{q}_1}} \right\rangle \left\langle \frac{\partial H}{\partial T^{\beta}_{\mathbf{q}_2}} \right\rangle \left\langle \frac{\partial H}{\partial T^{\gamma}_{\mathbf{q}_3}} \right\rangle \left\langle \frac{\partial H}{\partial T^{\delta}_{\mathbf{q}_4}} \right\rangle - 2 \Bigg[\left\langle \frac{\partial H}{\partial T^{\alpha}_{\mathbf{q}_1}} \right\rangle \left\langle \frac{\partial H}{\partial T^{\beta}_{\mathbf{q}_2}} \right\rangle \left\langle \frac{\partial H}{\partial T^{\gamma}_{\mathbf{q}_3}} \frac{\partial H}{\partial T^{\delta}_{\mathbf{q}_4}} \right\rangle \\ & + \left\langle \frac{\partial H}{\partial T^{\alpha}_{\mathbf{q}_1}} \right\rangle \left\langle \frac{\partial H}{\partial T^{\gamma}_{\mathbf{q}_3}} \right\rangle \left\langle \frac{\partial H}{\partial T^{\beta}_{\mathbf{q}_2}} \frac{\partial H}{\partial T^{\delta}_{\mathbf{q}_4}} \right\rangle + \left\langle \frac{\partial H}{\partial T^{\alpha}_{\mathbf{q}_1}} \right\rangle \left\langle \frac{\partial H}{\partial T^{\delta}_{\mathbf{q}_4}} \right\rangle \left\langle \frac{\partial H}{\partial T^{\beta}_{\mathbf{q}_2}} \frac{\partial H}{\partial T^{\gamma}_{\mathbf{q}_3}} \right\rangle + \left\langle \frac{\partial H}{\partial T^{\beta}_{\mathbf{q}_2}} \right\rangle \left\langle \frac{\partial H}{\partial T^{\gamma}_{\mathbf{q}_3}} \right\rangle \left\langle \frac{\partial H}{\partial T^{\alpha}_{\mathbf{q}_1}} \frac{\partial H}{\partial T^{\delta}_{\mathbf{q}_4}} \right\rangle \\ & + \left\langle \frac{\partial H}{\partial T^{\beta}_{\mathbf{q}_2}} \right\rangle \left\langle \frac{\partial H}{\partial T^{\delta}_{\mathbf{q}_4}} \right\rangle \left\langle \frac{\partial H}{\partial T^{\alpha}_{\mathbf{q}_1}} \frac{\partial H}{\partial T^{\gamma}_{\mathbf{q}_3}} \right\rangle + \left\langle \frac{\partial H}{\partial T^{\gamma}_{\mathbf{q}_3}} \right\rangle \left\langle \frac{\partial H}{\partial T^{\delta}_{\mathbf{q}_4}} \right\rangle \left\langle \frac{\partial H}{\partial T^{\alpha}_{\mathbf{q}_1}} \frac{\partial H}{\partial T^{\beta}_{\mathbf{q}_2}} \right\rangle \Bigg] + \left\langle \frac{\partial H}{\partial T^{\alpha}_{\mathbf{q}_1}} \right\rangle \left\langle \frac{\partial H}{\partial T^{\beta}_{\mathbf{q}_2}} \frac{\partial H}{\partial T^{\gamma}_{\mathbf{q}_3}} \frac{\partial H}{\partial T^{\delta}_{\mathbf{q}_4}} \right\rangle \\ & + \left\langle \frac{\partial H}{\partial T^{\beta}_{\mathbf{q}_2}} \right\rangle \left\langle \frac{\partial H}{\partial T^{\alpha}_{\mathbf{q}_1}} \frac{\partial H}{\partial T^{\gamma}_{\mathbf{q}_3}} \frac{\partial H}{\partial T^{\delta}_{\mathbf{q}_4}} \right\rangle + \left\langle \frac{\partial H}{\partial T^{\gamma}_{\mathbf{q}_3}} \right\rangle \left\langle \frac{\partial H}{\partial T^{\alpha}_{\mathbf{q}_1}} \frac{\partial H}{\partial T^{\beta}_{\mathbf{q}_2}} \frac{\partial H}{\partial T^{\delta}_{\mathbf{q}_4}} \right\rangle + \left\langle \frac{\partial H}{\partial T^{\delta}_{\mathbf{q}_4}} \right\rangle \left\langle \frac{\partial H}{\partial T^{\alpha}_{\mathbf{q}_1}} \frac{\partial H}{\partial T^{\beta}_{\mathbf{q}_2}} \frac{\partial H}{\partial T^{\gamma}_{\mathbf{q}_3}} \right\rangle \\ & + \left\langle \frac{\partial H}{\partial T^{\alpha}_{\mathbf{q}_1}} \frac{\partial H}{\partial T^{\beta}_{\mathbf{q}_2}} \right\rangle \left\langle \frac{\partial H}{\partial T^{\gamma}_{\mathbf{q}_3}} \frac{\partial H}{\partial T^{\delta}_{\mathbf{q}_4}} \right\rangle + \left\langle \frac{\partial H}{\partial T^{\alpha}_{\mathbf{q}_1}} \frac{\partial H}{\partial T^{\gamma}_{\mathbf{q}_3}} \right\rangle \left\langle \frac{\partial H}{\partial T^{\beta}_{\mathbf{q}_2}} \frac{\partial H}{\partial T^{\delta}_{\mathbf{q}_4}} \right\rangle + \left\langle \frac{\partial H}{\partial T^{\alpha}_{\mathbf{q}_1}} \frac{\partial H}{\partial T^{\delta}_{\mathbf{q}_4}} \right\rangle \left\langle \frac{\partial H}{\partial T^{\beta}_{\mathbf{q}_2}} \frac{\partial H}{\partial T^{\gamma}_{\mathbf{q}_3}} \right\rangle \\ & - \left\langle \frac{\partial H}{\partial T^{\alpha}_{\mathbf{q}_1}} \frac{\partial H}{\partial T^{\beta}_{\mathbf{q}_2}} \frac{\partial H}{\partial T^{\gamma}_{\mathbf{q}_3}} \frac{\partial H}{\partial T^{\delta}_{\mathbf{q}_4}} \right\rangle \Bigg\} . \end{aligned} \tag{B14}$$

Remembering that

$$\left. \frac{\partial H}{\partial T^{\alpha}_{\mathbf{q}_1}} \right|_{\mathbf{T}=0} = \frac{1}{N} \varepsilon^{\mu\nu\alpha} Q^{\nu}_{-\mathbf{q}_1} m^{\mu}_{-\mathbf{q}_1} V_{\mathbf{q}_1}, \tag{B15}$$

it is straightforward to write the derivatives at zero twist as $\mathbf{m}$ correlators. However, in many cases these expressions may be simplified further. If the sum over all possible configurations $\{\mathbf{m}\}$ is symmetric around zero, one finds that all odd-order correlators are zero, resulting in

$$\left. \frac{\partial F}{\partial T^{\alpha}_{\mathbf{q}_1}} \right|_{\mathbf{T}=0} = \left. \frac{\partial^3 F}{\partial T^{\alpha}_{\mathbf{q}_1} \partial T^{\beta}_{\mathbf{q}_2} \partial T^{\gamma}_{\mathbf{q}_3}} \right|_{\mathbf{T}=0} = 0. \tag{B16}$$

Furthermore, since $V_{ij} = V(|\mathbf{r}_i - \mathbf{r}_j|)$, i.e., we have a translationally invariant system, the even-order correlators are subject to relations such as

$$\langle m^{\mu}_{-\mathbf{q}_1} m^{\nu}_{-\mathbf{q}_2} \rangle = \langle m^{\mu}_{-\mathbf{q}_1} m^{\nu}_{-\mathbf{q}_2} \rangle \delta_{\mathbf{q}_1 + \mathbf{q}_2, 0} \tag{B17}$$

and

$$\langle m^{\mu}_{-\mathbf{q}_1} m^{\nu}_{-\mathbf{q}_2} m^{\kappa}_{-\mathbf{q}_3} m^{\lambda}_{-\mathbf{q}_4}\rangle = \langle m^{\mu}_{-\mathbf{q}_1} m^{\nu}_{-\mathbf{q}_2} m^{\kappa}_{-\mathbf{q}_3} m^{\lambda}_{-\mathbf{q}_4}\rangle \delta_{\mathbf{q}_1+\mathbf{q}_2+\mathbf{q}_3+\mathbf{q}_4,0}. \tag{B18}$$

Thus, we find

$$\left.\frac{\partial^2 F}{\partial T^{\alpha}_{\mathbf{q}_1}\partial T^{\beta}_{\mathbf{q}_2}}\right|_{\mathbf{T}=0} = \frac{\varepsilon^{\mu\sigma\alpha}\varepsilon^{\nu\rho\beta}Q^{\sigma}_{-\mathbf{q}_1}Q^{\rho}_{-\mathbf{q}_2}V_{\mathbf{q}_1}\delta_{\mathbf{q}_1+\mathbf{q}_2,0}}{N} \times\left(\delta^{\mu\nu}-\frac{V_{\mathbf{q}_2}}{NT}\langle m^{\mu}_{-\mathbf{q}_1}m^{\nu}_{-\mathbf{q}_2}\rangle\right) \tag{B19}$$

for the second derivative and

$$\begin{aligned}\left.\frac{\partial^4 F}{\partial T^{\alpha}_{\mathbf{q}_1}\partial T^{\beta}_{\mathbf{q}_2}\partial T^{\gamma}_{\mathbf{q}_3}\partial T^{\delta}_{\mathbf{q}_4}}\right|_{\mathbf{T}=0} &= \frac{\varepsilon^{\mu\sigma\alpha}\varepsilon^{\nu\rho\beta}\varepsilon^{\kappa\tau\gamma}\varepsilon^{\lambda\eta\delta}Q^{\sigma}_{-\mathbf{q}_1}Q^{\rho}_{-\mathbf{q}_2}Q^{\tau}_{-\mathbf{q}_3}Q^{\eta}_{-\mathbf{q}_4}V_{\mathbf{q}_1}V_{\mathbf{q}_2}V_{\mathbf{q}_3}V_{\mathbf{q}_4}}{N^4T^3}\\ &\times\{\langle m^{\mu}_{-\mathbf{q}_1}m^{\nu}_{-\mathbf{q}_2}\rangle\langle m^{\kappa}_{-\mathbf{q}_3}m^{\lambda}_{-\mathbf{q}_4}\rangle\delta_{\mathbf{q}_1+\mathbf{q}_2,0}\delta_{\mathbf{q}_3+\mathbf{q}_4,0}\\ &+\langle m^{\mu}_{-\mathbf{q}_1}m^{\kappa}_{-\mathbf{q}_3}\rangle\langle m^{\nu}_{-\mathbf{q}_2}m^{\lambda}_{-\mathbf{q}_4}\rangle\delta_{\mathbf{q}_1+\mathbf{q}_3,0}\delta_{\mathbf{q}_2+\mathbf{q}_4,0}\\ &+\langle m^{\mu}_{-\mathbf{q}_1}m^{\lambda}_{-\mathbf{q}_4}\rangle\langle m^{\nu}_{-\mathbf{q}_2}m^{\kappa}_{-\mathbf{q}_3}\rangle\delta_{\mathbf{q}_1+\mathbf{q}_4,0}\delta_{\mathbf{q}_2+\mathbf{q}_3,0}\\ &-\langle m^{\mu}_{-\mathbf{q}_1}m^{\nu}_{-\mathbf{q}_2}m^{\kappa}_{-\mathbf{q}_3}m^{\lambda}_{-\mathbf{q}_4}\rangle\delta_{\mathbf{q}_1+\mathbf{q}_2+\mathbf{q}_3+\mathbf{q}_4,0}\}\end{aligned} \tag{B20}$$

for the fourth. These expressions may also be applied to a gas of point charges in 2D or 3D, that is when m is a scalar field. One way to do this is by replacing $\nabla\times\mathbf{T}$ in Eq. (B2) with its z component $\varepsilon^{z\nu\lambda}\Delta^{\nu}T^{\lambda}$, with the consequence that the greek letter summations may be taken over x and y only. For the second derivative, this results in

$$\left.\frac{\partial^2 F}{\partial T^{\alpha}_{\mathbf{q}_1}\partial T^{\beta}_{\mathbf{q}_2}}\right|_{\mathbf{T}=0} = \frac{\varepsilon^{z\sigma\alpha}\varepsilon^{z\rho\beta}Q^{\sigma}_{-\mathbf{q}_1}Q^{\rho}_{\mathbf{q}_1}V_{\mathbf{q}_1}\delta_{\mathbf{q}_1+\mathbf{q}_2,0}}{N} \times\left(1-\frac{V_{\mathbf{q}_1}}{NT}\langle m_{\mathbf{q}_1}m_{-\mathbf{q}_1}\rangle\right), \tag{B21}$$

where we have applied $V_{\mathbf{q}}=V_{-\mathbf{q}}$. We recognize the paranthesis as the Fourier transform of the inverse dielectric response function $\epsilon^{-1}(\mathbf{q}_1)$ in the low density limit. Note that the factor

$$\varepsilon^{z\sigma\alpha}\varepsilon^{z\rho\beta}Q^{\sigma}_{-\mathbf{q}_1}Q^{\rho}_{\mathbf{q}_1} = Q^{\sigma}_{\mathbf{q}_1}Q^{\sigma}_{-\mathbf{q}_1}\left(1-\frac{Q^{\alpha}_{\mathbf{q}_1}Q^{\beta}_{-\mathbf{q}_1}}{Q^{\sigma}_{\mathbf{q}_1}Q^{\sigma}_{-\mathbf{q}_1}}\right) \tag{B22}$$

is a projection operator times $Q^{\sigma}_{\mathbf{q}_1}Q^{\sigma}_{-\mathbf{q}_1}\sim q^2_{1x}+q^2_{1y}$, reflecting the transversality of the twist.

To arrive at Eq. (8), we chose the twist (7) and computed the sums appearing in the expansion (B10) for both the second and fourth order term. The sum over direction is trivial, since our twist points in the x-direction. The sum over momenta is also managable, since $T^{x}_{\mathbf{q}}$ has nonzero values only for $\mathbf{q}=(0,\pm 2\pi/L)$. This sum gives two contributions in the second order term, due to the restriction $\delta_{\mathbf{q}_1+\mathbf{q}_2,0}$. The same argument results in four contributions for the three terms in Eq. (B20) being a product of two second order correlators. The term containing a fourth order correlator will give six contributions due to the restriction $\delta_{\mathbf{q}_1+\mathbf{q}_2+\mathbf{q}_3+\mathbf{q}_4,0}$.

APPENDIX C: HIGHER ORDER TERMS

Using the method described in this paper involves extrapolation to $L\to\infty$ and deciding whether or not the fourth order term in the expansion (B10) goes to zero or to a finite nonzero value. This procedure could in some cases be difficult. However, if the fourth order term had turned out to be zero in the thermodynamic limit, it would *not* necessarily mean that the second order term, the inverse dielectric response function, would have to go continuously to zero. In fact, if one were able to prove that the fourth order term is negative *or* zero, one could go on to investigate the sixth order term instead. If it then turned out that the value of the sixth order term was hard to establish, one could in principle repeat the procedure and go to higher order terms. We therefore include the sixth derivative here. To simplify calculations, we work with a twist in the x direction only:

$$\begin{aligned}\frac{\partial^6 F}{\partial T^x_{\mathbf{q}_1}\partial T^x_{\mathbf{q}_2}\partial T^x_{\mathbf{q}_3}\partial T^x_{\mathbf{q}_4}\partial T^x_{\mathbf{q}_5}\partial T^x_{\mathbf{q}_6}} &= \frac{1}{T^5}\Bigg\{120\left\langle\frac{\partial H}{\partial T^x_{\mathbf{q}_1}}\right\rangle\left\langle\frac{\partial H}{\partial T^x_{\mathbf{q}_2}}\right\rangle\left\langle\frac{\partial H}{\partial T^x_{\mathbf{q}_3}}\right\rangle\left\langle\frac{\partial H}{\partial T^x_{\mathbf{q}_4}}\right\rangle\left[\left\langle\frac{\partial H}{\partial T^x_{\mathbf{q}_5}}\right\rangle\left\langle\frac{\partial H}{\partial T^x_{\mathbf{q}_6}}\right\rangle-3\left\langle\frac{\partial H}{\partial T^x_{\mathbf{q}_5}}\frac{\partial H}{\partial T^x_{\mathbf{q}_6}}\right\rangle\right]\\ &+18\left\langle\frac{\partial H}{\partial T^x_{\mathbf{q}_1}}\frac{\partial H}{\partial T^x_{\mathbf{q}_2}}\right\rangle\left[13\left\langle\frac{\partial H}{\partial T^x_{\mathbf{q}_3}}\right\rangle\left\langle\frac{\partial H}{\partial T^x_{\mathbf{q}_4}}\right\rangle\left\langle\frac{\partial H}{\partial T^x_{\mathbf{q}_5}}\frac{\partial H}{\partial T^x_{\mathbf{q}_6}}\right\rangle-\left\langle\frac{\partial H}{\partial T^x_{\mathbf{q}_3}}\frac{\partial H}{\partial T^x_{\mathbf{q}_4}}\right\rangle\left\langle\frac{\partial H}{\partial T^x_{\mathbf{q}_5}}\frac{\partial H}{\partial T^x_{\mathbf{q}_6}}\right\rangle\right]\\ &+2\left\langle\frac{\partial H}{\partial T^x_{\mathbf{q}_1}}\frac{\partial H}{\partial T^x_{\mathbf{q}_2}}\frac{\partial H}{\partial T^x_{\mathbf{q}_3}}\right\rangle\left[5\left\langle\frac{\partial H}{\partial T^x_{\mathbf{q}_4}}\frac{\partial H}{\partial T^x_{\mathbf{q}_5}}\frac{\partial H}{\partial T^x_{\mathbf{q}_6}}\right\rangle-48\left\langle\frac{\partial H}{\partial T^x_{\mathbf{q}_4}}\right\rangle\left\langle\frac{\partial H}{\partial T^x_{\mathbf{q}_5}}\frac{\partial H}{\partial T^x_{\mathbf{q}_6}}\right\rangle+60\left\langle\frac{\partial H}{\partial T^x_{\mathbf{q}_4}}\right\rangle\left\langle\frac{\partial H}{\partial T^x_{\mathbf{q}_5}}\right\rangle\right.\\ &\left.\times\left\langle\frac{\partial H}{\partial T^x_{\mathbf{q}_6}}\right\rangle\right]+15\left\langle\frac{\partial H}{\partial T^x_{\mathbf{q}_1}}\frac{\partial H}{\partial T^x_{\mathbf{q}_2}}\frac{\partial H}{\partial T^x_{\mathbf{q}_3}}\frac{\partial H}{\partial T^x_{\mathbf{q}_4}}\right\rangle\left[\left\langle\frac{\partial H}{\partial T^x_{\mathbf{q}_5}}\frac{\partial H}{\partial T^x_{\mathbf{q}_6}}\right\rangle-2\left\langle\frac{\partial H}{\partial T^x_{\mathbf{q}_5}}\right\rangle\left\langle\frac{\partial H}{\partial T^x_{\mathbf{q}_6}}\right\rangle\right]+6\left\langle\frac{\partial H}{\partial T^x_{\mathbf{q}_1}}\right\rangle\\ &\times\left\langle\frac{\partial H}{\partial T^x_{\mathbf{q}_2}}\frac{\partial H}{\partial T^x_{\mathbf{q}_3}}\frac{\partial H}{\partial T^x_{\mathbf{q}_4}}\frac{\partial H}{\partial T^x_{\mathbf{q}_5}}\frac{\partial H}{\partial T^x_{\mathbf{q}_6}}\right\rangle-\left\langle\frac{\partial H}{\partial T^x_{\mathbf{q}_1}}\frac{\partial H}{\partial T^x_{\mathbf{q}_2}}\frac{\partial H}{\partial T^x_{\mathbf{q}_3}}\frac{\partial H}{\partial T^x_{\mathbf{q}_4}}\frac{\partial H}{\partial T^x_{\mathbf{q}_5}}\frac{\partial H}{\partial T^x_{\mathbf{q}_6}}\right\rangle\Bigg\}-\frac{12}{T^4}\frac{\partial^2 H}{\partial T^x_{\mathbf{q}_1}\partial T^x_{\mathbf{q}_2}}\Bigg\{2\left\langle\frac{\partial H}{\partial T^x_{\mathbf{q}_3}}\right\rangle\end{aligned}$$

$$\times \frac{\partial H}{\partial T^x_{\mathbf{q}_4}} \Bigg\rangle \Bigg\langle \frac{\partial H}{\partial T^x_{\mathbf{q}_5}} \frac{\partial H}{\partial T^x_{\mathbf{q}_6}} \Bigg\rangle + 2 \Bigg\langle \frac{\partial H}{\partial T^x_{\mathbf{q}_3}} \frac{\partial H}{\partial T^x_{\mathbf{q}_4}} \Bigg\rangle \Bigg\langle \frac{\partial H}{\partial T^x_{\mathbf{q}_5}} \frac{\partial H}{\partial T^x_{\mathbf{q}_6}} \Bigg\rangle + \Bigg\langle \frac{\partial H}{\partial T^x_{\mathbf{q}_3}} \Bigg\rangle \Bigg\langle \frac{\partial H}{\partial T^x_{\mathbf{q}_4}} \frac{\partial H}{\partial T^x_{\mathbf{q}_5}} \frac{\partial H}{\partial T^x_{\mathbf{q}_6}} \Bigg\rangle \Bigg\}$$

$$+ \frac{12}{T^3} \frac{\partial^2 H}{\partial T^x_{\mathbf{q}_1} \partial T^x_{\mathbf{q}_2}} \frac{\partial^2 H}{\partial T^x_{\mathbf{q}_3} \partial T^x_{\mathbf{q}_4}} \Bigg\{ \Bigg\langle \frac{\partial H}{\partial T^x_{\mathbf{q}_5}} \frac{\partial H}{\partial T^x_{\mathbf{q}_6}} \Bigg\rangle + 2 \Bigg\langle \frac{\partial H}{\partial T^x_{\mathbf{q}_5}} \Bigg\rangle \Bigg\langle \frac{\partial H}{\partial T^x_{\mathbf{q}_6}} \Bigg\rangle \Bigg\}. \tag{C1}$$

Note that we are allowed to permute the momenta $\mathbf{q}_1, \ldots, \mathbf{q}_6$, since these are summed over in the free energy expansion. Assuming vanishing odd-order correlators and imposing that m is a scalar field gives

$$\frac{\partial^6 F}{\partial T^x_{\mathbf{q}_1} \partial T^x_{\mathbf{q}_2} \partial T^x_{\mathbf{q}_3} \partial T^x_{\mathbf{q}_4} \partial T^x_{\mathbf{q}_5} \partial T^x_{\mathbf{q}_6}} = \frac{Q^y_{-\mathbf{q}_1} Q^y_{-\mathbf{q}_2} Q^y_{-\mathbf{q}_3} Q^y_{-\mathbf{q}_4} Q^y_{-\mathbf{q}_5} Q^y_{-\mathbf{q}_6} V_{\mathbf{q}_1} V_{\mathbf{q}_2} V_{\mathbf{q}_3} V_{\mathbf{q}_4}}{N^4 T^3} \Bigg\{ 12 \langle m_{-\mathbf{q}_1} m_{-\mathbf{q}_2} \rangle \Bigg[1 - \frac{2 V_{\mathbf{q}_5}}{NT} \langle m_{-\mathbf{q}_3} m_{-\mathbf{q}_4} \rangle \Bigg]$$

$$\times \delta_{\mathbf{q}_1+\mathbf{q}_2,0} \delta_{\mathbf{q}_3+\mathbf{q}_4,0} \delta_{\mathbf{q}_5+\mathbf{q}_6,0} - \frac{V_{\mathbf{q}_5} V_{\mathbf{q}_6}}{N^2 T^2} \Big[\langle m_{-\mathbf{q}_1} m_{-\mathbf{q}_2} m_{-\mathbf{q}_3} m_{-\mathbf{q}_4} m_{-\mathbf{q}_5} m_{-\mathbf{q}_6} \rangle \delta_{\mathbf{q}_1+\mathbf{q}_2+\mathbf{q}_3+\mathbf{q}_4+\mathbf{q}_5+\mathbf{q}_6,0}$$

$$- 3 \langle m_{-\mathbf{q}_1} m_{-\mathbf{q}_2} \rangle \delta_{\mathbf{q}_1+\mathbf{q}_2,0} (5 \langle m_{-\mathbf{q}_3} m_{-\mathbf{q}_4} m_{-\mathbf{q}_5} m_{-\mathbf{q}_6} \rangle \delta_{\mathbf{q}_3+\mathbf{q}_4+\mathbf{q}_5+\mathbf{q}_6,0} - 6 \langle m_{-\mathbf{q}_3} m_{-\mathbf{q}_4} \rangle$$

$$\times \langle m_{-\mathbf{q}_5} m_{-\mathbf{q}_6} \rangle \delta_{\mathbf{q}_3+\mathbf{q}_4,0} \delta_{\mathbf{q}_5+\mathbf{q}_6,0}) \Big] \Bigg\}. \tag{C2}$$

*E-mail address: kjetil.borkje@phys.ntnu.no
†E-mail address: steinar.kragset@phys.ntnu.no
‡E-mail address: asle.sudbo@phys.ntnu.no

[1] I. Affleck and J. B. Marston, Phys. Rev. B **39**, 11538 (1989).
[2] G. Baskaran and P. W. Anderson, Phys. Rev. B **37**, 580 (1988).
[3] I. Affleck, Z. Zou, T. Hsu, and P. W. Anderson, Phys. Rev. B **38**, 745 (1988); Z. Zou and P. W. Anderson, *ibid.* **37**, 627 (1988).
[4] E. Dagotto, E. Fradkin, and A. Moreo, Phys. Rev. B **38**, 2926 (1988).
[5] L. B. Ioffe and A. I. Larkin, Phys. Rev. B **39**, 8988 (1989).
[6] N. Nagaosa and P. A. Lee, Phys. Rev. B **61**, 9166 (2000).
[7] G. Mudry and E. Fradkin, Phys. Rev. B **49**, 5200 (1994); **50**, 11 409 (1994).
[8] I. Ichinose and T. Matsui, Phys. Rev. B **51**, 11 860 (1995); I. Ichinose, T. Matsui, and M. Onoda, *ibid.* **64**, 104516 (2001).
[9] D. K. K. Lee and Y. Chen, J. Phys. A **21**, 4155 (1988).
[10] T. Senthil and M. P. A. Fisher, Phys. Rev. B **62**, 7850 (2000).
[11] A. M. Polyakov, Nucl. Phys. B **120**, 429 (1977).
[12] J. M. Kosterlitz, J. Phys. C **10**, 1046 (1977).
[13] I. F. Herbut and Z. Tešanović, Phys. Rev. Lett. **76**, 4588 (1996).
[14] H. Kleinert, F. S. Nogueira, and A. Sudbø, Phys. Rev. Lett. **88**, 232001 (2002); Nucl. Phys. B **666**, 361 (2003).
[15] M. Hermele, T. Senthil, M. P. A. Fisher, P. A. Lee, N. Nagaosa, and X.-G. Wen, cond-mat/0404751 (unpublished).
[16] I. F. Herbut and B. H. Seradjeh, Phys. Rev. Lett. **91**, 171601 (2003); I. F. Herbut, B. H. Seradjeh, S. Sachdev, and G. Murthy, Phys. Rev. B **68**, 195110 (2003); M. J. Case, B. H. Seradjeh, and I. F. Herbut, Nucl. Phys. B **676**, 572 (2004).
[17] M. N. Chernodub, E.-M. Ilgenfritz, and A. Schiller, Phys. Lett. B **547**, 269 (2002); **555**, 206 (2003).
[18] S. Kragset, F. S. Nogueira, and A. Sudbø, Phys. Rev. Lett. **92**, 186403 (2004).
[19] D. R. Nelson and J. M. Kosterlitz, Phys. Rev. Lett. **39**, 1201 (1977); P. Minnhagen and G. G. Warren, Phys. Rev. B **24**, 2526 (1981).
[20] P. Minnhagen and B. J. Kim, Phys. Rev. B **67**, 172509 (2003).
[21] A. M. Ferrenberg and R. H. Swendsen, Phys. Rev. Lett. **61**, 2635 (1988); , **63**, 1195 (1989).
[22] J. M. Kosterlitz and D. J. Thouless, J. Phys. C **6**, 1181 (1973).
[23] H. A. Fertig and J. P. Straley, Phys. Rev. B **66**, 201402(R) (2002); H. A. Fertig, Phys. Rev. Lett. **89**, 035703 (2002).
[24] P. Olsson (private communication).
[25] J. M. Kosterlitz, J. Phys. C **10**, 3753 (1977).
[26] P. Minnhagen, Phys. Rev. B **32**, 3088 (1985).

Paper III

First order phase transition in a gauge theory of $S = 1/2$ quantum antiferromagnets

cond-mat/0609336, (submitted to Physical Review Letters)

First-order phase transition in a gauge theory of $S = 1/2$ quantum antiferromagnets in the deep easy-plane limit

S. Kragset,[1] E. Smørgrav,[1] J. Hove,[1] F. S. Nogueira,[2] and A. Sudbø[1,3]

[1] *Department of Physics, Norwegian University of Science and Technology, N-7491 Trondheim, Norway*
[2] *Institut für Theoretische Physik, Freie Universität Berlin, Arnimallee 14, D-14195 Berlin, Germany*
[3] *Centre for Advanced Study at the Norwegian Academy of Science and Letters, Drammensveien 78, N-0271 Oslo, Norway*

We perform large-scale Monte Carlo simulations on an effective gauge theory for a deep easy-plane antiferromagnet, including a Berry phase term that projects out the $S = 1/2$ sector. Without aBerry phase term, the model exhibits a phase transition in the $3DXY$ universality class associated with proliferation of gauge-charge neutral $U(1)$ vortices. The instantons that eliminate the phase transition in the gauge-charged sector are suppressed by the Berry phases. The result is a *first-order* phase transition.

PACS numbers: 73.43.Nq, 75.10.Jm, 11.15.Ha

The Landau–Ginzburg–Wilson (LGW) theory for phase transitions has been an immensely successful paradigm of physics for the last 50 years. It is one of the cornerstones of statistical and condensed matter physics, providing deep insight into phase transitions [1]. The standard example is the well-known paramagnetic-ferromagnetic phase transition. Recently, examples of phase transitions that do not fit into the LGW paradigm have been discussed [2–4]. These are specific *continuous* quantum phase transitions from a Néel state with conventional antiferromagnetic order into a paramagnetic valence-bond solid (VBS) state [5]. In the Néel state, an $SU(2)$ symmetry is broken, while in the valence-bond solid translational symmetry is broken. Hence, the phase transition separating them is an order–order phase transition with two distinct order parameters associated with it. Continuous order–order phase transitions would not easily fall within the LGW paradigm, where this type of transitions are typically first-order.

An attempt to provide proof of evidence for these ideas has recently been put forth [2]. It involves a deformation of the Heisenberg model into an easy-plane quantum antiferromagnet. The latter can be studied through the deep easy-plane version of an effective lattice gauge theory for a quantum antiferromagnet proposed in Ref. [6]. For $S = 1/2$ it has the action

$$S[\theta, \mathbf{A}; \eta] = \sum_j \Bigg[\sum_{\mu=1}^{3} \Bigg(\beta \sum_{a=1}^{2} [1 - \cos(\Delta_\mu \theta_{ja} - A_{j\mu})] + \kappa \{1 - \cos[(\mathbf{\Delta} \times \mathbf{A}_j)_\mu]\} \Bigg) + i\eta_j A_{j\tau} \Bigg]. \quad (1)$$

The first term is reminiscent of the CP^1 representation of the non-linear σ model description of a quantum antiferromagnet. There the orientation of the Néel order parameter is represented by $\mathbf{n}_j = z^*_{ja}\sigma_{ab}z_{jb}$. The deep easy-plane limit together with the constraint $|z_1|^2 + |z_2|^2 = 1$ allows us to write $z_{ja} = e^{i\theta_{ja}}/\sqrt{2}$. $\mathbf{A}$ is a compact gauge field which here is doing more than just being an auxiliary field, like in the case of the CP^1 model. It determines also the Berry phase for the above model. The index τ corresponds to $\mu = 3$, and the staggering factor is given by $\eta_j = \pm 1$ and is independent of imaginary time. Note that the present gauge field is a function of the space-time coordinates, in contrast to the usual Berry gauge potential appearing in $SU(2)$ spin models [4], which is a functional of the spin field.

Compactness of the gauge field gives rise to instanton configurations [7] which are known to remove a second order phase transition in a corresponding model with only one complex scalar matter field and no Berry phase [8]. Without the Berry phase and with two matter fields present, it is known that one can rewrite the theory in terms of a linear combination of phase fields which does not couple to the gauge field, and one which does [9, 10]. Thus, regardless of whether the gauge field is compact or not, the charge-neutral linear combination of phase fields features topological objects which proliferate in a $3DXY$ phase transition [10]. The remaining charged sector will behave as for the one-component case [10, 11].

Recently, it has been argued that the Berry phase, which is crucial to describe the phase inside the paramagnetic phase [2, 3], suppresses the instantons at the critical point. In a phase transition from a Néel to a VBS state, the spinons are confined at either of these phases. Irrelevance of instantons at the critical point leads to the so called "deconfined quantum criticality" [2]. Here we will investigate this point by monitoring the phase transitions in the model (1) in the presence and absence of a Berry phase term. As already mentioned, without such a term we expect a phase transition in the $3DXY$ universality class. The latter is driven by a vortex-loop proliferation in the neutral sector. In the presence of a Berry phase term, a phase transition is also expected in the charged sector. Since the bare phase stiffnesses of the two matter fields are the same, the proliferation temperature of the neutral and charged cases will also be the

same. The result will be shown to be a single first-order phase transition.

The deconfined quantum criticality scenario implies that the critical point is governed by an easy-plane system action featuring a non-compact gauge field, i.e.,

$$S[\theta,\mathbf{A}] = \sum_i \sum_{\mu=1}^{3} \Big\{ \beta \sum_{a=1}^{2} [1-\cos(\Delta_\mu \theta_{ia} - A_{i\mu})] + \frac{\kappa}{2} (\mathbf{\Delta} \times \mathbf{A}_i)_\mu^2 \Big\}. \quad (2)$$

This model with unequal bare phase stiffnesses has been studied in great detail [10]. It features two distinct second-order phase transitions, one belonging to the $3DXY$ universality class and another one corresponding to the so-called inverted $3DXY$ transition [12]. In the limit where the bare phase stiffnesses are equal, clear signals of non-$3DXY$ behavior are seen [10, 13]. In Ref. 13, strong indications of a first-order phase transition in a loop-gas representation of the non-compact model Eq. (2), were found. We will consider both Eqs. (1) and (2) in detailed Monte Carlo (MC) simulations.

For performing MC simulations on the model with a Berry phase term, it is convenient to introduce a dual representation of the model Eq. (1). In such a representation the action is real, given by [4]

$$S[\mathbf{h}^{(a)},s;f] = \frac{1}{2} \sum_i \Big\{ \frac{1}{\beta} [(\mathbf{\Delta} \times \mathbf{h}_i^{(1)})^2 + (\mathbf{\Delta} \times \mathbf{h}_i^{(2)})^2] + \frac{1}{\kappa} (\mathbf{h}_i^{(1)} + \mathbf{h}_i^{(2)} + \mathbf{f}_i + \mathbf{\Delta} s_i)^2 \Big\}. \quad (3)$$

Here, $\mathbf{h}^{(a)}$ are integer-valued dual gauge fields, and $\varepsilon_{\mu\lambda\nu}\Delta^\nu f_i^\lambda = \delta_{\mu\tau}\eta_i$. Note that we would obtain Eq. (3) both for Eqs. (1) and (2), with $f_i = 0$ for Eq. (2). For Eq. (1) with compact $A_{i\mu}$, s_i is integer-valued. For Eq. (2) with a non-compact $A_{i\mu}$, s_i is real-valued. Therefore in the former case s_i can be gauged away since the $\mathbf{h}^{(a)}$-fields are integer-valued. We have chosen a gauge where $s_i = 0$. The MC computations were performed using Eqs. (2) and (3). For both Eqs. (2) and (3), we have used $\kappa = \beta$. We have used the standard Metropolis algorithm with periodic boundary conditions on a cubic lattice of size $L \times L \times L$. For Eq. (3) we have used $L = 4, 8, 12, 16, 20, 24, 32, 36, 48, 60, 64, 72, 80, 96, 120$, while for Eq. (2) we have used $L = 48, 64, 80, 96, 112, 120$. A large number of sweeps is required in order to get adequate statistics in the histograms (see below) for the largest system sizes. Firstly, we have computed the second moment of the action $M_2 \equiv \langle (S - \langle S \rangle)^2 \rangle$ for the model with and without a Berry phase term. Secondly, we have focused on a number of quantities that provide information on the character of the phase transition associated with the specific heat anomaly. The first of these quantities is the third moment of the action, $M_3 \equiv \langle (S - \langle S \rangle)^3 \rangle$. At a second-order phase transition this quantity should scale as follows. The peak-to-peak height scales as $L^{(1+\alpha)/\nu}$, whereas the width between the peaks scales as $L^{-1/\nu}$ [14]. At a first-order phase transition, these quantities scale as L^6 and $L^{-1/\nu}$, respectively [15]. We also study the probability distribution $P(S,L)$ of the action S for various system sizes. At a first-order phase transition, $P(S,L)$ will exhibit a double-peak structure associated with the two coexisting phases.

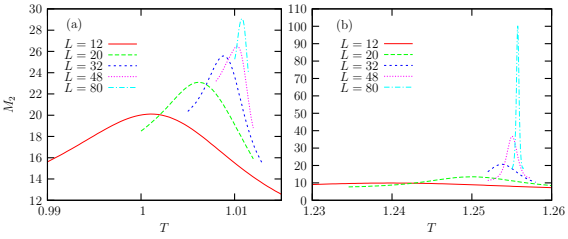

FIG. 1: (Color online) Specific heat M_2 of Eq. (3) for various system sizes. Panel (a): Without Berry phase term. The peak develops into a singularity of the $3DXY$ type. Panel (b): With Berry phase term. The peak develops into a δ-function singularity with a peak scaling as L^3, consistent with a first-order phase transition. Note the symmetry and asymmetry of the peaks in the right and left panels, respectively. This is to be expected, since the peaks in the right panel originate with the superposition of a $3DXY$ peak and an inverted $3DXY$ peak.

The specific heat M_2 is shown in Fig. 1. Panel (a) shows the anomaly for the model Eq. (3) with no Berry-phase term, i.e., $\mathbf{\Delta} \times \mathbf{f} = (0,0,\eta) = 0$. The anomaly has the characteristic asymmetric shape of the $3DXY$ model. In this case, there are no Berry phases to suppress the instantons of the compact gauge-field $\mathbf{A}$ at the critical point. Hence, the charged sector does not feature critical fluctuations that can interfere with those of the neutral sector. When the Berry phase field $\mathbf{f}$ is included, the specific heat is notably more symmetric and the anomaly develops into a δ-function peak, consistent with a first-order phase transition. This is shown in panel (b).

To investigate more precisely the character of the phase transition when a Berry phase term is present, we have performed finite-size scaling (FSS) of the third moment of the action, M_3 [14]. The results are shown in Fig. 2, panel (a). It is seen that for small and intermediate system sizes, the height increases with L in a manner which might appear consistent with that of a second-order phase transition. However, the quality of the scaling is not satisfactory, since a clear curvature in the scaling plots is seen (red data points). As system sizes increase we see a gradual increase in the apparent value of $(1+\alpha)/\nu$, until for large system sizes, we clearly have $M_3 \sim L^6$, consistent with a first-order phase transition [15].

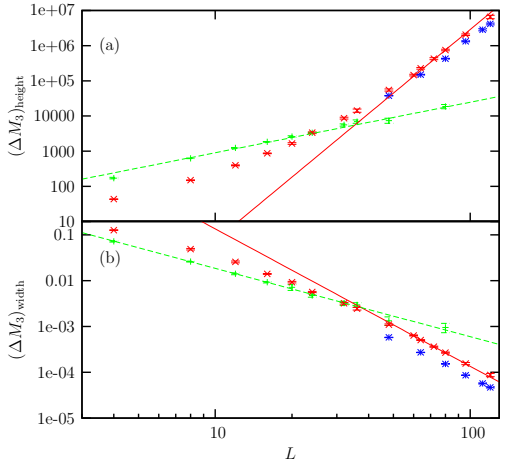

FIG. 2: (Color online) Scaling of the height [panel (a)] and width [panel (b)] of M_3 of the action in Eqs. (2) and (3). The lines in panel (a) represent $L^{1.43}$ and L^6. The former is the $3DXY$ result. The lines in panel (b) represent $L^{-1.49}$ and L^{-3}. The former is the $3DXY$ result. For large system sizes, the height and width scale in manner consistent with a first-order phase transition. Also shown are results for Eq. (3) with no Berry phase term $\mathbf{f} = 0$ (green symbols). These results follow the $3DXY$ scaling lines. The red symbols are the results for Eq. (3) while the blue symbols are results for Eq. (2).

Panel (b) of Fig. 2 shows the scaling of the width of M_3. Again, the line with the smallest negative slope is the line one would obtain for the $3DXY$ model, while the line with the most negative slope is $\sim L^{-3}$, characteristic of a first-order phase transition. Again we obtain apparent scaling, with a crossover regime at intermediate length scales into a regime where the width scales as it would in a first-order phase transition [15]. The results of Fig. 2 provide further support to the notion that the phase transition in the model with a compact gauge field and a Berry phase term is a first-order phase transition.

To investigate this further, we have computed the probability distribution $P(S, L)$ for various system sizes. The results are shown in Fig. 3. Panel (a) shows results for Eq. (1) in the representation Eq. (3). Panel (b) shows results for Eq. (2). The Ferrenberg–Swendsen algorithm has been used to reweight the histograms [16]. For $L \leq 48$, we essentially have not been able to resolve a double peak structure at all, showing that the phase transitions in the models Eqs. (1) and (2) are weakly first-order. We have located the transition temperature from the peak structures in the specific heat and M_3, and performed long simulations at this temperature for each L. For the largest systems, $L = 96, 120$, up to $120 \cdot 10^6$ sweeps over the lattice were done. A clear double-peak structure in $P(S, L)$ is seen to develop for system sizes $L > 60$. The fact that such large system sizes are required to bring out the double-peak structure, implies that this phase transition is weakly first-order.

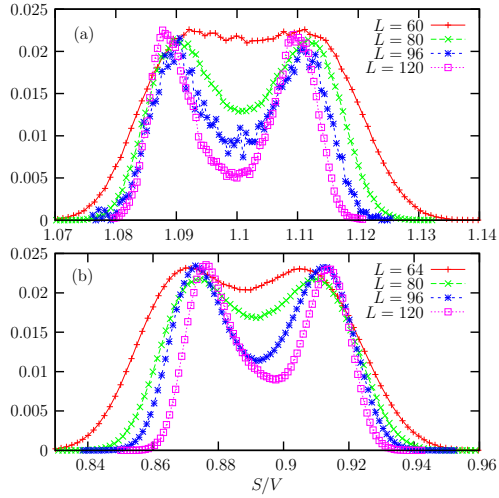

FIG. 3: (Color online) Histograms for the probability distribution $P(S, L)$ as a function of S/L^3 for various system sizes L. (a): results for Eq. (1) in the representation Eq. (3). (b): results Eq. (2). A double peak structure develops with the latent heat per unit volume approaching a finite constant as L is increased. This is a hallmark of a first-order phase transition. For the largest systems, up to $120 \cdot 10^6$ sweeps over the lattice were performed. A total of approximately 500000 CPU hours were used to obtain these results.

We also perform FSS of the height of the peak between the two degenerate minima in the free energy $-\ln[P(S, L)]$. This height should scale as L^2 in a first-order phase transition, since it represents the energy of an area which separates two coexisting phases [17]. The results are shown in panel (a) of Fig. 4. For large enough systems, the height clearly approaches the dotted line $\sim L^2$, as in a first-order transition. This is corroborated by extracting the latent heat per unit volume in the transition, shown in the lower panel of Fig. 4. It approaches a nonzero constant as L is increased, as it should in a first-order phase transition.

Further insight into the nature of the first-order phase transition can be obtained by means of the renormalization group (RG). In the field theory Lagrangian the interaction of the easy-plane system reads $\mathcal{L}_{\rm int} = u_0(|z_1|^2 + |z_2|^2)^2/2 + v_0|z_1|^2|z_2|^2 = u_0(|z_1|^4 + |z_2|^4)/2 + w_0|z_1|^2|z_2|^2$, where $w_0 = u_0 + v_0$. Consider a generalized situation where the complex fields each have $N/2$ components. A similarly generalized Ginzburg–Landau (GL) theory for superconductors [18] shows that a second-order phase transition occurs only if N is greater than a certain critical value. Thus, we consider the renormalized dimen-

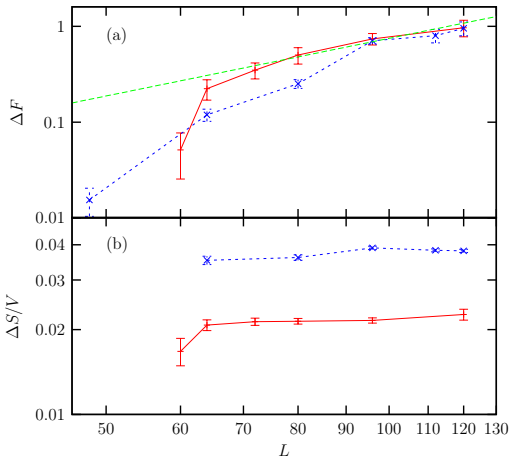

FIG. 4: (Color online) Panel (a) shows the scaling of the height ΔF of the peak between the two minima in $-\ln P(S,L)$ both for Eqs. (3) (red curve) and (2) (blue curve). Dotted line is the line $\sim L^2$. The height scales as $\Delta F \sim L^{d-1}$. This is a hallmark of a first-order phase transition. Panel (b) shows latent heat per unit volume $\Delta S/V$ as a function of L. The upper (blue) curve is from Eq. (2), the lower (red) curve is from Eq. (3). $\Delta S/V$ approaches a nonzero value as L is increased.

sionless couplings in $d = 4 - \varepsilon$ dimensions, $g = u\mu^{-\varepsilon}$, $h = w\mu^{-\varepsilon}$, and f, where f is the dimensionless gauge coupling and μ is an arbitrary mass scale. The β functions at one-loop order are [19] $\beta_g = -\varepsilon g - 6gf + (N+8)g^2/2 + 2Nh^2 + 6f^2$, $\beta_h = -\varepsilon h - 6hf + 3(N+2)gh + 6f^2$, and $\beta_f = -\varepsilon f + Nf^2/3$. For all values of N no fixed points such that $h = 0$ and $f = 3\varepsilon/N$ exist. For $N \geq 2$ and $f = 0$ there are two fixed points with $h \neq 0$, the infrared stable one corresponding to $h > 0$. Two fixed points with $f = 3\varepsilon/N$ and $h < 0$ are found for $N \geq 300$, one of which is infrared stable while the other one is unstable and associated with multicritical behavior. In the GL theory, the existence of a critical value of N above which an infrared stable fixed point is found reflects the strong-coupling behavior for $N = 2$, though being unable to reproduce it: actually it turns out that the phase transition for $N = 2$ is second-order in the type II regime [12], while a first-order phase transition occurs in the type I regime, thus establishing the existence of a tricritical point in the phase diagram [20, 21]. The same may occur here, which would apparently contradict the results of the MC simulations; see also Ref. [13] for another simulation in a closely related model which also leads to a first-order phase transition. However, it should be emphasized that the present simulation is made in the *deep* easy-plane limit, i.e., the limit where $|z_1|^2 - |z_2|^2 \approx 0$ at the core of the meron vortices. This limit is not assumed in the RG analysis. In order to see if the large N result really reflects the actual strong-coupling behavior of the $N = 2$ theory, a nonperturbative approach is needed. MC simulations of the type done in Ref. [21] is a promising alternative.

This work was supported by the Research Council of Norway, Grant Nos. 158518/431, 158547/431, 167498/V30 (STORFORSK), and 167498/V30 (NANOMAT), and the Norwegian High-Performance Computing Consortium (NOTUR).

[1] K. G. Wilson and J. B. Kogut, Phys. Rep. **12** C, 75 (1974).
[2] T. Senthil, A. Vishwanath, L. Balents, S. Sachdev, and M. P. A. Fisher, Science, **303**, 1490 (2004).
[3] T. Senthil, L. Balents, S.Sachdev, A. Vishwanath, and M. P. A. Fisher, Phys. Rev. **B 70**, 144407 (2004).
[4] S. Sachdev, in: "Quantum magnetism", U. Schollwock, J. Richter, D. J. J. Farnell and R. A. Bishop, eds., Lecture Notes in Physics (Springer, Berlin 2004).
[5] N. Read and S. Sachdev, Phys. Rev. Lett., **62**, 1694 (1989); Phys. Rev. B **42**, 4568 (1990).
[6] S. Sachdev and R. Jalabert, Mod. Phys. Lett., **B 4**, 1043 (1990).
[7] A. M. Polyakov, Nucl. Phys. B **120**, 429 (1977).
[8] E. Fradkin and S. H. Shenker, Phys. Rev. D **19**, 3682 (1979).
[9] E. Babaev, Phys. Rev. Lett. **89** (2002) 067001; Nucl. Phys. B **686** (2004) 397.
[10] J. Smiseth, E. Smørgrav, and A. Sudbø, Phys. Rev. Lett. **93**, 077002 (2004); E. Smørgrav, E. Babaev, J. Smiseth, and A. Sudbø, Phys. Rev. Lett. **95**, 135301 (2005); E. Smørgrav, J. Smiseth, E. Babaev, and A. Sudbø, Phys. Rev. Lett. **94**, 096401 (2005); J. Smiseth, E. Smørgrav, E. Babaev, and A. Sudbø, Phys. Rev. **B 71**, 214509 (2005).
[11] M. B. Einhorn and R. Savit, Phys. Rev. **D 19**, 1198 (1979).
[12] C. Dasgupta and B. I. Halperin, Phys. Rev. Lett. **47**, 1556 (1981).
[13] A. B. Kuklov, N. V. Prokof'ev, B. V. Svistunov, and M. Troyer, Ann. Phys. (N.Y.) **321**, 1602 (2006); O. I. Motrunich and A. Vishwanath, Phys. Rev. B **70**, 075104 (2004).
[14] A. Sudbø, E. Smørgrav, J. Smiseth, F. S. Nogueira, and J. Hove, Phys. Rev. Lett. **89**, 226403 (2002); J. Smiseth, E. Smørgrav, F. S. Nogueira, J. Hove, and A. Sudbø, Phys. Rev. B **67**, 205104 (2003).
[15] M. E. Fisher and A. N. Berker, Phys. Rev. B **26**, 2507 (1982); J. L. Cardy and P. Nightingale, Phys. Rev. B **27**, 4256 (1983).
[16] A. M. Ferrenberg and R. H. Swendsen, Phys. Rev. Lett., **61**, 2635 (1988); *ibid* **63**, 1195 (1989).
[17] J. Lee and J. M. Kosterlitz, Phys. Rev. Lett. **65**, 137 (1990).
[18] B. I. Halperin, T. C. Lubensky, and S.-K. Ma, Phys. Rev. Lett., **32**, 292 (1974).
[19] F. S. Nogueira, S. Kragset, and A. Sudbø, in preparation.
[20] H. Kleinert, Lett. Nuovo Cimento **35**, 405 (1982).
[21] S. Mo, J. Hove, and A. Sudbø, Phys. Rev. B **65**, 104501 (2002).

Paper IV

Thermal fluctuations of vortex Matter in trapped Bose condensates

cond-mat/0604416, (accepted for publication in Physical Review Letters)

Thermal Fluctuations of Vortex Matter in Trapped Bose Condensates

S. Kragset[1], E. Babaev[2,1], and A. Sudbø[1]
[1] *Department of Physics, Norwegian University of Science and Technology, N-7491 Trondheim, Norway*
[2] *Laboratory of Atomic and Solid State Physics, Cornell University, Ithaca, NY 14853-2501, USA*

We perform Monte Carlo studies of vortices in three dimensions in a cylindrical confinement, with uniform and nonuniform density. The former is relevant to rotating ^{4}He, the latter is relevant to a rotating trapped Bose condensate. In the former case we find dominant angular thermal vortex fluctuations close to the cylinder wall. For the latter case, a novel effect is that at low temperatures the vortex solid close to the center of the trap crosses directly over to a tension-less vortex tangle near the edge of the trap. At higher temperatures an intermediate tensionful vortex liquid located between the vortex solid and the vortex tangle, may exist.

Topological vortex excitations are hallmarks of quantum ordered states such as superconductors and superfluids. Vortices are important at vastly different length scales ranging from the dynamics of neutron stars to transport properties in superconductors and rotational response of ultracold atomic gases in optical traps [1, 2]. Particularly rich physics is associated with various orderings of quantum vortices, and the transitions between them. In certain systems, even numerous aggregate states of vortex matter are possible [3]. The simplest, yet extremely important, temperature-induced phase transition in vortex matter in a one-component superconductor or superfluid is the one from an ordered vortex line lattice (VLL) to a disordered vortex liquid (VL) state. This has been a subject of intense research in the context of high-T_c superconductivity.

Remarkable progress has recently been made in the physics of vortices in Bose-Einstein condensates (BEC) of ultra-cold atoms [1, 2]. These systems are extremely clean and have physical parameters controllable in a wide range. This has led to many suggestions for testing a number of general physical concepts in BECs. Since individual vortices, as well as their ordering patterns, can be resolved in ultra-cold gases [1, 2], a natural question arises if in these systems a thermally induced phase transition from VLL to VL can be observed, and if it can shed more light on fundamental properties of the VL states in quantum fluids in general. Detailed theoretical studies of a model uniform system, with density corresponding to the values attainable in the center of a trap, indicate that in present experiments rotation is too slow and/or particle numbers are too high to obtain a VLL melting if the approximation of a uniform system holds [4]. We also mention studies of quantum VLL melting in a one dimensional optical lattice [5]. In a harmonic trap, the condensate density will gradually be depleted from the center of the trap towards its edge. This suggests that thermal fluctuation effects will be enhanced close to the edges. We thus focus on investigating possible crossover states of vortex matter in a spatially inhomogeneous system such as a trapped BEC.

Melting of vortex lines in a bosonic condensate can be modeled by the uniformly frustrated lattice 3D XY model (see e.g. [6–8]). We study a system which takes into account the presence of a harmonic trap by using the Hamiltonian

$$H = -\sum_{\langle ij \rangle} P_{ij} \cos(\theta_j - \theta_i - A_{ij}), \qquad (1)$$

where θ_i is the phase of the condensate wave function at position i. The factor $P_{ij} \equiv P(r_{ij}) = 1-(r_{ij}/R)^2$ if $r_{ij} \leq R$, where R is the cloud size and r_{ij} is the radial distance from the cloud center. For $r_{ij} > R$ we set $P_{ij} = 0$. We account for circulation by introducing the potential $A_{ij} = \int_i^j d\mathbf{l} \cdot \mathbf{A}$. Here, $\nabla \times \mathbf{A} = (0, 0, 2\pi f)$, and f is the number of rotation-induced vortices per plaquette in the xy-plane.

We perform Monte Carlo (MC) simulations on Eq. (1) with the Metropolis algorithm. We have considered cubic numerical grids of size L^3, with $L = 36, 72$, and along the z-direction we impose periodic boundary conditions to model an elongated system. The filling fraction is $f = 1/36$, and temperatures $T \in (0.30, 3.0)$ [9]. The temperature at which the Bose condensation takes place at zero rotation in a bulk system, is given by $T = 2.2$ in our units. We note that a rapidly rotating system should be better described by the Lowest Landau Level (LLL) approximation [10], characterized for instance by the fact that the intervortex separation is comparable to the vortex-core size. However, several experiments on elongated systems are clearly outside the LLL regime. For instance, in Ref. [2], the inter-vortex separation is given as $5.0\mu m$, while the healing length (vortex-core radius ξ) is $0.2\mu m$. A parameter estimating the validity of the LLL approximation is the ratio λ of the interaction energy scale to the level spacing of the transverse harmonic confinement [10], $\lambda = 4\pi\hbar^2 a_s n/(M\hbar\omega_\perp)$, where a_s is the s-wave scattering length, M is the particle mass, and $\omega_\perp$ is the trap frequency. The LLL approximation requires $\lambda \ll 1$, while the parameters of Ref. [2] correspond to at least $\lambda \in 1 - 100$. Under such conditions, we expect Eq. (1) to be adequate. (See also caption of Fig. 3).

In the problem of vortex matter in a trap we encounter two specific circumstances, namely a finite-size situation and an inhomogeneous density profile. We begin by examining the consequences of finite size, by studying the system in a cylindrical container *with a uniform* P_{ij}. Such a situation is indeed relevant for the physics of liquid ^{4}He. Vortex orderings in such a geometry at zero temperature were studied in [11], however the VLL melting for this case was addressed only for a planar geometry (see e.g. [12]). Since the melting process in three dimensional vortex matter is very different from that in two dimensions due to the importance of vortex line bending, this problem warrants careful consideration.

Fig. 1 shows the results of simulations of vortex matter in a cylindrical container with $P_{ij} = 1, r_{ij} \leq R$. At low temperatures, the simulations reproduce orderings with circular distortions of VLL near the container wall, as predicted for ^{4}He in a zero-temperature treatment of the problem [11]. For a large number of vortices the system reacquires the hexagonal lattice symmetry away from the wall, see Fig. 1 (lower panel). Increasing the temperature in the case of small number of vortices (upper panel of Fig. 1) the dominant vortex fluctuations are associated with angular displacements, while radially the vortex density remains ordered. For a larger number of vortices (lower panel of Fig. 1) we find dominance of angular fluctuations only for the vortices situated close to container wall, while the center of the system does not display this phenomenon. The crossover to a uniformly molten vortex system occurs in both cases only at a higher temperature. The two-step thermal crossover in the vortex pattern we find is analogous to that in two dimensions where vortices are point-like objects (see e.g. [12]). There is, however, a principal difference in our case, since in three dimensions the VLL melting is accompanied by significant vortex bending fluctuations.

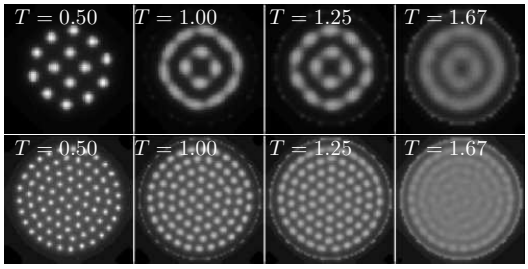

FIG. 1: xy positions of vortices in a cylindrical container integrated over z-direction, and averaged over every tenth of a total of $5 \cdot 10^5$ MC sweeps. Top and bottom rows have $L = 36$ and $L = 72$, respectively. At $T = 0.5, 1.0$, we discern circular ordering close to the cylinder wall combined with a hexagonally ordered state closer to the center. At $T = 1.25, 1.67$ we observe dominance of angular fluctuations closest to the edge.

Let us now turn to the case of a harmonic trap (Eq. 1). In a uniform and infinite system, the fluctuations can cause either VLL melting via a first-order phase transition or a second order transition associated with a thermally induced proliferation of closed vortex loops near the critical temperature where the vortices loose their line-tension [8, 13]. In a finite-size inhomogeneous system, the situation is different. A density gradient in a trap may effectively be viewed as a temperature gradient in a uniform system. It is clear that for low, but finite, temperatures there will be a finite area near the edge of the cloud which effectively would be at a high enough temperature to feature an annulus of tension-less tangle of vortices. This is a phase where the vortex-line tension (free energy per unit length) has vanished through the proliferation of vortex loops [8]. *The boundary where this tangle sets in, marks the true boundary of the BEC.* An issue to be adressed is whether we encounter an appreciable VL (i.e. tensionful but disordered vortex state) layer between the tension-less vortex tangle and the VLL.

Fig. 2 shows snapshots of vortex configurations in the model Eq. 1 generated by MC simulations at $T = 0.5$ and $T = 1.0$. For better visualization we choose the vortex radius to be 0.4 of the grid spacing so it should *not* be associated with the core size. The sharp bends at short length scales result from the presence of a numerical grid. Nonetheless, this model has proved to be accurate for describing vortex fluctuations at scales larger than the grid spacing [6–8].

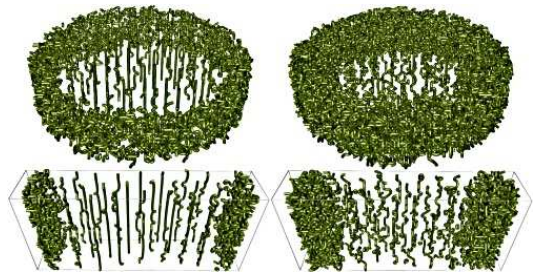

FIG. 2: (Color online) Snapshots of vortex configurations in a rotating trapped BEC at $T = 0.5$ (left figures) and at $T = 1.0$ (right figures). The top row shows a selection of 16 out of 72 layers in z direction. The bottom row shows smaller selections in the xy plane, but 32 out of 72 layers in z direction. Fluctuations are minimal in the trap center, and increase towards the edge of the trap. A distinct front separating regions of ordered and disordered vortices is easily identified.

We next locate the vortex liquid layer between the ordered vortex state and the tension-less vortex tangle closest to the edge of the trap. To this end, we take snapshots of vortex matter at different temperatures, in each case integrating over the z-direction. In a resulting image, straight vortex lines will be seen as bright spots while bent vortices will be seen as smeared out spots. This may be related to experiments, where at least for

non-equilibrated vortex systems the z-integration renders vortices essentially indistinguishable [14, 15]. The results are given in the upper row of Fig. 3 for different temperatures. There we can identify regions of rather straight and ordered vortex lines and a smeared region. To obtain further insight into the vortex matter in this case, we also perform a *thermal averaging* as in Fig. 1. This is shown in the second and third rows in Fig. 3. By averaging over different number of snapshots we identify a well-defined boundary between the ordered and disordered regions. Indeed, in a finite system, averaging will eventually produce a complete smearing even in the center of the trap. We observe signatures of this effect in the clear differences between the third picture in second and third row of Fig. 3, where averaging was made over 10^5 and $5 \cdot 10^5$ MC sweeps, respectively. Thus, the time scale of the fluctuations in the ordered regions are dramatically larger than those related to the fluctuations in the disordered regions.

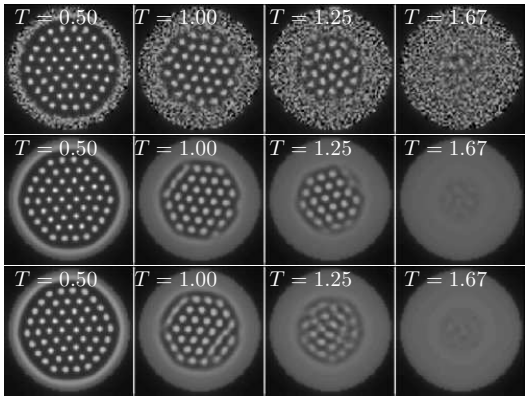

FIG. 3: xy-positions of vortices in a trapped BEC integrated over z-direction. Top row are snapshots, while middle and bottom rows are averages of 10^5 and $5 \cdot 10^5$ MC sweeps, respectively. Every tenth configuration has been sampled. This provides information on the stability of the ordered region and the evolution of the disordered region as T varies. Intervortex distance $2r_0 = 2\sqrt{\hbar/M\Omega}$ and healing length $\xi = \hbar/\sqrt{2Mg_{2D}n} \leq ca/2$, where a is lattice constant and c is a constant of order, but less than, unity. Hence, $2\hbar\Omega/g_{2D}n \leq c^2/9$, which according to Coddington *et al.* [1] validates our approach.

We next investigate the character of the vortex state in the disordered region. It is known that in the VL the helicity modulus, or equivalently the superfluid density, is zero in any direction [7, 8]. Monitoring of the helicity modulus could be employed to identify a region of a possible tensionful VL in the above pictures, as explained below. In a trapped system the global helicity modulus Υ_z [8] has no rigorous meaning, due to the non-uniform P_{ij}. However, we introduce a modified helicity modulus in z direction, defined in a selected region between two cylinders of radii R_1 and R_2. We do so by applying a twist

$$\mathbf{\Delta}(r_{ij}) \equiv \mathbf{\Delta}_{ij} = \begin{cases} \Delta\hat{\mathbf{z}} & \text{if } R_1 \leq r_{ij} < R_2, \\ 0 & \text{otherwise,} \end{cases} \tag{2}$$

to the model Eq. 1 and defining the modified helicity modulus as follows,

$$\tilde{\Upsilon}_z(R_1, R_2) \equiv \frac{1}{N'} \left\langle {\sum}' P_{ij} \cos(\theta_j - \theta_i - A_{ij}) \right\rangle - \frac{1}{TN'} \left\langle {\sum}' \left[P_{ij} \sin(\theta_j - \theta_i - A_{ij}) \right]^2 \right\rangle . \tag{3}$$

Here, $\sum'$ is over all links where $\mathbf{\Delta}_{ij}$ is nonzero (depending on R_1 and R_2) and N' is the number of these links.

In a uniform extended system the proliferation of vortex loops happens via a second order phase transition [8]. When loops proliferate, the condensate is destroyed. The temperature of vortex-loop proliferation decreases with increasing rotation (see Fig. 12 in [8]). Alternatively, the destruction of the phase-coherence along the z-axis is caused by destruction of the lattice order via a first order transition. This scenario, if it is realized in a trapped system, should be manifest in the *shape* of the helicity modulus as the transition is approached, in that it should be significantly different from the case without rotation. Namely, one should see a *remnant of a first order phase transition* with a near-discontinuity in the helicity modulus, rather than the continuous variation characterizing a second order transition driven by a proliferation of vortex loops. If one were to observe no appreciable difference in the temperature dependence of the helicity with and without rotation, one would conclude that the demarcation line seen in the images separates an ordered region from tension-less vortex tangle, with no discernible VL region. This scenario would imply a well defined and regular structure of the boundary of the VLL.

The results for $\tilde{\Upsilon}_z(R_1, R_2)$ are shown in Fig. 4. These measurements indeed show that the presence of a rotation significantly reduces the temperature at which $\tilde{\Upsilon}_z$ vanishes. This reduction relative to the case of no rotation decreases with increasing R_1, R_2. That is, panel (d) is similar to panel (c) (no trap), whereas in panel (g) there is little difference between $\tilde{\Upsilon}_z(R_1, R_2)$ with and without rotation. Thus, for the latter case the presence of vortices essentially does not influence $\tilde{\Upsilon}_z$, and the destruction of superfluid density is driven by the proliferation of vortex loops. Panel (g) is connected to the three leftmost panels in Fig. 3 in the following sense. The distinct demarcation line in these leftmost images separates a vortex solid from a tension-less vortex tangle with no visible tensionful VL region. This is consistent with the experiments showing a very regular edge structure for systems with large number of vortices [1, 2]. Note also

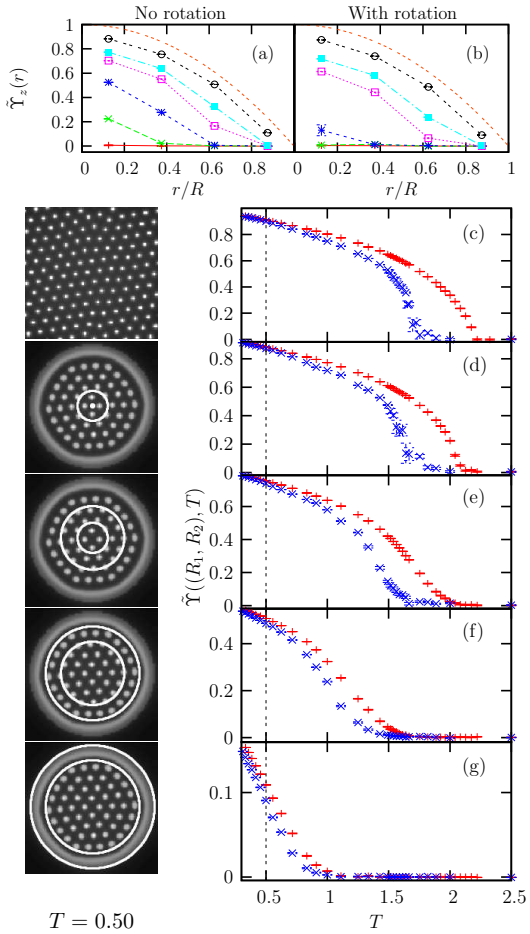

FIG. 4: Results for $\tilde{\Upsilon}_z(R_1, R_2)$. The two top panels show thermal depletion of the superfluid density in the model Eq. 1 (r is the distance from the center of the trap) at the temperatures $T = 2.50$ (the lowermost curve), $T = 2.00$, $T = 1.67$, $T = 1.25$, $T = 1.00$, $T = 0.50$. In panels (c)–(g), the upper curve (+) is the helicity modulus without rotation, while the lower curve (×) the helicity modulus with rotation-induced vortices with filling fraction $f = 1/36$ as functions of temperature. Panel (c) shows Υ_z for a cubic uniform system with periodic boundary conditions. The upper curve (+) has the properties of a second order transition (helicity modulus vanishes because of vortex-loop proliferation), whereas the lower curve (×) has the finite-size appearance of a first order transition (suggesting that the helicity modulus vanishes because of vortex lattice melting) [7, 8]. The remaining panels (d)-(g) show $\tilde{\Upsilon}_z(0, R/4)$, $\tilde{\Upsilon}_z(R/4, 2R/4)$, $\tilde{\Upsilon}_z(2R/4, 3R/4)$, and $\tilde{\Upsilon}_z(3R/4, R)$, respectively. The vortex plots on the left (obtained at $T = 0.50$) defines the radii R_1 and R_2 as white circles. Taking parameters from Ref. 2, and using $\Omega = (h/M)N_v/2\pi R^2$ [2] where N_v is the number of vortices in the trap, we find $\Omega \sim 100$Hz. Since $\omega_\perp \sim 500$Hz [2], this puts us well outside the LLL regime.

the absence of circular distortion for the vortices at the edge of the system. On the other hand, by comparing panels (c) and (d), we see that Υ_z and $\tilde{\Upsilon}_z$ are quite similar. This points toward a possibility of the existence of a tensionful VL phase close to the center of the trap.

We have considered vortex matter in the model Eq. 1 with uniform and nonuniform density. The uniform case features dominant angular vortex fluctuations near the wall of the cylinder. Vortex matter in a trapped BEC is more complicated, due to density gradients. We have identified a number of inhomogenous vortex states. Notabley, we find a direct crossover from a vortex solid to tension-less vortex tangle with no discernible intermediate tensionful vortex liquid at low temperatures as the edge of the trap is approached. This explains very regular edges of VLL at finite temperatures in many experiments. At higher temperatures, a possible tensionful vortex liquid state located between a vortex solid at the center and a tension-less vortex tangle closer to the edge is identified. Our simulations indicate strong bending fluctuations of vortices in this region which may obscure its visibility in experiments. An experimental observation of the discrepancy between visible vortex numbers and rotation frequency (as we predict for disordered vortex states) has in fact been observed, albeit in an anharmonic trap [15].

This work was supported by the Research Council of Norway, Grant Nos. 158518/431, 158547/431 (NANOMAT), 167498/V30 (STORFORSK), the National Science Foundation, Grant No. DMR-0302347, Nordforsk Network on Low-Dimensional Physics. Discussions and correspondence with J. Dalibard, A. K. Nguyen, V. Schweikhard, E. Smørgrav, M. Zwierlein and especially with Erich J. Mueller, are gratefully acknowledged.

[1] K. W. Madison *et. al.*, Phys. Rev. Lett. **84**, 806 (2000); I. Coddington *et. al.*, Phys. Rev. Lett. **91**, 100402 (2003); V. Schweikhard *et. al.*, *ibid* **92**, 040404 (2004); N. L. Smith *et al.*, *ibid*, **93**, 080406 (2004); I. Coddington *et al.*, Phys. Rev. A**73**, 063607 (2004); S. R. Muniz *et al.*, Phys. Rev. A**73**, 041605 (2006).

[2] J. R. Abo-Shaeer, C. Raman, J. M. Vogels, and W. Ketterle, Science **292**, 476 (2001).

[3] E. Babaev, A. Sudbø, and N. W. Ashcroft, Nature, **431**, 666 (2004).

[4] S. A. Gifford and G. Baym, Phys. Rev. A **70**, 033602 (2004).

[5] M. Snoek and H. T. C. Stoof, cond-mat/0601695.

[6] R. E. Hetzel, A. Sudbø, and D. A. Huse, Phys. Rev. Lett. **69**, 518 (1992).

[7] X. Hu, S. Miyashita, and M. Tachiki, Phys. Rev. Lett. **79**, 3498 (1997).

[8] A. K. Nguyen and A. Sudbø, Phys. Rev. B **60**, 15307 (1999).

[9] At least 10^5 MC sweeps were discarded for equilibration at each temperature and up to $5 \cdot 10^5$ sweeps were used for calculating averages.
[10] G. Watanabe, G. Baym, and C. J. Pethick, Phys. Rev. Lett. **93**, 190401 (2004); N. R. Cooper, S. Komineas, and N. Read, Phys. Rev. A **70**, 033604 (2004).
[11] L. J. Campbell and R. M. Ziff, Phys. Rev. B **20**, 1886 (1979).
[12] Yu. Lozovik and E. Rakoch, Phys. Rev. B **57**, 1214 (1998).
[13] Z. Tesanovic, Phys. Rev. **B 59**, 6449 (1999).
[14] J. R. Abo-Shaeer, C. Raman, and W. Ketterle, Phys. Rev. Lett. **88**, 070409 (2002).
[15] V. Bretin, S. Stock, Y. Seurin, and J. Dalibard, Phys. Rev. Lett. **92**, 050403 (2004).